

University of New Hampshire

University of New Hampshire Scholars' Repository

Doctoral Dissertations

Student Scholarship

Spring 2009

Determination of geotechnical properties of seafloor sediment using a free fall penetrometer

Gopala Krishna Mulukutla
University of New Hampshire, Durham

Follow this and additional works at: <https://scholars.unh.edu/dissertation>

Recommended Citation

Mulukutla, Gopala Krishna, "Determination of geotechnical properties of seafloor sediment using a free fall penetrometer" (2009). *Doctoral Dissertations*. 480.
<https://scholars.unh.edu/dissertation/480>

This Dissertation is brought to you for free and open access by the Student Scholarship at University of New Hampshire Scholars' Repository. It has been accepted for inclusion in Doctoral Dissertations by an authorized administrator of University of New Hampshire Scholars' Repository. For more information, please contact Scholarly.Communication@unh.edu.

**DETERMINATION OF GEOTECHNICAL
PROPERTIES OF SEAFLOOR SEDIMENT
USING A FREE FALL PENETROMETER**

BY

Gopala Krishna Mulukutla

Bachelor of Engineering (B.E), Andhra University, India, 1997
M.S., Indian Institute of Technology, Madras, India, 2000

DISSERTATION

Submitted to the University of New Hampshire
in Partial Fulfillment of
the Requirements for the Degree of

Doctor of Philosophy

in

Engineering: Ocean

May, 2009

UMI Number: 3363724

INFORMATION TO USERS

The quality of this reproduction is dependent upon the quality of the copy submitted. Broken or indistinct print, colored or poor quality illustrations and photographs, print bleed-through, substandard margins, and improper alignment can adversely affect reproduction.

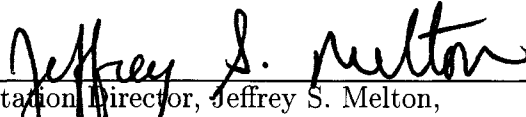
In the unlikely event that the author did not send a complete manuscript and there are missing pages, these will be noted. Also, if unauthorized copyright material had to be removed, a note will indicate the deletion.

UMI[®]

UMI Microform 3363724
Copyright 2009 by ProQuest LLC
All rights reserved. This microform edition is protected against
unauthorized copying under Title 17, United States Code.

ProQuest LLC
789 East Eisenhower Parkway
P.O. Box 1346
Ann Arbor, MI 48106-1346

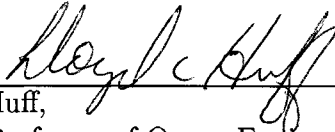
This dissertation has been examined and approved.



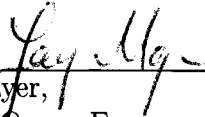
Dissertation Director, Jeffrey S. Melton,
Research Assistant Professor of Civil/Environmental Engineering.



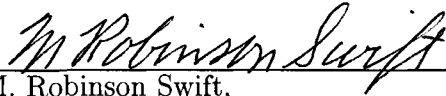
Dissertation Co-director, Kenneth C. Baldwin,
Professor of Mechanical Engineering and Ocean Engineering.



Lloyd C. Huff,
Research Professor of Ocean Engineering.



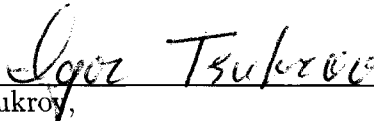
Larry A. Mayer,
Professor of Ocean Engineering and Earth Sciences.



M. Robinson Swift,
Professor of Mechanical Engineering and Ocean Engineering.



Pedro A. De Alba,
Professor of Civil Engineering and Ocean Engineering.



Igor I. Tsukroy,
Associate Professor of Mechanical Engineering and Materials Science.

Date

4/7/09

DEDICATION

This work is dedicated to my family and especially to Emese.

नासदासीन्नो सदासीत्तदानीं नासीद्रजो नो व्योमा परो यत्
किमावरीवः कुह कस्य शर्मन्नम्भः किमासीद्गहनं गभीरम्

There was neither non-existence nor existence then.
There was neither the realm of space nor the sky which is beyond.
What stirred? Where? In whose protection?
Was there water, unfathomably deep?

-*Nasadiya Sukta, Rig Veda, Mandala 10, Hymn 129*
- Translation from Doniger-O'Flaherty (1981)

ACKNOWLEDGMENTS

This work would not have been possible without advice, support and assistance provided by several individuals. First and foremost I would like to thank my advisors, Prof. Baldwin and Prof. Melton for giving me an opportunity to work on this research. I also thank them for committing time and support for this work.

I also thank members of my doctoral committee especially Prof. Huff, for his letting me work in the EFH project and for providing invaluable insight into the working of free fall probes. Prof. Mayer, Prof. De Alba, Prof. Swift and Prof. Tsukrov for their encouragement.

It would have been impossible to complete this work without the support provided by Stan Boduch, Dr. Jim Irish, Glenn McGillicuddy, Brett Fullerton, Glen Rice and Mashkooor Malik in lab testing, troubleshooting and field deployment of the probe. The crew of R/V Gulf Challenger and R/V Coastal Surveyor for assistance during the deployment of the probe. Prof. Germaine at MIT for letting me use his vane shear equipment. Thanks also to Rich Rouleau at UNH Facilities for providing geotechnical site investigation data. Thanks as well to colleagues and friends, especially Jud, at Ocean Engineering for fostering a wonderful working environment that made my stay thoroughly enjoyable.

Last but not the least, I am thankful to my family and Emese for patience and understanding. This work would not have been possible without them.

TABLE OF CONTENTS

DEDICATION	iii
ACKNOWLEDGMENTS	iv
LIST OF TABLES	viii
LIST OF FIGURES	ix
ABSTRACT	xiii
1 INTRODUCTION	1
1.1 General	1
1.2 Problem Statement	1
1.3 Objectives	3
1.4 Organization of Dissertation	3
2 BACKGROUND IN RELEVANT AREAS	5
2.1 Introduction	5
2.2 Quasi-static Penetration	6
2.3 Instrumented Impact Probes	10
2.3.1 History	10
2.3.2 Various Probes	11
2.4 Sediment Characterization	18
2.4.1 Sediment Strength	21
2.4.2 <i>In Situ</i> Pore Pressure Measurements	23

2.5	Literature Review	25
2.6	Conclusions from Literature Review	32
3	FORMULATION OF ANALYTICAL MODEL	34
3.1	Introduction	34
3.2	Sediment Classification	34
3.3	Forces Acting on a Freely Falling Probe	36
3.4	Characteristics of Acceleration Signals	38
3.5	Embedment Types	40
3.6	Firmness Scale	42
3.6.1	Effect of Mass, Tip Geometry and Impact Velocity	45
3.7	Evaluation of Undrained Shear Strength	49
3.7.1	Influence of Strain Rate	49
3.7.2	Evaluation of Bearing Capacity Factors	51
3.8	Pore Pressure Dissipation Study	54
3.8.1	Formulation of Cylindrical Cavity Expansion Model	55
3.8.2	Solution for Normal-Stress Induced Pore Pressure	59
3.8.3	Solution for Shear-Stress Induced Pore Pressure	62
3.8.4	Model Validation and Analysis of Results	64
4	FIELD DEPLOYMENT PROGRAM	70
4.1	Objectives and Approach	70
4.2	The Free Fall Cone Penetrometer (FFCPT)	70
4.3	Pre-deployment Assembly and Testing	71
4.4	Field Deployment - Piscataqua River	78

4.5	Bering Sea	78
4.6	Shear Strength Determination Using a Field Vane Shear	86
4.7	The Field Vane Shear Borer Equipment	86
4.8	Interpretation of the Data	87
4.9	FVS Deployment	88
5	DATA ANALYSIS AND RESULTS	89
5.1	Introduction	89
5.2	Data Processing	89
5.2.1	Initial Data Processing	89
5.2.2	Analysis Tool	94
5.3	Results	94
5.3.1	Sediment Classification Model	94
5.3.2	Validation of Sediment Classification Model	98
5.3.3	Bering Sea Sediment Map	101
5.3.4	Undrained Shear Strength	105
5.3.5	Study of Pore Pressure	107
6	CONCLUSIONS AND RECOMMENDATIONS	116
6.1	Conclusions	116
6.2	Recommendations for Further Research	118
	APPENDIX	120
	REFERENCES	130

LIST OF TABLES

2.1	Summary of impact tests.	28
2.2	Variables influencing penetrometer-sediment interaction process. . .	33
3.1	Sediment classification based on mean grain size.	35
3.2	Summary of impact test data used in developing the firmness scale.	44
3.3	Summary of dissipation model input parameters.	65
4.1	Configuration of UNH and AFSC probes.	71
4.2	Summary of field deployment.	78
4.3	Summary of field deployment in the Bering Sea.	84

LIST OF FIGURES

2-1	Diagram of a WISON cone penetrometer.	7
2-2	Diagram of SEACLAM, a seabed platform system.	8
2-3	Soil classification chart based on CPT data.	9
2-4	Schematic diagram of a marine impact penetrometer.	12
2-5	Schematic of Expendable Doppler Penetrometer.	14
2-6	Application of CPT soil classification chart to free fall penetrometer data.	16
2-7	Schematic diagram and pictures showing deep water and shallow water free fall cone penetrometer developed at the University of Bremen	17
2-8	Schematic diagram of an eXpendable Bathymetric Probe (XBP). . .	18
2-9	Sediment type classes grouped based on peak accelerations from XBP drops.	19
2-10	Study of bottom type based on the characteristic shape of the accel- eration signal.	20
2-11	Plot of $(a_{max}/(gv_i))$ Vs. t_t for a hemispherical probe.	20
2-12	Failure mechanism for wedge penetration into soil for small and large relative depths	24
2-13	A schematic diagram of Pop-Up Pore Pressure Instrument (PUPPI). . .	26
2-14	Schematic diagram of Davis-Villinger Temperature-Pressure Piezo- probe (DVTP-P).	27
3-1	Figure showing the forces acting on a free falling penetrometer. . .	37
3-2	Figure showing events in a typical drop of a free fall penetrometer to the seafloor.	39

3-3	Diagram showing three embedment types and their corresponding acceleration-time signal shapes.	41
3-4	A logarithmic plot of normalized peak acceleration (a_{max}/g) divided by impact velocity(v_i) plotted against total duration of the acceleration-time signal (t_t).	43
3-5	Effect of varying probe mass on firmness factor (F_f).	46
3-6	Effect of varying probe shape on the firmness factor.	47
3-7	Effect of high impact velocity of hemispherical probe on soils.	48
3-8	Outline of a conical probe and variation of shear strength with depth.	52
3-9	Pressure sensor output from the drop of a free fall probe with principal events identified.	56
3-10	Illustration of pore pressure in shallow seabed.	57
3-11	Diagram showing details of zones of deformation in sediment surrounding an embedded free fall probe.	60
3-12	Measured and modeled pore pressure dissipation at depth of 18.5 m in a soft clay site in Onsøy, Norway	66
3-13	Measured and modeled pore pressure dissipation in a stiff clay at a depth of 17.2 m in a site in Cowden, UK.	67
3-14	Measured and modeled pore pressure dissipation in a highly over-consolidated stiff clay at a depth of 11.2 m.	68
3-15	Plot showing the contribution of individual components of total pressure at a soft clay site in Onsøy, Norway.	68
3-16	Plot showing the contribution of individual components of total pressure at a stiff clay site in Cowden, UK.	69
3-17	Plot showing the contribution of individual components of total pressure at a stiff clay site in Madingley, UK.	69

4-1	Photograph showing the various modules in the Free Fall Cone Penetrometer (FFCPT)	72
4-2	Photograph showing a unit similar to the AFSC FFCPT with various modules identified.	73
4-3	A fully assembled FFCPT probe being tested at the Center for Ocean Engineering.	74
4-4	The FFCPT being tested for performance underwater.	75
4-5	The raw data output from a vertically positioned FFCPT using company supplied software.	76
4-6	The raw data output from a FFCPT dropped into a drum of sand.	77
4-7	Satellite image showing the Great Bay estuary and the FFCPT deployment stations	79
4-8	Satellite image showing the location of the Station NP	79
4-9	Satellite image showing the location of the Staion FP	80
4-10	FFCPT deployment from R/V Gulf Challenger in the Piscataqua River (station GB).	80
4-11	FFCPT deployment in the Piscataqua River.	81
4-12	Map showing the location of survey area in the Bering Sea.	83
4-13	The FFCPT and SEABOSS grab sampler being deployed off the Vessel NOAA <i>Fairweather</i> in the Bering Sea.	84
4-14	Figure showing various components of Field Vane Shearer Borer	87
4-15	Photograph of Geonor H-10 FVS Borer.	88
5-1	Flowchart describing the tool for preprocessing program PREP.	91
5-2	Plot of raw data from the OBS sensor, accelerometers and tail and tip pressure sensors.	92
5-3	Plot showing output from program PREP.	93

5-4	An organization chart of processing tool.	95
5-5	Plot extending the firmness scale to include data from this study. . .	97
5-6	Plot of impact velocity against water depth for Bering Sea deployment.	98
5-7	Plot showing the grain size distribution curves from samples collected at 26 stations in the Bering Sea.	99
5-8	Plot showing the proposed sediment classification model.	100
5-9	Bottom type prediction at Station NP	102
5-10	Grain size distribution curves of sediments at station NP	103
5-11	Sediment Map of surveyed area in the Bering Sea based on FFCPT data.	104
5-12	Variation of model cone factors with normalized embedment depth.	106
5-13	Sediment type at Station FP determined using the sediment classi- fication model.	108
5-14	Variation of undrained shear strength with depth, as station FP. . .	109
5-15	Comparison of FFCPT shear strength profiles with data from field vane shear studies.	110
5-16	Comparison of FFCPT shear strength profiles with no influence of strain rate data.	111
5-17	Shear strength profiles from Station A04 in the Bering Sea.	112
5-18	Variation of positive and negative pore pressure with mean grain size for Bering Sea sediments.	114
5-19	Variation of firmness factor (F_f), normalized embedment depth (z/D) and excess positive and negative pore pressure to mean grain size (M_z).	115

ABSTRACT

DETERMINATION OF GEOTECHNICAL PROPERTIES

OF SEAFLOOR SEDIMENT USING A FREE FALL

PENETROMETER

by

Gopala Krishna Mulukutla

University of New Hampshire, May, 2009

A study was conducted to determine the penetration behavior of a cylindrical probe free falling to the seafloor and to utilize the data obtained to evaluate the engineering properties of surficial sediment. Two experimental probes, each equipped with accelerometers, pressure sensors and optical backscatter sensors were deployed in different sediment regimes. The data collected was used to derive the sediment type and determine physical properties such as undrained shear strength, coefficient of consolidation and shear modulus for soft fine-grained sediment.

Acceleration signals from drops of a free fall penetrometer contain information about the nature of the seafloor. A simple sediment classification model was proposed using data from field deployment tests as well as literature. This model, though applicable only to the probes used in this study, presents an approach that can expand the usage of free fall penetrometers.

Rapid penetration with rigid probes in saturated sediments usually results in an increase in measured penetration resistance. This effect, called the strain rate effect,

was studied for soft fine-grained sediments by formulating a model to determine undrained shear strength profiles.

Excess pore pressure dissipation seen in post-arrest pressure sensor signals in fine-grained sediments were studied to predict the coefficient of consolidation and by extension permeability and shear modulus. A dissipation model using a cylindrical cavity expansion method was formulated for this purpose.

A field study was conducted to validate the sediment classification model and undrained shear strength models. Field vane shear tests at the location of the probe drops were used to validate the strain rate dependent strength model.

This work facilitates the expanded use of free fall penetrometers as part of geotechnical, geophysical and geological studies of the seafloor.

CHAPTER 1

INTRODUCTION

1.1 General

Recent studies describing the use of tethered free fall probes to test the in-place strength and other properties of sediment have fueled renewed research in this area (see for example Stoll and Akal (1999); Aubeny and Shi (2006) and Stoll (2006)). Advances in probe technology and the need for robust methods and models to assess the physical properties of sediments has resulted in research focused on the ability of such probes to deliver important sediment geotechnical properties. This study was supported in part by National Oceanic and Atmospheric Administration's (NOAA) Alaska Fisheries Science Center (AFSC) and the Center for Ocean Engineering at the University of New Hampshire (UNH).

1.2 Problem Statement

Many studies of coastal and offshore regions require knowledge of the physical properties of underlying layers of sediments. As part of these studies samples of sediments are collected for testing on-board a vessel or in a laboratory. Such techniques usually require the deployment of instrumentation requiring heavy handling.

Factors such as the expense of deployment, the sea state and disturbances caused during sampling usually limits the use of such methods. *In situ* or "in place" testing of sediments accomplished by deploying a probe has gained popularity mainly due to the ease of use and the ability to measure field values of required parameters. The use of instrumented free fall probes is one such *in situ* test.

A typical free fall probe consists of a slender cylindrical body tipped with either a hemispherical or a conical nose to aid penetration. It is suitably instrumented with sensors such as accelerometers, pressure ports, friction sleeves and optical backscatter sensors, etc. Typically the instrumented tethered, free fall probe is dropped from a vessel to impact the seabed, penetrate and then is retrieved. The rate of deceleration is measured by the accelerometers, which then is used to derive the dynamic penetration resistance. The pressure sensor measures the dynamic pore pressure during the penetration event and the dissipating pressure when the probe is embedded and at rest. Such probes typically penetrate a few meters into the seabed and have the potential to produce quick and economical data that is used to determine strength properties and consolidation properties of the sediment.

Free fall penetrometers (FFP) find application in various studies of the seafloor like offshore construction, deep sea mine burial, installation of undersea pipelines, etc. A review of the applications of such probes shows that in several cases the probe is either dropped in known sediment type to assess sediment strength or other methods are employed to identify sediment type using samples collected and tested on-board or in the laboratory. A method that can determine the sediment type and physical properties using a rapid drop and retrieve method would extend

the use of free fall probes to newer areas where rapid testing is useful in sediment mapping studies for various properties over large survey areas. This study is aimed at extending the application of free fall probes to studies that require quick identification and characterization of surficial sediment.

1.3 Objectives

This dissertation describes formulation of an analytical model, field studies and analysis of data obtained from free fall cone penetrometers. The analytical model principally deals with identifying the sediment, determining undrained shear strength using a strain-rate dependent model and coefficient of consolidation of fine-grained sediments determined using a pore pressure dissipation model.

The objectives of this research were established as the following:

1. Develop a system to distinguish sediment type by analyzing acceleration signals.
2. Develop an analytical framework to determine properties of fine-grained sediments, such as undrained shear strength, coefficient of consolidation and by extension rigidity index and permeability.
3. Provide validation of the analytical framework using field studies.

1.4 Organization of Dissertation

This research mainly consists of analytical studies and experimental field work. Chapter 2 describes the background of the research problem including an extensive

review of relevant literature.

In Chapter 3 an analytical model is formulated that details the free fall penetrometer as a stand-alone unit capable of measuring sediment resistance and pore pressure. A model to identify the predominant character of the surficial sediment is formulated based on the study of acceleration signals. A method is introduced to determine undrained shear strength of soft fine-grained sediments using dynamic penetration resistance. A model is also formulated to determine the consolidation properties of fine-grained sediments using post-arrest pore pressure dissipation.

Chapter 4 describes the field testing program undertaken to gather data for testing the analytical model. Two free fall cone penetrometers were deployed in waters off Portsmouth and New Castle, New Hampshire as well as in the Bering Sea, Alaska. This chapter also describes deployment of Field Vane Shear (FVS) equipment at a site where a Free Fall Cone Penetrometer (FFCPT) was deployed. This study was used to validate the developed shear strength determination procedure.

In Chapter 5 a sediment classification model based on the analysis of the data obtained in field deployment is formulated. The analytical model to determine undrained shear strength profiles is validated by comparing results obtained from the analytical to data from vane shear studies. The sediment classification system is validated using data from free fall probe drops and comparing with data from prior field investigations.

Chapter 6 summarizes the study and provides principal conclusions, important design recommendations and suggestions for future studies.

CHAPTER 2

BACKGROUND IN RELEVANT AREAS

2.1 Introduction

Penetration of a rigid body into deformable media is of interest to researchers in many fields of engineering and science. In engineering studies probes suitably instrumented are used to infer information about the physical and strength properties of soils. This principle has been applied in two ways. The first is when probe penetration into the target material is at a slow and constant rate also called "quasi-static penetration". Cone Penetrometer Testing (CPT) is a commonly used term for such quasi-static that uses cone tipped penetrometers. The second is when a probe is allowed to impact the target material at a velocity dictated by deployment conditions that are usually free fall or forced impact. This is termed "dynamic or impact penetration".

Instrumented probes used in the terrestrial and marine environment have been described as penetrometers or penetrators. Other terms include piezometers for probes instrumented to measure pore pressure. McNeill (1979) defined a penetrator as "a device which penetrates smoothly after impacting the soil surface with an initial velocity, continuously measures one or more of the properties and transmits them to be recorded on board".

2.2 Quasi-static Penetration

In situ quasi-static penetration tests in offshore areas are normally conducted using cone penetrometers by deploying a wireline system or a seabed platform (McNeill and Noorany, 1983). In the wireline technique, cone penetrometers instead of samplers are inserted into a drill pipe using a drill string as a casing while measurements are done in the advancing borehole. In the seabed platform technique cone penetrometer testing is done with a probe of standardized dimensions, instrumented to measure penetration resistance and pore pressure, being pushed into the seabed or ground at a constant rate of approximately 2 cm/s. Figure 2-1 shows the diagram of a marine penetrometer named WISON designed by B.V. Fugro, Netherlands (from McNeill and Noorany, 1983). Figure 2-2 shows a seabed platform system developed by B.V. Fugro to deploy a WISON penetrometer (from McNeill and Noorany, 1983).

CPT testing is one of the most widely used *in situ* terrestrial testing techniques for soils. Penetration resistance and pore pressure response from CPT tests have been used to develop empirical correlations to determine soils strength, soil classification, stress history, consolidation coefficient, hydrostatic pore pressure (Yu, 2004). For example, Figure 2-3 shows an empirical chart proposed by Robertson, 1990 that is used to interpret sediment type from variables derived from penetration resistance in the tip and friction sleeve during testing. However, CPT usage in the offshore areas is limited by factors such a water depth and cost. Free fall probes, whose penetrating mechanics differ significantly from CPTs, can be quickly dropped and retrieved have the potential to provide a cost-effective alternative to

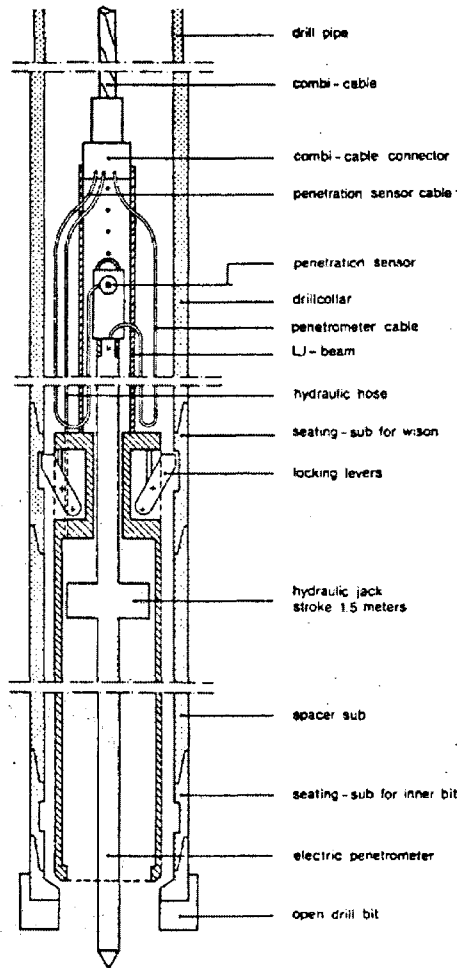


Figure 2-1: Diagram of a WISON cone penetrometer used for quasi-static testing using a wireline or seabed platform (from McNeill and Noorany, 1983).

CPT usage. This is conditional on the development of empirical sediment identification models that consider the distinct penetration mechanics of such probes.

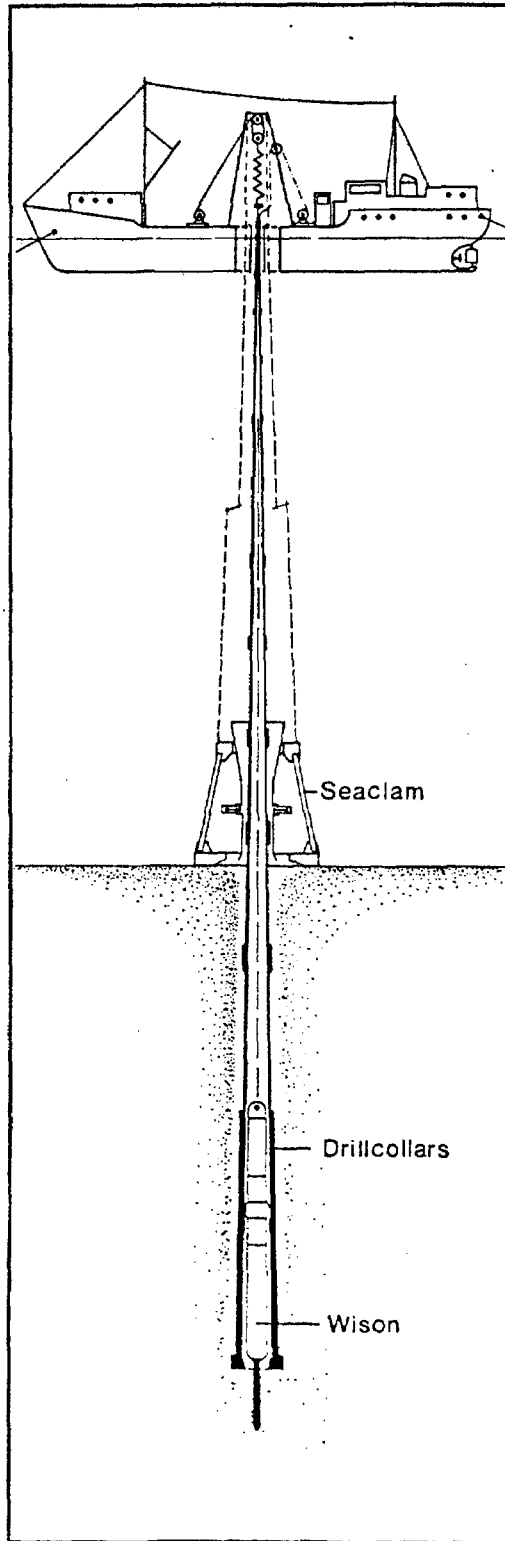


Figure 2-2: Diagram of a SEACLAM a seabed platform system used to deploy a WISON penetrometer (from McNeill and Noorany, 1983).

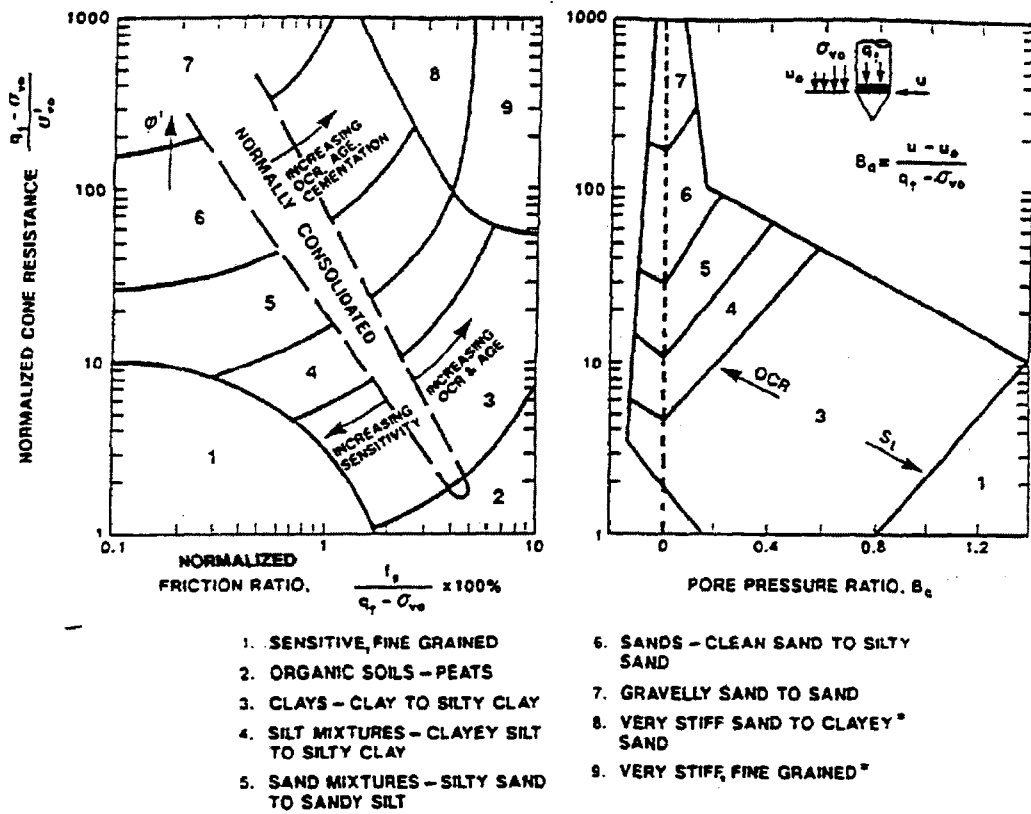


Figure 2-3: A soil classification chart based on quasi-static CPT data. The parameters used are penetration resistance measured by tip and friction sleeve, and pore pressure (from Robertson, 1990).

2.3 Instrumented Impact Probes

2.3.1 History

Impact probes were first studied to predict the depth of penetration of projectiles impacting man-made structures and designed based on the classical problem of terminal ballistics (Dayal, 1981). Such studies were undertaken to expand understanding of the impact of bombing and shelling of military installations. Scientists and engineers expanded the application of these principle to *in situ* measurements using impact probes to study soils or "soil-like" material in terrestrial, oceanic and lunar/planetary bodies that are not easily accessible by other means.

The earliest known design of an impact probe to study *in situ* properties of soils was by Knight and Blackmon (1957) at the US Army Engineer Waterways Experimental Station (USAE-WES) in Vicksburg, Mississippi (as reported by Thomspson and Mitchell (1971)). Other studies include early efforts by Scott (1970) to instrument a core barrel sampler with an accelerometer to measure the strength of ocean sediments and the work of McCarty and Carden (1962) on the feasibility of using instrumented probes to test the lunar surface. Studies in the last three decades have continued focus on determining new methodologies to test *in situ* properties of inaccessible terrestrial materials, ocean sediments and lunar/planetary surfaces using free fall or impact probes.

Estimating physical properties of ocean sediments using instrumented probes that can be rapidly dropped and retrieved from a vessel provide a cost-effective option in comparison with retrieving sediment samples for testing. Free fall probes

have been used in the marine environment for various studies including sediment characterization, seafloor slope stability, environmental studies, hazard mapping, stratification logging, mine burial, design of foundations for anchoring of floating productions and storage systems, geo-acoustic surveys pipeline and cable projects, harbor dredging, fresh water research in paleolimnology, and physical limnology, etc. (Stoll, 2006, Dayal, 1981, Spooner et al., 2004 and Meunier et al., 2000).

2.3.2 Various Probes

The first reported instrumented impact penetrometer for the marine environment was by Dayal and Allen (1973) (see Figure 2-4). It was instrumented with accelerometers and tipped with a conical nose with a 60° apex angle and a friction sleeve to measure the adhesive resistance at the surface of the probe. It was also one of the early works where the dynamic *in situ* strength of sediment measured by an impact penetrometer was recognized and studied in relation to static strength. Work by Dayal and Allen (1973) also recognized the "strain rate" effect, the apparent increase in strength due to rapid loading and gave an equation to relate dynamic strength to static strength.

$$\frac{S_d - S_s}{S_s} = 0.10 \log_{10} \frac{V_d}{V_s} \quad (2.1)$$

where S_d is the dynamic shear strength at velocity V_d and S_s is the static shear strength at a reference or 'static' velocity V_s . A velocity of 1.5 – 2 cm/s was used as the 'static' velocity for calculating the dynamic *in situ* strength of sediment.

Expendable Doppler Penetrometer (XDP) was another early marine free fall

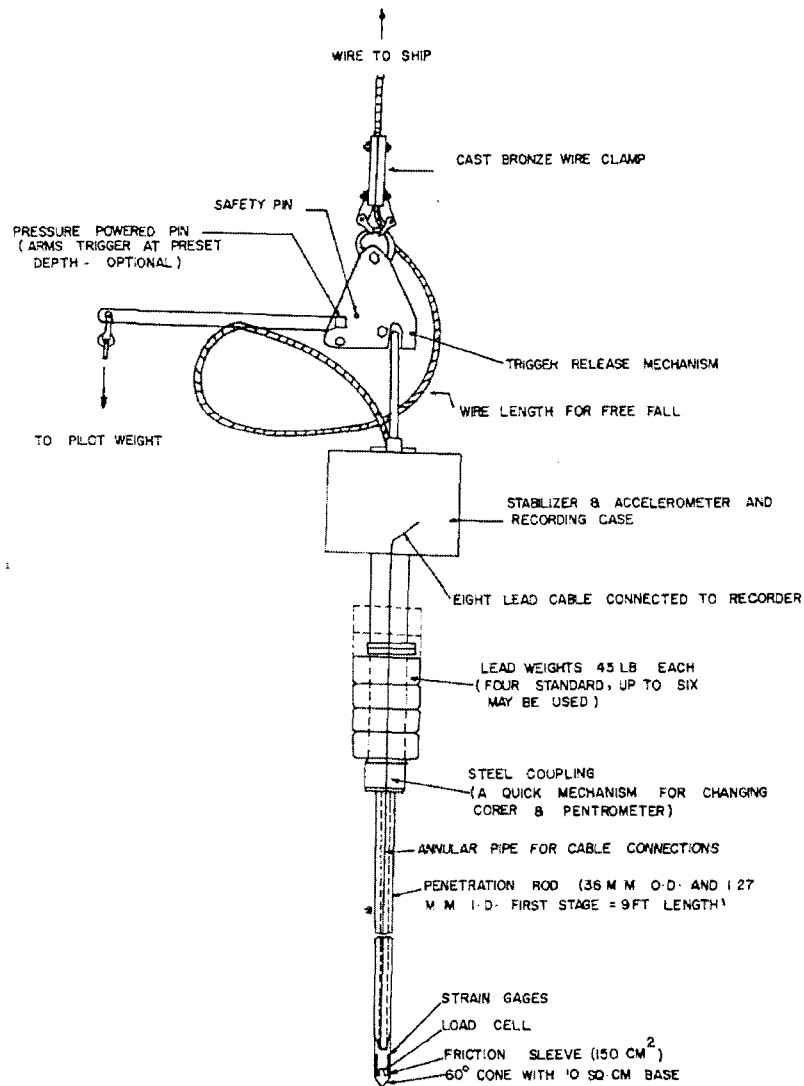


Figure 2-4: Schematic diagram of a marine impact penetrometer (from Dayal and Allen, 1973).

probe designed to measure *in situ* sediment strength (see Figure 2-5). Beard (1981) reported the performance of an XDP as early as 1977. The Doppler effect was used in instrumenting the probe with an acoustic source and deploying a receiver off a support vessel to record the apparent shift in emitted acoustic signal. The shift is proportional to the velocity of the probe and thus its position and dynamic penetration resistance. Beard used a formulation developed by True (1976) to relate the dynamic penetration resistance to the *in situ* strength of sediment.

$$M'v(dv/dz) = F_D + W_b - F_{BE} - F_{AD} - F_H \quad (2.2)$$

where M' is the effective mass of the probe, v is the probe velocity, z is the soil depth, F_D the external driving force, W_b buoyant unit weight of the probe, F_{BE} the bearing force component, F_{AD} the side adhesion force and F_H the inertial drag force. The bearing force is related to the undrained shear strength of sediment by the following equation.

$$F_{BE} = S_{\dot{\epsilon}}(S_u N_c A_f) \quad (2.3)$$

where $S_{\dot{\epsilon}}$ is a soil strength strain rate factor, S_u is the soil undrained shear strength, N_c is the bearing capacity factor, and A_f penetrator frontal area. True (1976) provided a formulation to relate the strain rate to the probe velocity and the shear strength of the sediment by the following equation.

$$S_{\dot{\epsilon}} = \frac{S_{\dot{\epsilon}}^*}{1 + \frac{1}{\sqrt{(C_{\dot{\epsilon}}v/S_{ut})+0.6}}} \quad (2.4)$$

where $S_{\dot{\epsilon}}^*$ is an empirical strain rate factor, $C_{\dot{\epsilon}}$ is an empirical strain rate coefficient

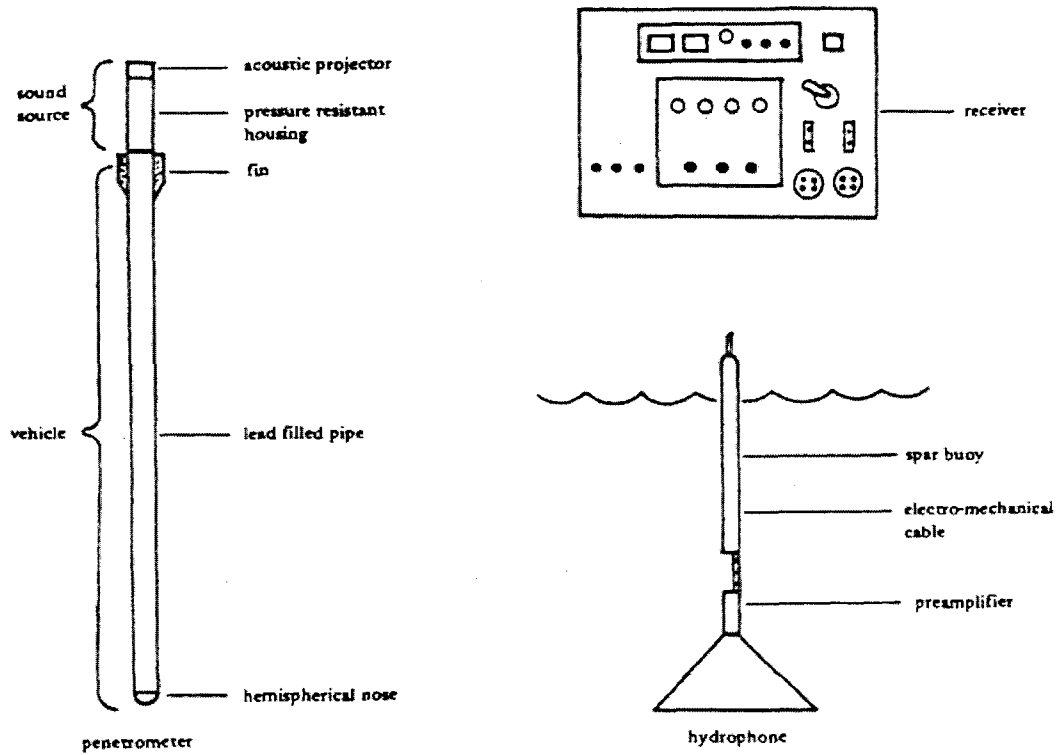


Figure 2-5: Schematic of Expendable Doppler Penetrometer (from Beard, 1985). The penetrometer (left) contains a sound source that relays an acoustic signal to a hydrophone receiver (right) monitored from a support vessel. The velocity of the probe is determined by studying the shift in the emitted acoustic signal. The velocity data is then used to determine the *in situ* strength of sediment.

and t is the probe diameter.

The bearing capacity theory, commonly applied to the study of foundations and used extensively in the study of quasi-static CPT forms the basis of a majority of the models developed to determine *in situ* strength. The most common form of the bearing capacity equation used directly from the CPT testing approach is given by the following equation (Lunne et al., 1997):

$$S_u = (q_t - \sigma_{vo})/N_k \quad (2.5)$$

where q_t is the penetration resistance, σ_{vo} is the *in situ* total vertical stress and N_k is an empirical cone factor that varies between 15 and 20 for soft sediment. In CPT the penetration resistance is commonly studied in relation with pore pressure response for the purpose of classifying the soil. A pore pressure parameter given by the following equation is normally used for this purpose.

$$B_q = \frac{(U_d - U_o)}{(q_t - \sigma_{vo})} \quad (2.6)$$

where U_d is the dynamic pore pressure measured during penetration and U_o is the hydrostatic pressure at the depth under consideration giving the excess pore pressure $(U_d - U_o)$. q_t and σ_{vo} are the penetration resistance and total vertical stress respectively. Extensive testing in soils using a CPT at a constant penetration rate of 2 cm/s has resulted in a sediment classification charts relating factors such as penetration resistance and pore pressure ratio. A popular chart that has been adapted in applications using free fall probes is developed by Robertson (1990). Figure 2-6 shows the classification chart applied to data from FFCPT (from Melton, 2005). The FFCPT, a free fall cone penetrometer designed by ODIM Brooke Ocean Technologies Inc (BOT) which is described in a later chapter.

The approach of directly applying CPT data analysis techniques to free fall probe data has been taken by researchers. It includes work done using two free fall cone penetrometers (ffCPT) developed at the University of Bremen, Germany (Stegmann et al., 2005). As seen in Figure 2-7 they are instrumented with accelerometers and pore pressure sensors for short and long term pore pressure measurement and designed separately for use in shallow and deep water applications.

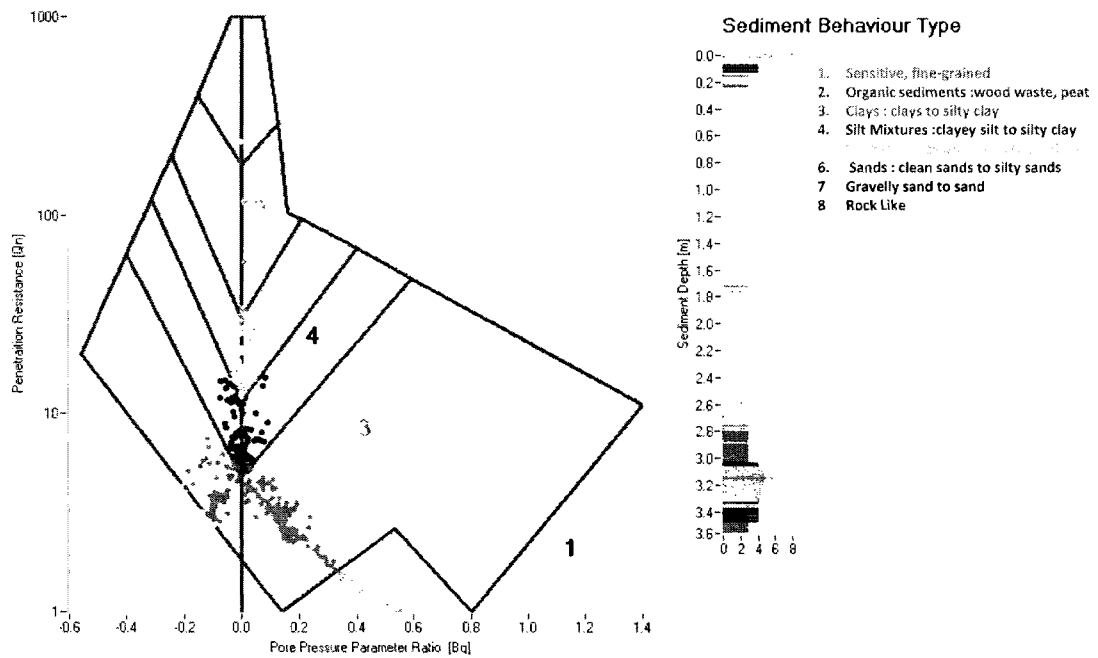


Figure 2-6: Sediment classification based on penetration resistance and pore pressure ratio. Originally developed for a CPT data by Robertson (1990), this method or its modification has been used to classify sediment using free fall probe data. This plot is a direct adaptation of Robertson's work for fFCPT data (from Melton, 2005). In a similar approach Stegmann et al. (2006) reported the use of a modified chart to classify sediment from fFCPT data

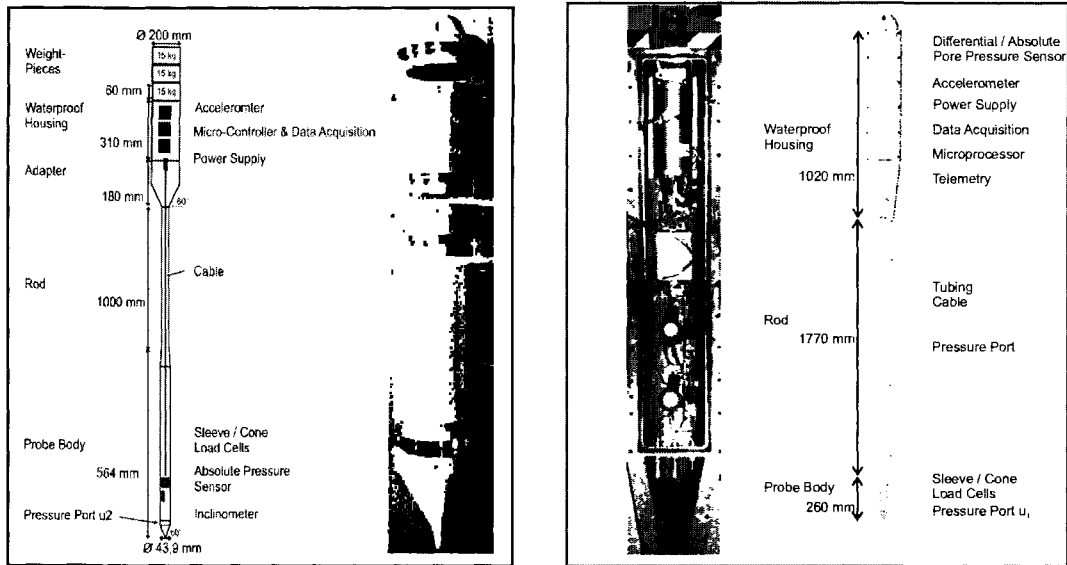


Figure 2-7: Schematic and pictures showing deep water (left) and shallow water (right) free fall cone penetrometer developed at Center for Marine Environmental Sciences, University of Bremen, Germany (from Stegmann et al., 2006). The probe is equipped with accelerometers as well as differential pore pressure ports.

The *in situ* shear strength determined using this approach has been used to study slope stability problems (Stegmann et al., 2007 and Strasser et al., 2007).

The Expendable Bathymetric Probe (XBP) is a small inexpensive, easily deployable, probe instrumented with accelerometers that can be used in a rapid survey of the seafloor (see Figure 2-9). A strain-rate dependent strength model to determine the undrained shear strength of soft sediment was validated using data from XBP deployment by Aubeny and Shi (2006). Their model developed is discussed in the context of a strain-rate dependent model formulated in a later section of this dissertation.

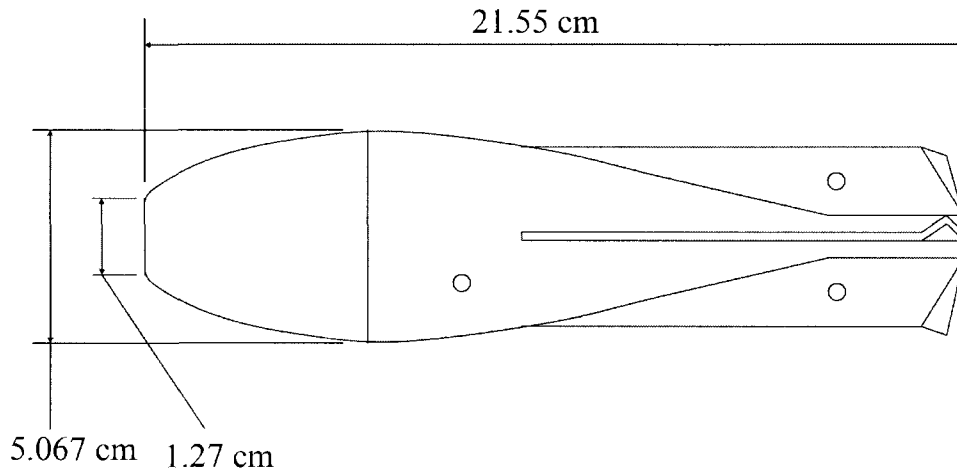


Figure 2-8: Schematic diagram of an eXpendable Bathymetric Probe (XBP) designed and developed by Stoll and Tumay (1997). The probe is equipped with an accelerometer (from Aubeny and Shi, 2006).

2.4 Sediment Characterization

Identification of sediment type is normally done using bottom sampling equipment. The cost of acquiring geotechnical properties using bottom sampling rises with increasing water depth and deteriorating sea state (Beard, 1981); thus limiting many bottom sampling studies to fair weather. Acceleration-time signals obtained from the impact of projectiles in geological materials can be used to evaluate the properties of the targeted material. This approach can provide a distinct advantage in comparison with bottom sampling devices. One of the first to apply this principle was McCarty (McCarty and Carden, 1962 and McCarty and Carden, 1968) who studied impact characteristics of dry target media such as sand and silt. More recently Stoll et al. (2007) chose peak acceleration (a_{max}) as a variable to categorize seabed types (Figure 2-9). Spooner et al. (2004) applied a technique used in characterizing Gaussian curves to determine a "hardness coefficient" (C). C is given

by:

$$C = \frac{a_{max}/2}{gt_{1/2}} \quad (2.7)$$

where a_{max} is the peak acceleration, $t_{1/2}$ is the width of the acceleration-time curve at $1/2(a_{max})$ and g is the acceleration due to gravity. Figure 2-10 shows a 50 kHz sonar record of a lake bed along with different characteristic shapes of acceleration curves of drops and hardness coefficients obtained from an experimental free fall penetrometer (from Spooner et al., 2004).

McCarty and Carden (1962) proposed a "firmness" scale specific to a probe. Figure 2-11 shows $a_{max}/(gv_i)$ vs. t_t plot for a hemispherical probe ($D = 0.0508m$) for materials with "firmness" ranging from concrete to lead. Where t_t is the total duration of impact. Such a scale, for specific probes, could be used to distinguish targeted materials by its position on the scale.

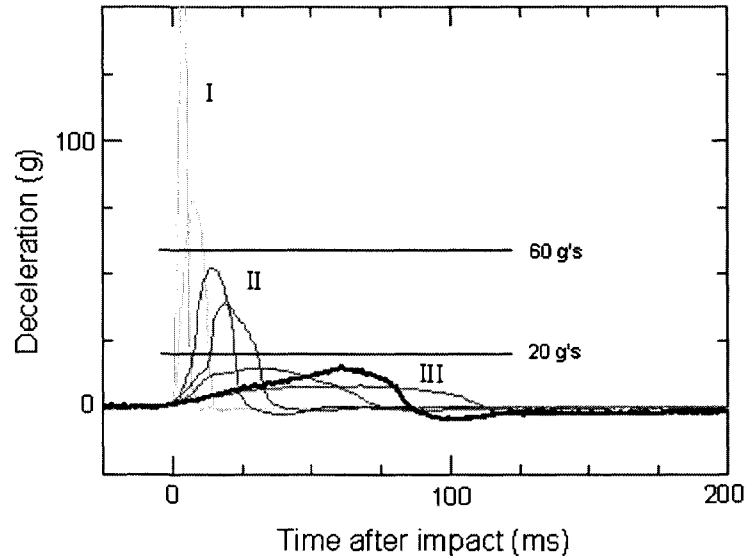


Figure 2-9: Sediment type classes grouped based on peak accelerations from XBP drops (Stoll et al., 2007).

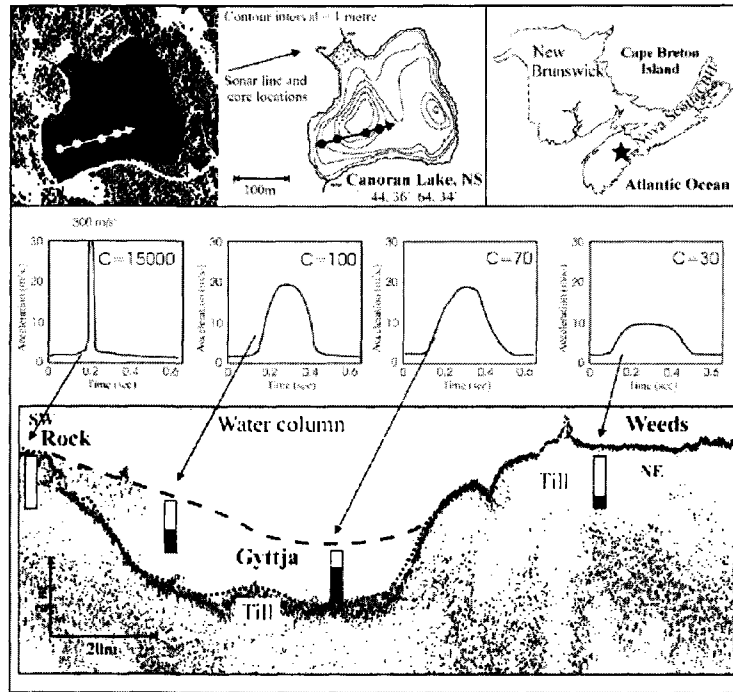


Figure 2-10: Study of bottom type based on the characteristic shape of the acceleration signal (Spooner et al., 2004).

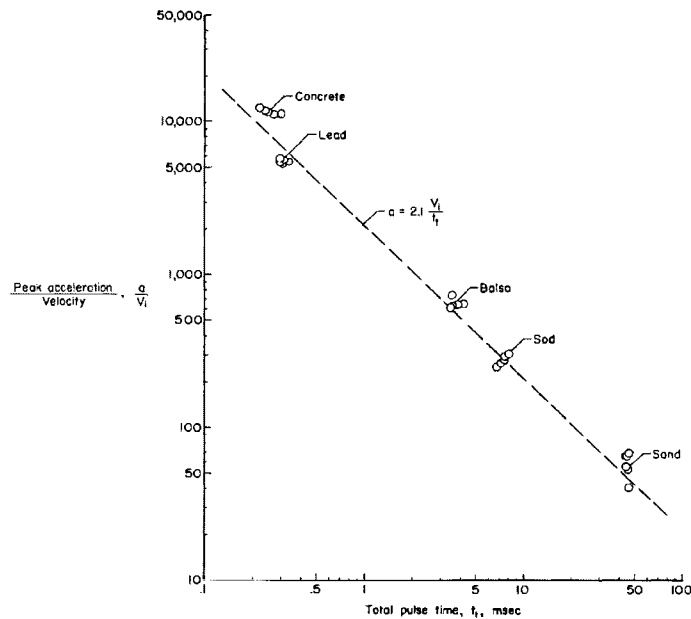


Figure 2-11: Plot of $(a_{max}/(g v_i))$ Vs. t_t for a hemispherical probe ($D= 0.0508m$) for materials with "firmness" ranging from concrete and lead to sand (from McCarty and Carden, 1962).

2.4.1 Sediment Strength

Deformations produced by a rigid penetrometer advancing in saturated sediment results in forces that resist the penetration. This mechanism, provided the dynamic nature of the penetration is discounted, is similar to resistance offered by soils to bearing failure of foundations. This principle has been used as a starting point to formulate analytical models to determine sediment strength derived from dynamic penetration resistance. True (1976) was among the first to use this principle. More recently Lee and Elsworth (2004) and Shi (2005) and Stegmann et al. (2006) have used this principle predictive strength and dissipation models.

Prandtl's formula (given by Durgunoglu and Mitchell, 1973) for the ultimate bearing capacity (q_f) of a strip footing under a rigid-plastic, incompressible, weightless soil that follows Mohr-Coulomb failure criteria is given by:

$$q_f = cN_c \quad (2.8)$$

where N_c is given by

$$N_c = \cot\phi [e^{\pi \tan\phi} \tan^2(\frac{\pi}{4} + \frac{\phi}{2}) - 1] \quad (2.9)$$

The Mohr-Coloumb failure criteria is given by the following equation:

$$S_f = c + \sigma \tan\phi \quad (2.10)$$

Where S_f is the shear strength, c is the cohesion, σ the normal stress and ϕ the

angle of friction.

Terzaghi extended the study with an equation that included soil cohesion, friction and surcharge (Bowles, 1996)

$$q_f = cN_c + qN_q + \frac{1}{2}\gamma_sBN_\gamma \quad (2.11)$$

where q_f is the ultimate bearing capacity of a infinitely long footing of width B. N_c , N_q and N_γ are empirical bearing capacity factors. q is the surcharge, γ_s is unit weight of soil. Numerical methods are used to solve the Equation 2.11 using mechanisms constructed to predict the pattern of failure.

Terzaghi also considered additional factors in refining the bearing capacity equation. Those included, surface roughness of the foundation as well as accounting for shapes other than strip footings.

$$q_f = cN_c\xi_c + 1/2\gamma_sBN_\gamma\xi_\gamma + qN_q\xi_\gamma \quad (2.12)$$

where ξ_c , ξ_q and ξ_γ are empirical shape factors to extend the use of the equations to footing shapes other than rectangular strips. A number of values for empirical shape factors have been proposed by various researchers based on experimental studies to extend the use of the bearing capacity equation to axisymmetric foundations.

In order to determine the solution to Equation 2.12 the values of the bearing capacity factors need to be known. Durgunoglu and Mitchell (1973) used an approach of constructing a failure mechanisms for a wedge lodged at different relative depths and used a rigorous approach to determine the bearing capacity factors

and extending them to axisymmetric problems with the aid of shape factors (Figure 2-12). Another approach is to calculate the bearing capacity factors for axisymmetric shapes using the Mohr-Coulomb criterion by constructing failure mechanisms based on a plasticity model. Such a method requires assuming the circumferential stress to be equal to the minor principal stress (known as Haar Von Karman hypothesis) (Durgunoglu and Mitchell, 1973). This approach, which eliminates the use of shape factors but requires a numerical method to solve the equations of equilibrium, has been used by Aubeny et al. (2005) to determine bearing capacity factors for a XBP. Houlsby and Martin (2003) also used the same approach to determine the bearing capacity factors of cone tipped cylindrical offshore footings which is adapted for the probe used in this study. This is described in detail in the next chapter.

2.4.2 *In Situ* Pore Pressure Measurements

In situ measurement of pore pressure in soft marine sediments is crucial to many engineering and hydrogeological applications (Schultheiss, 1990). Short and long term excess pressure data is used to estimate sediment properties such as coefficient of consolidation, permeability and rigidity index (Fang et al., 1993). It is also used in deep sea hydro-geological studies for estimating fluid flow through seafloor sediment (Urgeles et al., 2000).

Typically a tethered probe equipped with pressure sensors is allowed to free fall and penetrate soft sediment. Pore pressures are measured over time intervals ranging from a few hours to multiple tidal cycles. Examples of such probes include

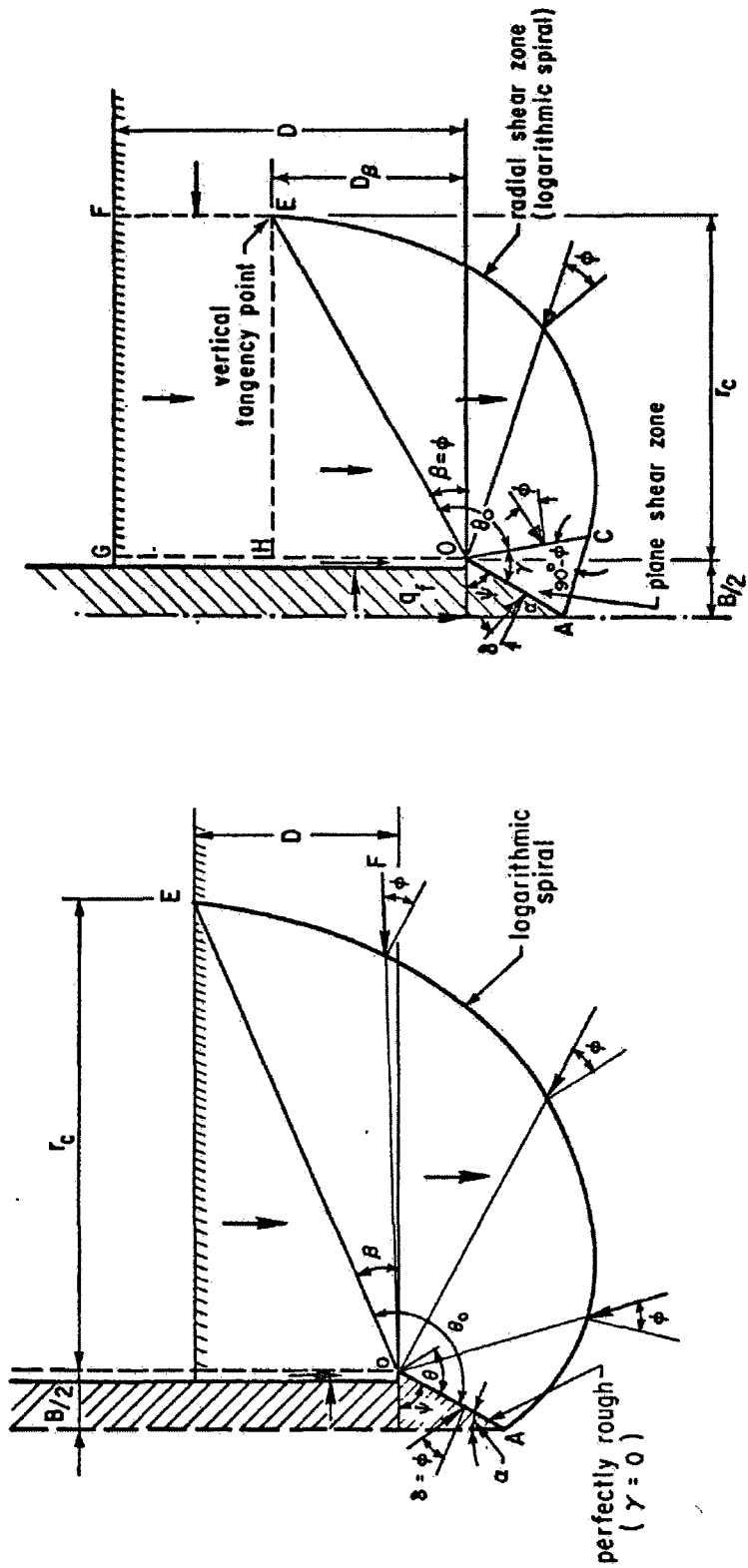


Figure 2-12: Failure mechanism for wedge penetration into soil for small relative depths (left) and large relative depths (right) (Durgunoglu and Mitchell, 1973).

the Pop-up Pore Pressure Instrument (PUPPI) developed by Schultheiss et al. (1985) (see Figure 2-13), the Davis-Villinger Temperature-Pressure probe (DVTP-P)(Davis et al., 1991) (see Figure 2-14)) and Fugro-McClelland Piezoprobe (Moore et al., 2001).

Recently developed free fall penetrometers like the BOT FFCPT and the University of Bremen fCPT, are equipped with pore pressure sensors in addition to accelerometers to enable the simultaneous measurements of sediment strength and excess pore pressure. A more detailed discussion of pore pressure measurements is provided in the next chapter.

2.5 Literature Review

An extensive literature review was conducted to trace the study of impact probes to determine existing practice. The review, summarized chronologically in Table 2.1, provides the basis for the present work.

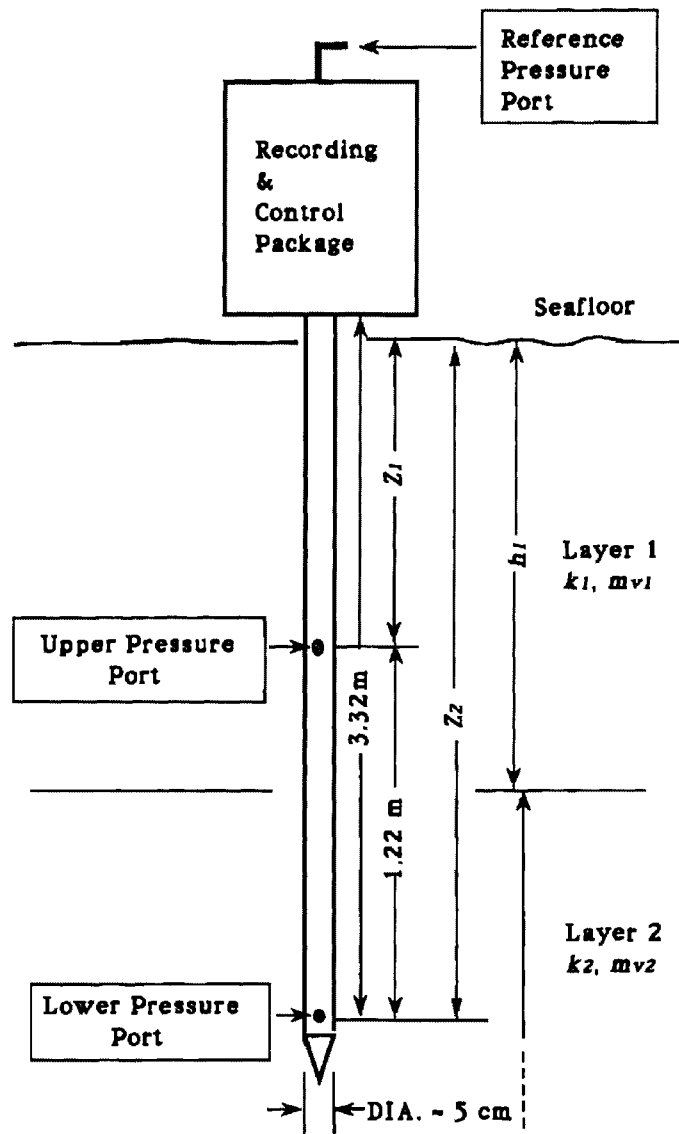


Figure 2-13: A schematic diagram of Pop-Up Pore Pressure Instrument (PUPPI) designed and developed by Schultheiss et al. (1985) (from Fang et al., 1993).

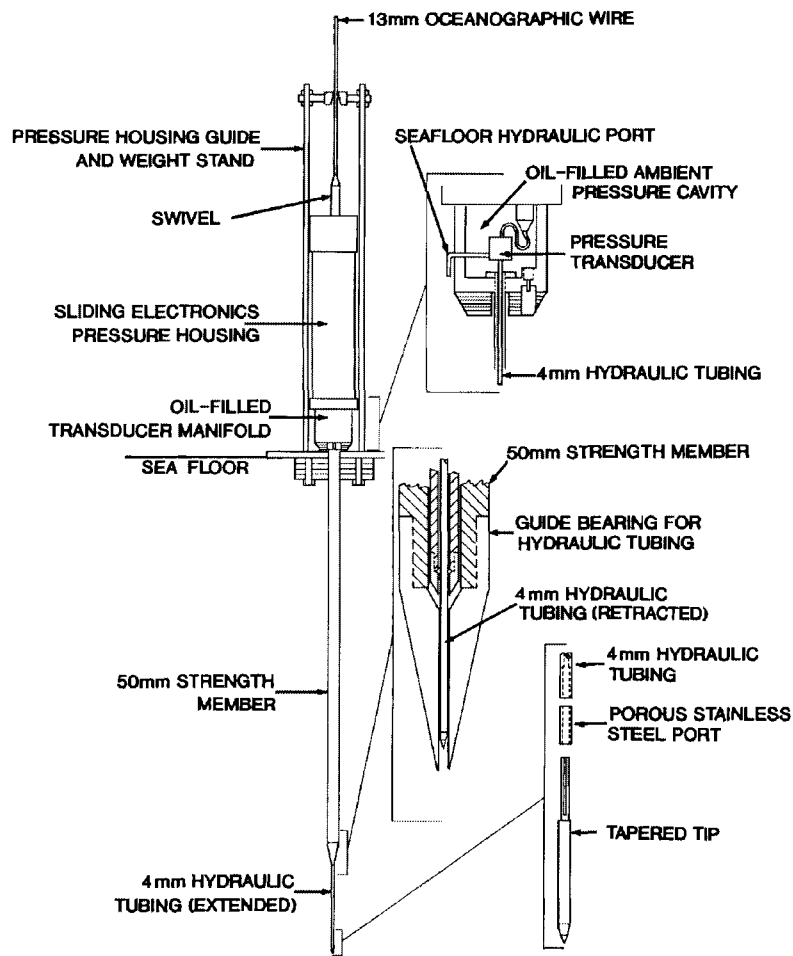


Figure 2-14: Schematic of an early version of Davis-Villinger Temperature-Pressure Piezoprobe (DVTP-P) (from Davis et al., 1991).

Table 2.1: Summary of impact tests.

Author(s)	Soil(s) Investigated	Probe(s) Utilized	Remarks (if any)
Akal and Stoll (1995)	Dense sand to Bentonite clay	Expendable Bathymetric Probe (XBP)	Impact velocities ~ 7 m/s.
Allen et al. (1957)	Sand	Cone-tipped projectile, 1.3 cm diameter	Impact Velocities 608-915 m/s
Aubeny and Dunlap (2003)	Gulf of Mexico Clay in a tank	28.57-76.48 kg, 16.82 cm dia., hemisphere tipped, 0.5048m length	Impact velocities 5.25-7.56 m/s
Awoshika and Cox (1968)	Colorado River Sand, Ottawa Sand	Cone, sphere, circular plate and wedge, 19.5 -58.7 kg	Impact velocities 3.048-7.01 m/s
Beard (1985)	Clays, clayey silts and oozes	Expendable Doppler Penetrometer (XDP)	XDP has been used in water depths upto 6000 m
Chari et al. (1981)	Silty clay	7.5 cm dia., 60° cone, 3.7 m length and 160 kg weight	Impact velocity ~ 10 m/s
Dayal (1981)	Layered sand, gravelly soil, clay powder, sand and mud	60° cone 10 cm^2 area, 6.8-20.4 kg, 3.0 m length	Impact velocities 4.57-6.10 m/s
Denness et al. (1981)	Saturated compacted clay in 0.5m square, 1.0 m deep steel tank	Penetrometer, 3.6 cm dia. cone tipped, 1.135m length and 7 kg weight	Impact velocity ~ 30 m/s

Continued on next page.

Table 2.1 – continued from previous page.

Author(s)	Soil(s) Investigated	Probe(s) Utilized	Remarks (if any)
Fasanella et al. (2001)	Partially saturated soft clay	Hemispherical probe 2.98-24.5 kg, 0.203 -0.66 m dia. hemispheres	Impact velocities 5.74-45 m/s.
Guerin and Goldeberg (2002)	Siliceous clay and clay bearing ooze	Instrumented corer, 22.86 cm dia., 1.20 m length, 34 kg weight	Impact velocities less than 1 m/s. Studies in water depths 5564 and 5587 m
Hembise et al. (1990)	clayey sediments in the Mediterranean sea	0.36 m dia. cone tipped, 3.6 m length, 2000 kg weight	Impact velocities ~ 55 m/s, penetration depths »20
Kelly and Heald (2002)	English Channel sand, gravel and mud	XBP	Impact velocities ~3 m/s
McCarty and Carden (1962), McCarty and Carden (1968)	Concrete, Lead, lightly, loosely and densely packed dry sand, basalt sand and basalt silt	Hemispherical probes, 10.16-30.48 cm dia., 1.0-3.64 kg weight	Impact velocities 6.1-71.3 m/s
McNeill (1981)	Soft silty clay	Penetrators : (a) Cone tipped, 7.62 cm dia. 152.4 cm length, 45.81 kg weight (b)Cone tipped, 22.86 cm dia., 284.48 cm length, 680.3 kg weight	Impact velocities 49.68-55.77 m/s

Continued on next page.

Table 2.1 – continued from previous page.

Author(s)	Soil(s) Investigated	Probe(s) Utilized	Remarks (if any)
Poor et al. (1965)	Partially saturated and dry sandy clay	Plates (25.4 and 50.8 cm dia.), hemispheres (22 cm and 44 cm dia.) and cones (18 cm and 36 cm dia.), 3.62 kg to 58.06 kg weight	Impact velocities 4.52-9.47 m/s
Schultheiss et al. (1985), Fang et al. (1993)	Fine-grained sediments in the deep sea	Pop-up Pore Pressure Instrument (PUPPI)	PUPPI measures post-arrest <i>in situ</i> differential pore pressures
Shi (2005)	Gulf of Mexico clays	XBP	Impact velocities upto 7 m/s. Proposed a rate-dependent predictive model soft sediment
Stegmann et al. (2005) and Stegmann et al. (2006)	Clayey silty sediment (65% to 95% fines)	4.39 cm dia. at tip, 20 cm dia. at tail, 2.114m-2.234m length, 40-170 kg.	Impact velocities ~2 m/s
Stoll et al. (2007)	Saturated granular sediments	XBP	Impact velocities ~7m/s. Reported the dilatative response of granular sediments

Continued on next page.

Table 2.1 – continued from previous page.

Author(s)	Soil(s) Investigated	Probe(s) Utilized	Remarks (if any)
True (1976)	Soft silt, medium silt and cemented material targets	blunt cone, regular cone	
Tarabay and Sanai (1994)	Layer of mud in a tank	7.62 cm dia., 62 cm length conical probe	Impact velocities 12-35 m/s
Turnage (1973)	Fat clay, lean clay and silt at 90% or higher saturation and soft to firm strength level	Cones, rectangular and circular plates 0.323-58.1 cm^2 area	Impact velocities 0.03-12.21m/s
Womack and Cox (1967)	Poorly graded sand, clay and crushed stone	2.93 cm dia., 0.81 cm length, 2.44 kg weight flat plate	Impact velocity ~4.57 m/s
Young (1981)	Partially saturated soft clay	7.6 - 22.2 cm dia., 1.52 m -3.04m length, 45 - 182 kg, flat tipped to 18° cone	Impact velocities 22-76 m/s

2.6 Conclusions from Literature Review

The mechanism of free fall penetration is a complex process. This is mainly due to the high magnitude strain rates and variable drainage conditions that are observed during penetration. In a single penetration event of a free fall probe a wide range of strain rates are observed due to the varying velocity of the probe. The drainage conditions may also vary from undrained, partially drained to fully drained in a single penetration event depending on sediment type. This has been recognized and studied for soft clayey sediment (Dayal and Allen, 1975, True, 1976 and Aubeny and Shi, 2006) and granular cohesionless sediment (Stoll et al., 2007 and Hansen and Gjalson, 2007).

There are a number of variables that influence the penetration process in a free fall penetrometer. A list of variables that affect an impact penetrometer-sediment system have been compiled after a review of literature encompassing studies of impact probes on soil and soil-like materials (see Table 2.2). Many of these variables do not influence CPT (for example impact velocity and peak acceleration). Consequently, the empirical correlations developed for quasi-static CPT are neither proven nor validated to be appropriate for application to the study of free fall probes. The rest of this dissertation seeks to build upon these conclusions by formulating a new analytical model for the evaluations of sediment type, strength and consolidation properties using a free fall penetrometer.

Table 2.2: Variables influencing penetrometer-sediment interaction process.

Variable	Symbol
Cohesion of soil	c
Angle of internal friction	ϕ
Bulk modulus of soil	γ_B
Effective size of soil particles	M_z
Wet mass density of soil	γ_{sat}
Degree of saturation of soil	S_r
Apex angle of cone	β
Mass of probe	M
Embedment depth of probe	z
Acceleration due to gravity	g
Peak Acceleration	a_{max}
Rise time of impact	t_r
Total time of impact	t_t
Velocity of probe impact	v_i
Surface roughness of tip	α_s

CHAPTER 3

FORMULATION OF ANALYTICAL MODEL

3.1 Introduction

The acceleration and pore pressure data collected from the dynamic impact of a free fall penetrometer can be used to interpret important geotechnical properties of seafloor sediments. In this chapter an analytical model is formulated to identify the sediment type and determine undrained shear strength of fine-grained sediment from the acceleration signals. Additionally, a methodology to determine the consolidation properties of fine-grained sediments from post-arrest pore pressure measurements is also described.

3.2 Sediment Classification

Identification of surficial sediment is among the first requirements in many studies of the seafloor. A commonly used parameter to distinguish surficial sediment is mean grain size. A classification convention extensively used in sedimentology is adopted in this study. It is based on Folk and Ward statistics (Folk and Ward, 1957 and Folk, 1966). This system captures characteristics of the grain size distribution curve. Mean grain size(M_z) is given by the following equation:

$$M_z = \frac{\phi_{16} + \phi_{50} + \phi_{84}}{3} \quad (3.1)$$

Table 3.1: Sediment classification based on grain size. M_z is given in "phi" (ϕ) units, based on a logarithmic scale.

Grain Size		Descriptive Terminology
Phi(ϕ)	mm/ μm	from Blott and Pye (2001)
-11 to -10	2048 to 1024 mm	Very Large Boulders
-10 to -9	1024 to 512	Large Boulders
-9 to -8	512 to 256	Medium Boulders
-8 to -7	256 to 128	Small Boulders
-7 to -6	128 to 64	Very Small Boulders
-6 to -5	64 to 32 mm	Very Coarse Gravel
-5 to -4	32 to 16	Coarse Gravel
-4 to -3	16 to 8	Medium Gravel
-3 to -2	8 to 4	Fine Gravel
-2 to -1	4 to 2	Very Fine Gravel
-1 to 0	2 to 1 mm	Very Coarse Sand
0 to 1	1 mm to 500 μm	Coarse Sand
1 to 2	500 to 250	Medium Sand
2 to 3	250 to 125	Fine Sand
3 to 4	125 to 63	Very Fine Sand
4 to 5	63 to 31 μm	Very Coarse Silt
5 to 6	31 to 16	Coarse Silt
6 to 7	16 to 8	Medium Silt
7 to 8	8 to 4	Fine Silt
8 to 9	4 to 2	Very Fine Silt
9 and above	2 μm and finer	Clay

where ϕ_n is the normalized grain size given by the following equation:

$$\phi_n = -\frac{\log_{10} D_n}{\log_{10} 2} \quad (3.2)$$

where D_n is the mean grain size at $n\%$ finer. The value of M_z can be related to the sediment type using a classification system. M_z is given in "phi" (ϕ) units, based on the logarithmic scale described by Equation 3.2 (Table 3.1).

The implicit assumption in using mean grain size is that surficial sediment is homogenous. Prior studies have shown it is not the case and that sediment in the shallow portions of the seafloor commonly consists of lenses as thin as 1 cm. Nev-

ertheless, the use of mean grain size is justified in this study as it represents an important variable that is widely used to relate to other important physical parameters such as bulk density while also providing an indication of the predominant character of surficial sediment.

3.3 Forces Acting on a Freely Falling Probe

A typical free fall penetrometer probe, instrumented with accelerometers and pressure sensors, is dropped from a vessel to impact and penetrate the seabed. The measurements of acceleration of the falling probe are used to determine the velocity and position of the probe as well as to determine the dynamic penetration resistance of the sediments. The pressure sensors measure the dynamic pressure of the probe as it impacts and penetrates the seafloor. Figure 3-1 shows the forces acting on the probe. The following equation is given for vertical equilibrium (True, 1976):

$$F = F_{BE} + F_{AD} + F_D + W_b \quad (3.3)$$

where F_{BE} and F_{AD} are the bearing and adhesion forces respectively. They are dependent on, among other factors, probe geometry and dynamic soil strength. F_D is the inertial drag force given by the following equation given by True:

$$F_D = -A\rho v^2 \sin^2\beta \quad (3.4)$$

where β is the half angle of cone tip, A is the projected frontal area of probe, ρ is the density of the surrounding media, depending on the position of the probe in either the water column or the sediment.

The bearing force (F_{BE}) on the penetrometer is a dynamic parameter that depends primarily on velocity and to a minor degree (in comparison with F_D) on

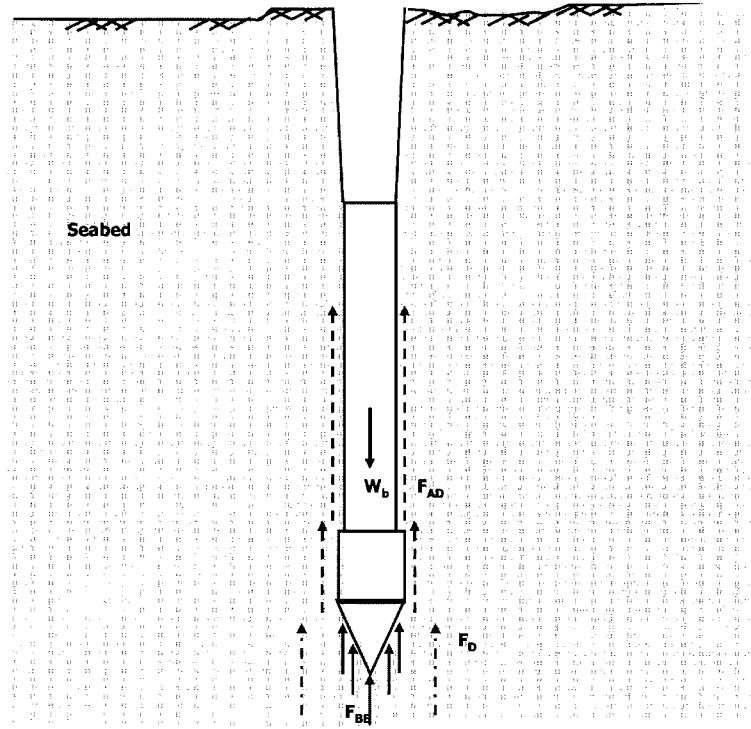


Figure 3-1: Figure showing the forces acting on a free falling penetrometer.

the soil strength, depth of embedment and the patterns of soil deformation (True, 1976). Additionally, soil strength inherently depends on the soil type and on strain rate which itself is dependent on velocity and geometry of the penetrometer. The side adhesion force F_{AD} is dependent on the "smoothness" or "roughness" of the surface of the probe and the cohesion of sediment.

Based on this discussion, the forces experienced by a free falling penetrometer can be given as:

$$\sum F = F_{BE} + F_{AD} + F_D - W_b \quad (3.5)$$

where W_b is the buoyant weight of the probe. These results are necessary to solve the equation of motion to determine the velocity and position of the probe as well as in the evaluation of penetration resistance to determine mechanical strength profiles.

3.4 Characteristics of Acceleration Signals

An individual episode of a free fall penetrometer drop, subsequent to impacting the seafloor, can be divided into four distinct events: (1) impact; (2) embedment; and (3) initial arrest ; and (4) rebound and final arrest, as shown in Figure 3-2(a). These events are captured in a typical acceleration-time signal as shown in Figure 3-2(b). An ideal signal resembles a Gaussian curve with the two inflection points associated with impact and initial arrest respectively. The peak acceleration is given by the apex point in the curve and the rebound and final arrest located beyond the ideal portion of the curve.

Impact occurs when the probe touches the seafloor and transitions from the water column into the sediment. In theory, this is a distinct point on the acceleration-time signal. However, in many cases the exact time is difficult to detect due to the presence of suspended sediment in the sediment-water interface. As a result, this event needs to be detected manually in any analytical model. Embedment of the probe occurs subsequent to impact when the downward momentum drives the probe to penetrate the seafloor. The acceleration reaches a peak (a_{max}) and the time required to reach the peak is given as rise time (t_r).

The probe comes to rest when the sediment resistance overcomes the momentum of the probe but only momentarily before it proceeds to produce a damping oscillatory motion that leads to final rest. This oscillatory motion is analogous to the rebound of a bouncing ball. The location of the initial point of arrest is shown in the acceleration-time signal in Figure 3-2(b). The magnitude of this motion is dependent on the properties of the sediment. Embedment depth (z) is defined as the distance of probe's descent between the point of impact and point of initial arrest. The duration of the drop from impact to initial arrest is termed total duration of drop (t_t) (see Figure 3-2(b)). In the analytical model zero crossings in

the velocity signal obtained from the integration of acceleration with respect to time are used to detect the point of initial arrest of the probe. The utilization of acceleration-time signal, in this dissertation, is limited to the point of initial arrest. The damped oscillatory motion is beyond the scope of this work.

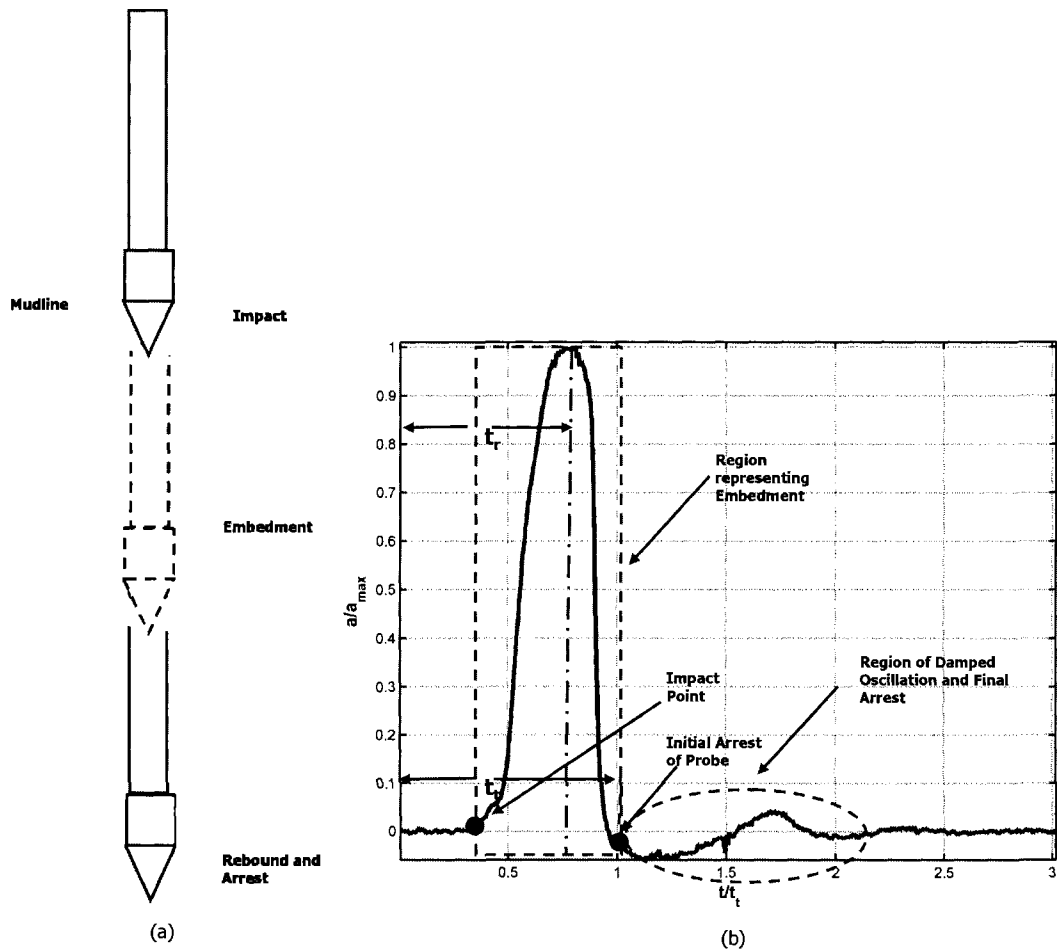


Figure 3-2: (a) Events in a typical impact penetration of seafloor by a free fall penetrometer. (Not to Scale); (b) The location of each event on the acceleration-time signal. The signal is from an actual field drop of a free fall probe.

3.5 Embedment Types

Field deployment of a free fall probe having a constant configuration of tip geometry, diameter and mass in water depths where the probe can reach terminal velocity has shown that the embedment depth is consistently related to sediment type. Embedment depths in softer fine-grained sediment are higher in comparison with drops in coarse-grained sediment. However, the impact velocities of probes can vary widely may due to reasons such as failure to reach terminal velocity due to inadequate water depth or excessive cable drag during deployment. So this variable is studied in relation to other variables affecting a penetrometer-sediment interaction system.

Embedment depth is depicted by the region of the acceleration-time signal shown in Figure 3-2(b). Based on field studies as well as reported work in literature the embedment depths are defined as *shallow*, *intermediate* and *deep* using an arbitrary standard. Figure 3-3 shows the three cases and corresponding shapes of acceleration signals with embedment depths in the range noted. Shallow embedment is defined in this study as normalized embedment less than 5 ($z/D < 5$), where z is the embedment depth and D the diameter of the probe. It is characterized by the symmetrical shape of the acceleration-time signal, similar to a Gaussian curve (Figure 3-3a). The rise time is approximately half the total duration of the signal (Figure 3-3a). Intermediate embedment is defined by the normalized embedment depth range of 5 to 20 ($5 < z/D < 20$). The characteristic shape of the acceleration-time signal is that of a slightly asymmetrical Gaussian curve with a higher rise time (Figure 3-3b). A further increase in embedment depth, beyond deep is observed to significantly distort the Gaussian shape of the curve leading to a low rise time and a high total duration of the signal (Figure 3-3c). The normalized embedment depth for this case is greater than 20 ($z/D > 20$).

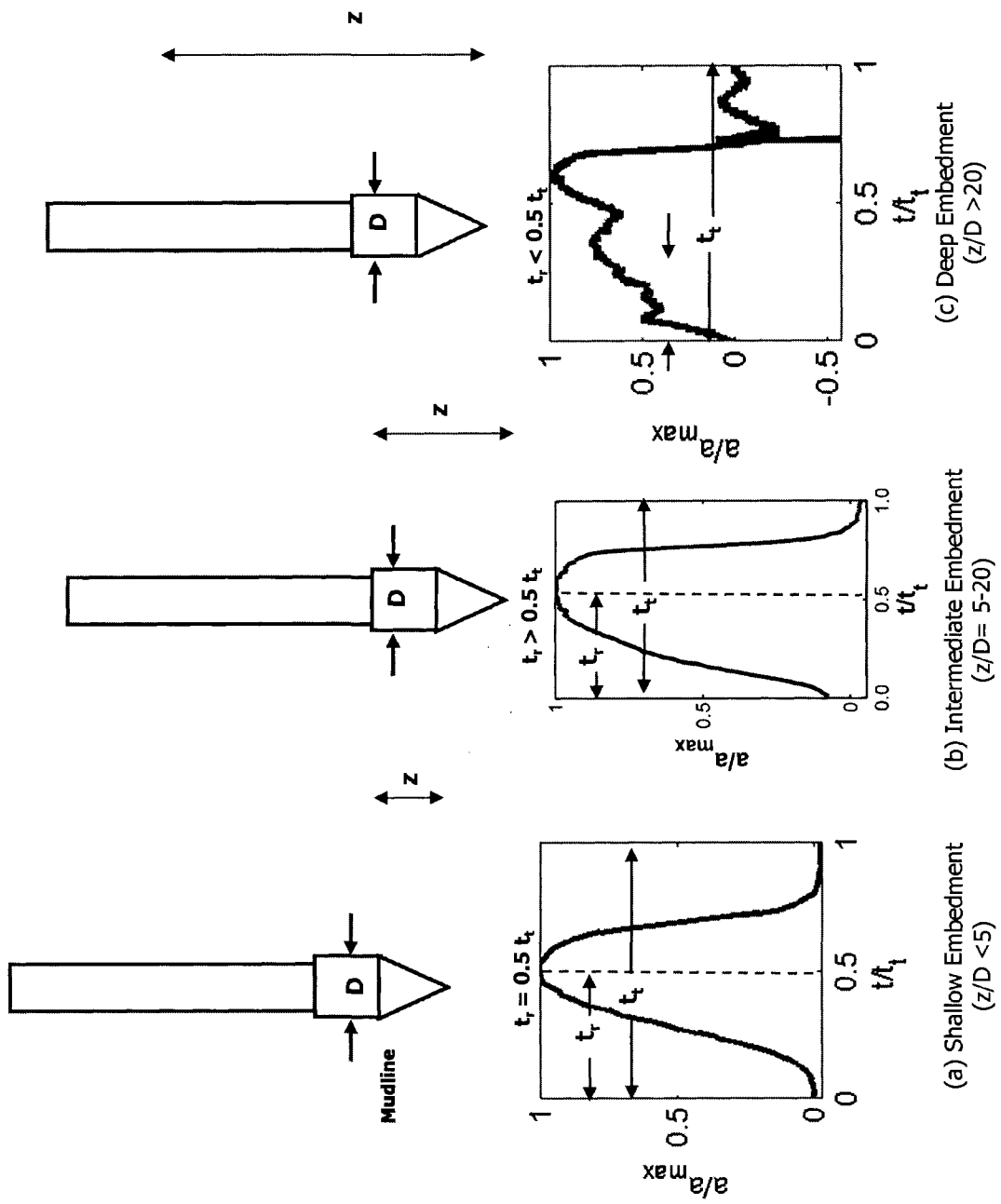


Figure 3-3: Diagram showing three embedment types and their corresponding acceleration-time signal shapes.

3.6 Firmness Scale

Prior studies on projectile-soil systems have shown that information on the target media can be gathered from factors including but not limited to peak acceleration, impact velocity and the total duration of the acceleration-time signal. The exact relationship between these variables depends on the nature of the target media, shape and mass of the probe, and there is no universally accepted relationship validated by experimental data. Nevertheless, the work of McCarty and Carden (1962) in establishing a firmness scale for materials ranging from concrete and lead to sand provides a starting point for studying the characteristic shapes of acceleration-time signals and to relate them with the predominant sediment type of the seafloor.

The firmness scale, originally proposed by McCarty and Carden (1962), was established by plotting $a_{max}/(gv_i)$ against t_t , where a_{max} is the peak acceleration; t_t is the total duration of the acceleration-time signal that encompasses impact, embedment and initial arrest; v_i is the impact velocity and g is the acceleration due to gravity. In order to study the validity of this scale to seafloor sediments, experimental impact test data from various sources, aside from McCarty and Carden (1962), comprising of data from impacts using different probe geometries, masses and targeted media types is used. The developed pattern is shown in Figure 3-4. This logarithmic plot has data points from laboratory and field studies using impact probes. The maximum velocity of impact was limited to 46.1 m/sec, an arbitrary value below which crushing of soil particles is assumed not to have occurred. The summary of the tests data is compiled in Table 3.2.

The following are some important conclusions drawn from the study:

1. There is a relationship of the form $y = ax^b$ between $[a_{max}/(gv_i)]$ and t_t , where $x = [a_{max}/(gv_i)]$ and $y = t_t$.

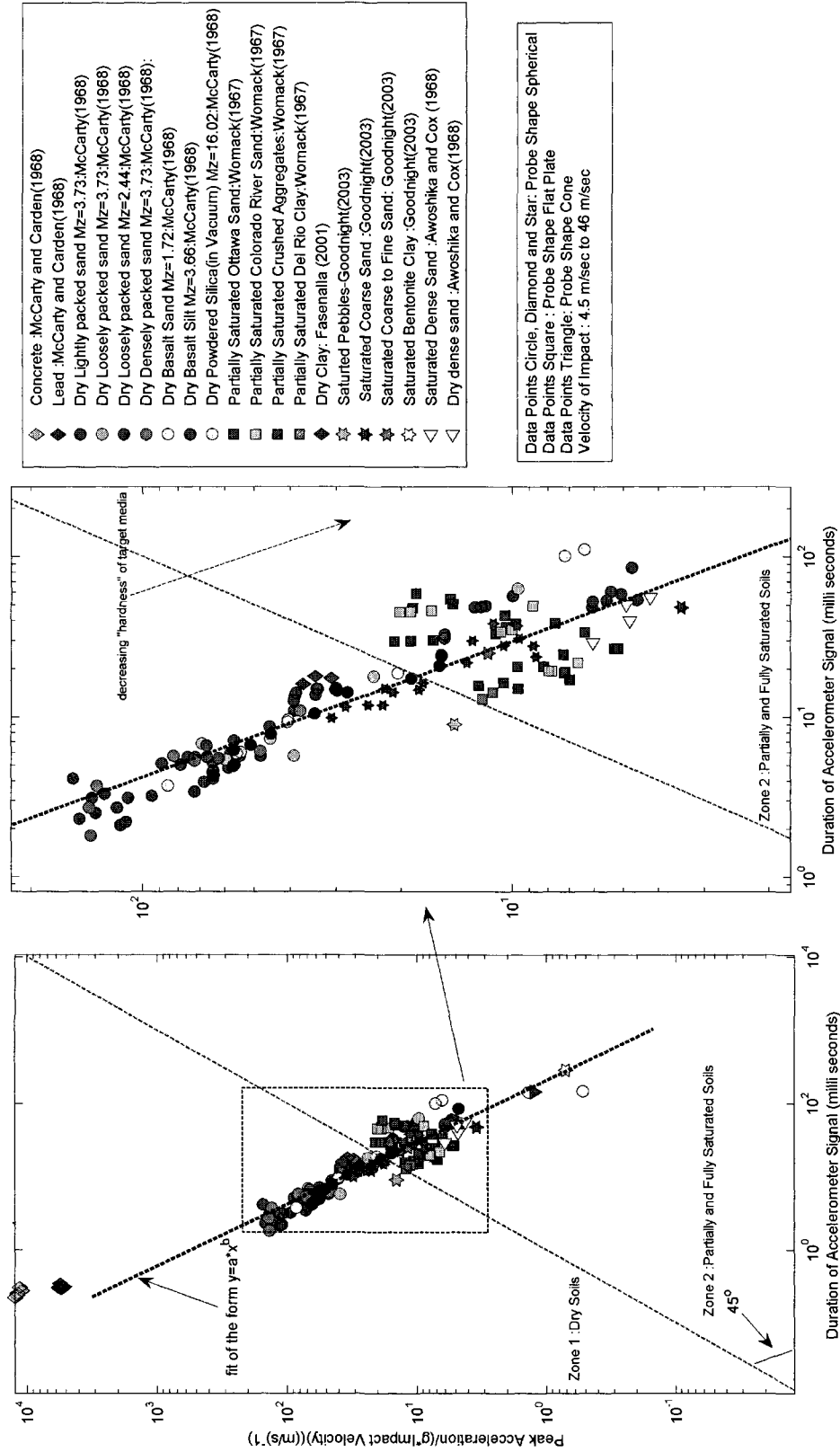


Figure 3-4: A logarithmic plot of peak acceleration (a_{max}) normalized with acceleration due to gravity g and impact velocity (v_i) plotted against total duration of the acceleration-time signal (t_t). The legend gives details of the various sources of the data. The box below the legend gives the details about the various tip shapes. The ratio of y variable over x variable in linear form is defined as firmness factor.

Table 3.2: Summary of impact test data used in developing the firmness scale.

Source	Probe(s)	Target Media	Data Points	v_i (m/s)
Poor et al. (1965)	cones and spheres	Sandy-clay	36	4.5-9.4
Womack and Cox (1967)	flat plates	sand and clay	35	4.3-4.8
McCarty and Carden (1968)	hemispheres	sand, silt, concrete, lead and silica	81	6.1- 46.1
Awoshika and Cox (1968)	cones	sand	6	7.01
Fasanella et al. (2001)	hemispheres	dry clay	4	35 - 45
Goodnight (2003)	sphere	pebbles, sand and clay	3	1.3 - 2.8

2. The normalized embedment depth (z/D) was limited to a maximum of 20 (intermediate embedment) in cases where the data was available or could be determined. The highly distorted shape of acceleration-time signal for z/D greater than 20, discussed earlier in this section, makes it very difficult to pinpoint the location of impact on the acceleration-time signal. In cases where the impact points were chosen approximately the relationship exhibited for the other embedment types (shown in Figure 3-4) was not observed
3. The targeted media type ranges from concrete and lead at the top of the plot, to saturated bentonite clay at the bottom of the plot. The plot clearly captures the pattern of decreasing "firmness" of the targeted media, regardless of the weight and shape of the penetrometer.
4. There is a clear separation between data for dry soils with data for partially and fully saturated sediments, which is indicated by the 45° line that passes through the origin of the logarithmic plot.

5. The duration of acceleration signals increase with decreasing "firmness" of the target media. While this pattern has been reported earlier by McCarty and Carden (1962) based on experiments on dry soils, this study extends it to saturated soils.
6. Saturated media exhibit lower peak accelerations compared with dry media of the same type. This can be explained by energy absorbed by water during impact in saturated media.

Figure 3-4 shows decreasing firmness with increasing t_t for range of targeted media. This establishes the validity of using such a scale to study acceleration-time signals of free fall penetrometer drops in saturated sediments. Based on the firmness scale, a parameter termed firmness factor, F_f , is defined as per the following equation:

$$F_f = \frac{a_{max}}{t_t * g * v_i} \quad (3.6)$$

The firmness scale was plotted in logarithmic coordinates but the firmness factor is defined in linear coordinates as simplify the formulation. The observed correlation between the variables observed in logarithmic mode would also be present in the linear formulation as shown in subsequent work. In the next subsection the discussion of F_f is extended and its effect on normalized embedment depth z/D is studied in relation with mass, tip geometry and impact velocity that provide a basis for proposing a sediment classification model.

3.6.1 Effect of Mass, Tip Geometry and Impact Velocity

The discussion on the firmness scale is extended in this section to study the effect of other factors that are known to influence penetrometer-sediment interaction systems. For this study the firmness factor (F_f) is studied in relation with normalized embedment depth (z/D). The total duration of the acceleration signal, t_t , used

in evaluating F_f is also related to z/D . The higher the value of t_t the higher is z/D . In an ideal acceleration-time signal the two inflection points of a Gaussian curve coincide with the point of impact and point of arrest respectively. However, in reality noise leads to errors during calculations to determine the velocity and position of the probe, thus adding the possibility of an erroneous location of the point of arrest. In order to reduce this error embedment depth (z/D) is introduced into the model.

The effect of probe mass on firmness factor is studied using a logarithmic plot of F_f vs. z/D developed using data from impact tests of conical probes in dry and saturated sand reported by Awoshika and Cox (1968) and shown in Figure 3-5 for two different probe masses. The plot shows that F_f remains in the same linear fit for any change in the mass of a probe.

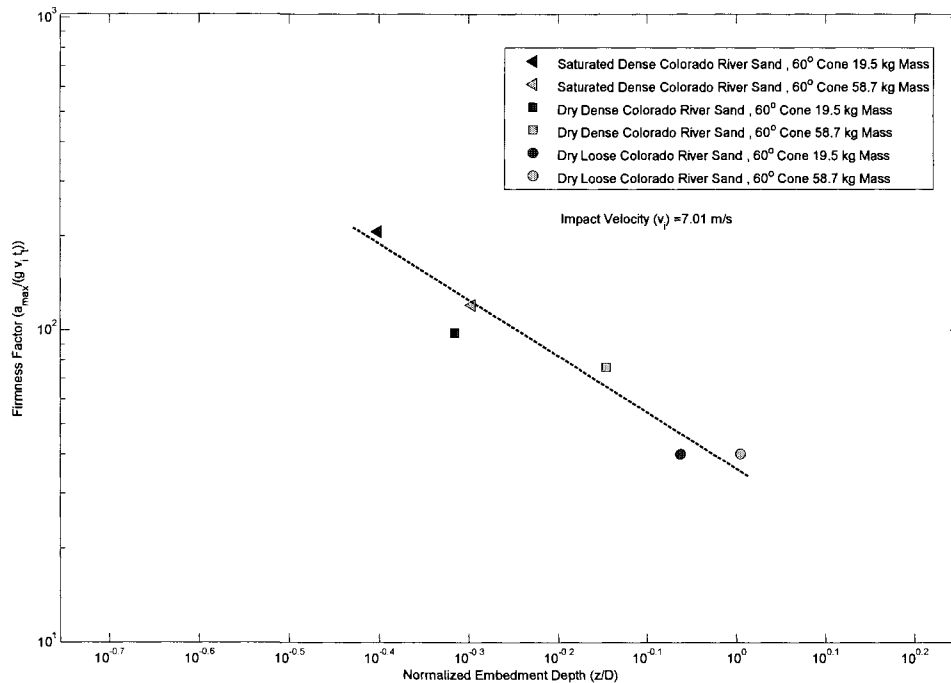


Figure 3-5: Effect of varying probe mass on firmness factor (F_f) (data from Awoshika and Cox, 1968)

The effect of tip geometry on the F_f is studied using data from Poor et al.

(1965). Figure 3-6 shows data from impact tests on cone tipped and spherical probes at impact velocities in the range of 5.9-9.4 m/s. The data shows F_f vs. z/D for two sizes each of cone tipped and spherical probes. It can be observed that cone tipped probes provide higher embedment depths and an increase in diameter results in lower values of F_f .

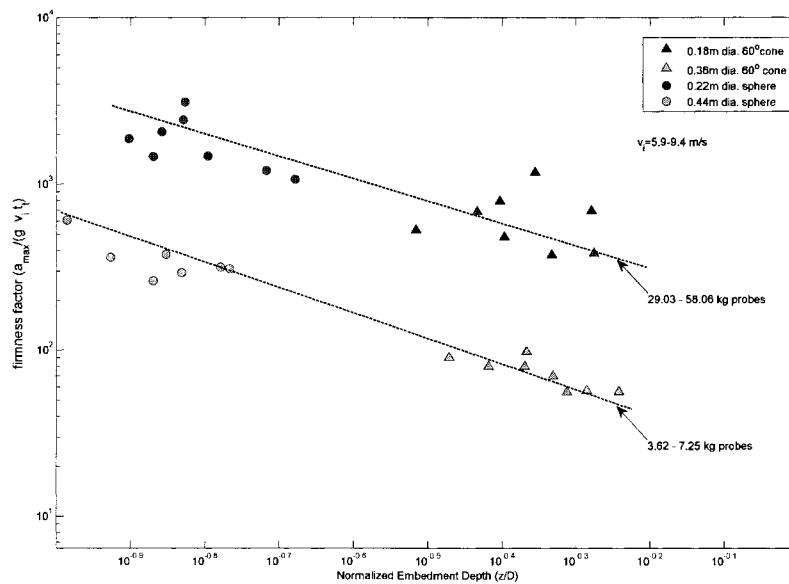


Figure 3-6: Effect of varying probe shape on the firmness factor (data from Poor et al., 1965).

Figure 3-7 shows a plot of F_f vs. z/D from impact tests of hemispherical probes in various target media at two different impact velocities (from McCarty and Carden, 1968). It shows that the variation of "firmness" with respect to embedment depth in coarse-grained soils is closely related to impact velocity. On one hand, for probes with same geometrical properties and mass, the "spread" of the target media response is described by increased length of the curve for relatively low impact velocities. On the other hand the increase in impact velocity (v_i) narrows the "spread" of the firmness factor for the same range of target media tested. Since target media is mostly coarse-grained soils, the increase in impact velocity narrows

the "spread" of the firmness factor over the same range of target media. This suggests that a lower value of impact velocity would provide a wider "spread" of the data points.

Extensive study of data from field investigations described in the next chapter confirm these results leading to a conclusion that for a particular probe with a constant mass and geometrical characteristics the firmness factor and embedment depth provide a consistent response relatable to sediment type. If that probe is deployed within a range of impact velocity these results suggest that firmness factor and embedment depth together can be used to develop a sediment classification model. It must be noted that such a model would be valid only for unconsolidated surficial and near-surface sediment with the assumption that they are homogenous.

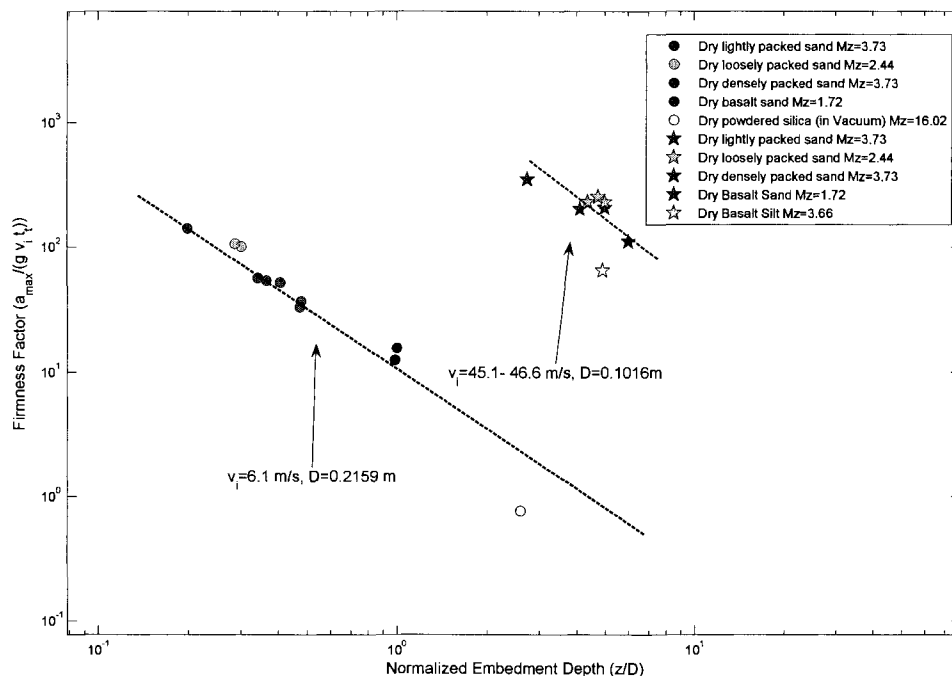


Figure 3-7: Effect of high impact velocity of hemispherical probe on soils.(data from McCarty and Carden, 1968).

3.7 Evaluation of Undrained Shear Strength

3.7.1 Influence of Strain Rate

The dynamic penetration resistance (Q_d), the sum of F_{BE} and F_{AD} , is "sensed" by the accelerometers during the impact and penetration of a free fall probe. If it is assumed that the penetration rate is rapid enough to avoid volume change in the sediment, then the resistance to rapid shearing consists only of a cohesive component and no frictional component. This assumption holds true for sediment with a significant amount of fines, like silts and clays. Q_d can be related to soil strength parameters based on bearing capacity theory: (Lee and Elsworth, 2004)

$$Q_d = N_c S_u A + \sigma_{vo} A_f \quad (3.7)$$

where N_c is a empirical cone factor also referred to as bearing capacity factor, S_u is the undrained shear strength and A_f the frontal area of the probe. The solution of the Equation 3.7 provides a basis of extracting the undrained shear strength profiles provided the empirical cone factor values are chosen appropriately.

Research has shown that stress-strain behavior of fine-grained saturated sediment is influenced by the loading rate (Sheahan et al., 1996). Aubeny and Dunlap (2003), using experiments on free falling cylindrical bodies impacting saturated soft soils, reported that disregarding strain rate underestimated shear strength calculations. Mitchell (1975) explained the behavior using physical principles and showed that shearing resistance increases linearly with the logarithm of strain rate. Dayal and Allen (1975) used these principles to conduct constant rate penetration experiments in saturated clay and proposed a rate dependent equation which can be written as:

$$S_{uv} = S_{uo} [1 + \eta_0 \log_{10}(\frac{\dot{\epsilon}_v}{\dot{\epsilon}_o})] \quad (3.8)$$

where S_{uv} is the rate dependent shear strength, S_{u0} is the shear strength measured at a reference strain rate $\dot{\epsilon}_o$, η_0 is an apparent viscosity parameter that is also referred to as the soil viscosity coefficient and $\dot{\epsilon}_v$ is strain rate at velocity v . The strain rate dependence on the bearing capacity factor can be explained in a manner analogous to Equation 3.8 (Aubeny and Shi, 2007):

$$N_{cv} = N_{co}[1 + \lambda_o \log_{10}(\frac{v}{D\dot{\epsilon}_o})] \quad (3.9)$$

where N_{cv} is the rate dependent bearing capacity factor, N_{co} is the bearing capacity factor at a reference strain rate $\dot{\epsilon}_o$, λ_o is an empirical strain rate parameter and v/D represents the strain rate under consideration. The strain rate dependence on the bearing capacity factor can be explained in a manner analogous to Equation 3.8.

In the Equation 3.9 the reference strain is represented by the equivalent term for cylindrical probes, v/D . λ_o is a strain rate multiplier that has been shown to be equal to η at $z/D = 1$ (Aubeny and Shi, 2007, $\dot{\epsilon}_o$ is a threshold strain rate below which the rate-effects are insignificant. A study by Sheahan et al. (1996) on Boston blue clays provided a value of 0.05%/hr .

Randolph (2004) found that using Equation 3.8 posed numerical stability problems at very low values of strain rate and proposed an alternate equation:

$$S_{uv} = S_{uo}[1 + \dot{\eta}_0 \sinh^{-1}(\frac{v}{D\dot{\epsilon}_o})] \quad (3.10)$$

where $\dot{\eta}_0 = \eta_0 / \ln(10)$. This equation can be extended to bearing capacity factors as described previously:

$$N_{cuv} = N_{co}[1 + \dot{\lambda}_0 \sinh^{-1}(\frac{v}{D\dot{\epsilon}_o})] \quad (3.11)$$

where $\dot{\lambda}_0 = \ln(\lambda_0) / 10$.

The solution to Equation (3.11) and the determination of S_u is dependent upon the use of appropriate bearing capacity factors. There are several approaches to determine them and the next subsection describes the method adopted.

3.7.2 Evaluation of Bearing Capacity Factors

Cohesive sediments in this study are considered to be homogenous, but to account for non-uniform strength conditions a linearly varying strength profile is used. Fig. 3-8 shows a cone tipped penetrometer of diameter ($D = 2R$) embedded in the seafloor. Undrained shear strength S_{u0} at any depth z is given by:

$$S_{u0} = S_{um} + c_1 * z \quad (3.12)$$

where S_{um} is the shear strength at mudline and c_1 is the rate of strength increase with depth. Shear stresses mobilized surface surrounding the cone and body of the probe are denoted using the term τ . It is assumed that the all of the surface of the probe is smooth and frictionless except the conical face. The parameter c_1 can be conveniently expressed as a dimensionless parameter $\eta = \frac{c_1 D}{S_{um}}$.

Bearing capacity factors are empirical factors that are determined using various methods like bearing capacity theory, cavity expansion theory, finite element analysis, strain path analysis and lower bound plasticity analysis (Durgunoglu and Mitchell, 1973; Yu, 2000; Houlsby and Teh, 1988; Teh and Houlsby, 1988 and Houlsby and Wroth, 1982). Among these methods results of prior research using plasticity theory are used in this study. Theoretical background behind the lower bound plasticity method is discussed briefly in the rest of this section.

Plasticity theory is widely used to study problems involving soils at collapse or in an imminent state of collapse. As a probe impacts the seabed and penetrates it induces large strains and stresses in its vicinity, the soil is in a critical state. Such

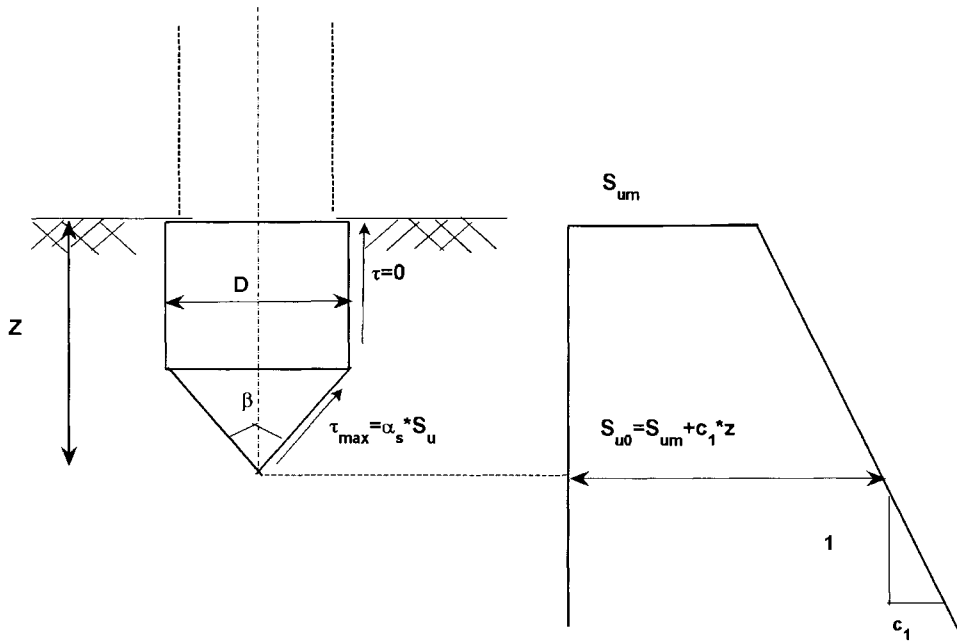


Figure 3-8: Outline of a conical probe and variation of shear strength with depth. Adapted from an illustration by Houlsby and Martin (2003)

an analysis can only be considered a simplified form of solution, because it neglects the large strain aspects of the problem. This approach has been used by Aubeny and Shi (2006) to study the problem of penetration of rigid bodies into the seabed producing realistic results.

Most of the application of plasticity theory to problems in geomechanics is related to the study of deformation in cohesive soils based on a uniqueness theorem given by Drucker (Houlsby and Wroth, 1982). This theorem states that any problem of plastic flow with a particular geometry has a unique load at plastic collapse. The soil is modeled as being rigid-perfectly plastic (Tresca) material with a yield criterion and an associated flow rule. The normalized collapse loads for a conical foundation, also termed cone factors, in Tresca material with an undrained strength S_u given by Houlsby and Martin (2003) are used in this study. The approach has been extensively studied and the results are readily adaptable to the study of cone tipped penetrometers used in this study.

Quasi-static cone factors can be expressed as $N_{c0}(\beta, \alpha, z, \eta)$, where β, α, z and η are apex angle of cone, roughness of cone surface, depth of embedment, rate of strength increase with depth respectively Houlsby and Martin (2003).

Houlsby and Martin (2003) gave the equation that relates the above factors :

$$N_{c0\alpha} + \frac{\alpha}{\tan(\beta/2)} \left[1 + \frac{1}{6 \tan(\beta/2)} \frac{Dc_1}{S_{u0}} \right] \quad (3.13)$$

where $N_{c0\alpha}$ is the contribution of the normal stress on the cone face due to the roughness of the cone surface (α). D is the diameter of the cone. $N_{c0\alpha}$ can then be related to the cone factor produced for a smooth cone face (N_{c00}). A lower bound plasticity analysis gives the equation as:

$$N_{c0\alpha} = N_{c00} \left[(1 + f_1\alpha + f_2\alpha^2) \left(1 - f_3 \frac{h}{D+h} \right) \right] \quad (3.14)$$

for a 60° cone, the values $f_1 = 0.212$ and $f_2 = -0.097$ and $f_3 = 0.53$ (Houlsby and Martin, 2003). The equation for N_{c0} is given as a linear expression of the rate of strength increase with depth.

$$N_{c0} = N_1 + N_2 \frac{Dc_1}{S_{u0}} \quad (3.15)$$

Where $N_1 = N_1(\beta, z/D)$ and $N_2 = N_2(\beta, z/D)$ are generated using the lower bound plasticity analysis given by Houlsby and Martin (2003). c_1 is the rate of strength increase with depth. The following equations provide curve-fitted expressions that are used to calculate N_1 and N_2 :

$$N_1 = N_0(1 - f_8 \cos(\beta/2))(1 + z/D)^{f_6} \quad (3.16)$$

$$N_2 = f_4 + f_5(1/\tan(\beta/2))^{f_6} + f_7(z/D)^2 \quad (3.17)$$

where $f_4 = 0.5$, $f_5 = 0.36$, $f_6 = 1.5$, $f_7 = -0.4$, $f_8 = 0.21$, $f_9 = 0.34$, $N_0 = 5.69$.

The quasi-static bearing capacity factors (cone factors) generated using this methodology are input into the rate-dependent strength model to evaluate undrained shear strength profiles of soft fine-grained sediment using data from free fall penetrometer drops.

3.8 Pore Pressure Dissipation Study

Pore pressures, in excess of hydrostatic pressure, play a vital role in geological processes (Flemings et al., 2008). Free fall penetrometers equipped with pore pressure measurement capabilities have been used to measure the excess pressure response of soft sediment (for example Schultheiss et al., 1985, Fang et al., 1993 and Bennett et al., 2002). Such probes are used to measure the post-impact dynamic pore

pressure and post-arrest dissipation. A free fall probe used for mapping studies encounters a wide variety of sediment. Pore pressure response due to probe impact in sands and other coarse-grained sediments is known to occur in partially drained or drained conditions and is considered to be beyond the scope of this study. A typical signal from pressure sensor located near the cone tip of a FFCPT is shown in Fig. 3-9. The post-impact, also termed post-insertion pressure, consists of the pressure signal during the embedment stage (post-insertion stage) and post-arrest pressure decay. During field testing, it was observed that in coarse-grained sediments the probe usually tips over due to insufficient embedment depth. In fine-grained sediments the embedment depth is sufficient in many cases to retain its vertical position. As a result the post-arrest pore pressure signal provides information on the consolidation properties of the sediments. This study specifically deals with the post-arrest dissipation of pore pressure. A cylindrical-cavity expansion method (CCE) is implemented to solve the diffusion equation data. This method is based on an analytical solution to one-dimensional consolidation equation proposed by Burns and Mayne (2002), that was used to formulate a spherical cavity expansion method (SCE) of pore pressure dissipation in soft fine-grained soils observed using piezocones.

3.8.1 Formulation of Cylindrical Cavity Expansion Model

The vertical effective stress (σ'_v) in homogenous sediment at any commonly given depth is given by Terzaghi's equation:

$$\sigma'_v = \sigma_v - u \quad (3.18)$$

where σ_v is the total vertical stress and u the pore pressure. Effective stresses are important to predicting the strength or deformation behavior of sediment. The

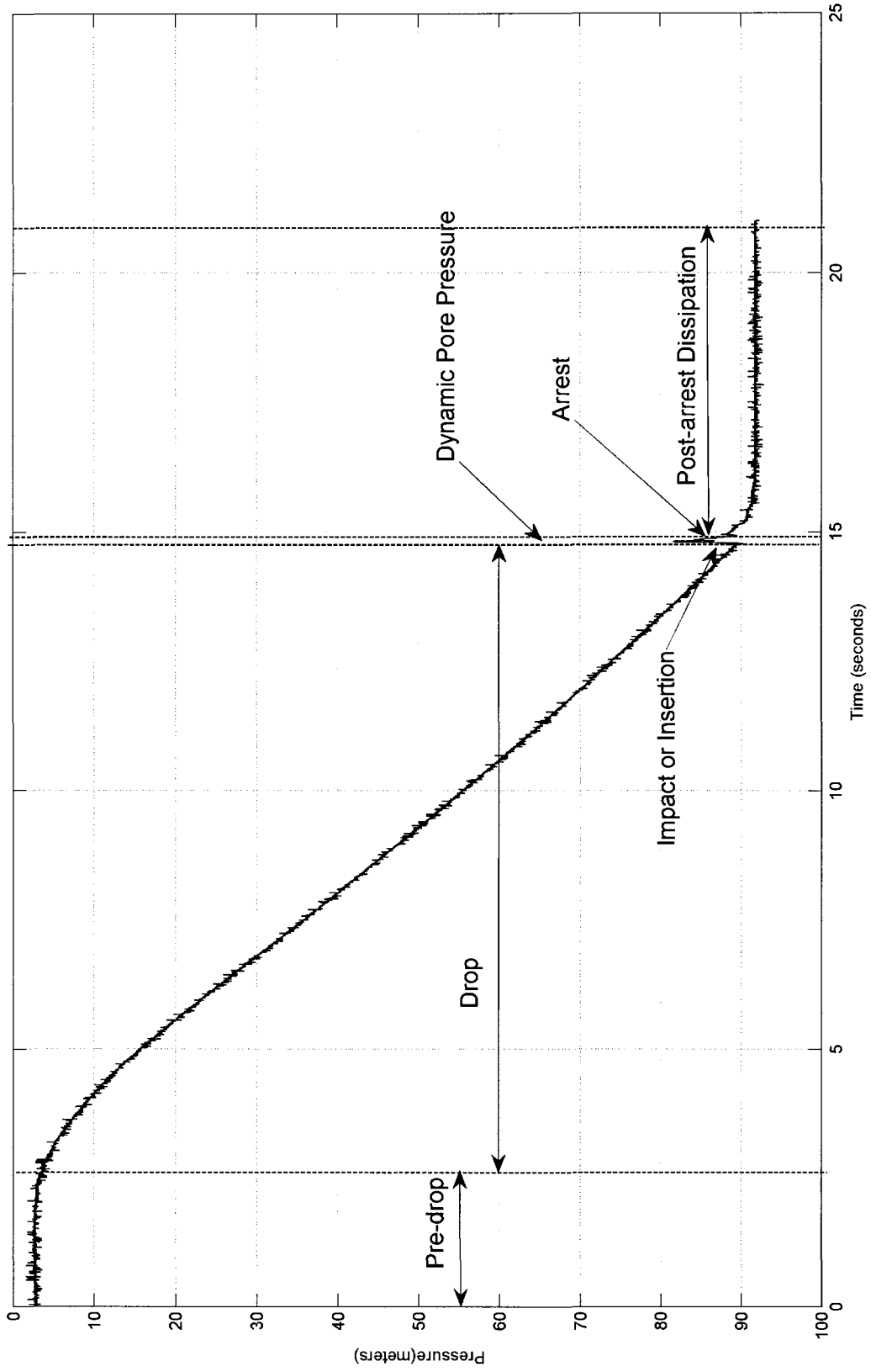


Figure 3-9: Pressure sensor output from the drop of a free fall probe with principal events identified.

excess pore pressure(Δu) at any depth is defined as:

$$\Delta u = u - u_h \quad (3.19)$$

where u_h is the hydrostatic pressure. Figure 3-10 explains the concept of pore pressure based on an illustration from Schultheiss (1990).

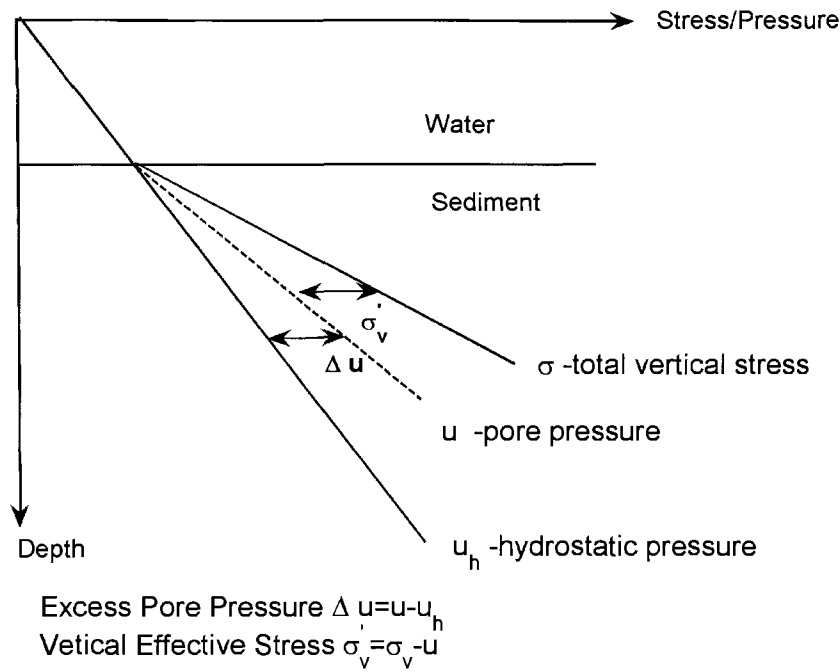


Figure 3-10: Illustration of pore pressure in shallow seabed (based on an illustration by Schultheiss (1990)).

During the penetration of a probe in saturated sediments, pore pressures in excess of hydrostatic pressure are generated due to the change in normal and shear stresses in the sediment. These stresses persist even after the penetration ceases. The pressure sensors measure total pressure during penetration, it can be divided into three components, normal-stress induced, shear-stress induced and pre-existing hydrostatic pressure (Burns and Mayne, 2002). The normal stress induced pore pressure is caused by the physical displacement of sediment and is always posi-

tive in magnitude. The shear-stress induced pore pressure dissipation behavior is dependent on the consolidation state of sediment and the mechanics of penetration. The equation governing the radial dissipation of excess pore pressure is given by the consolidation equation (Mitchell, 1975):

$$\frac{\partial u}{\partial t} = C \left(\frac{\partial^2 u}{\partial r^2} + \frac{\partial u}{r \partial r} \right) \quad (3.20)$$

where u is the excess pore pressure (in kPa) and C (or C_h) the coefficient of radial (or horizontal) consolidation (in m^2/s). The variables r and t are in units of meters and seconds respectively. C_h is related to sediment and fluid properties by the following equation:

$$C_h = \frac{k}{\eta_w m_v} \quad (3.21)$$

where k is the permeability, m_v is the frame compressibility and η_w the viscosity of seawater. This equation is valid in the region of deformation (plastic region), where the excess pressure changes to compensate for the stresses brought about by the creation and expansion of a cavity by the probe (Fig. 3-11). A material model is required to determine the extent of the plastic region. A simple elastic-plastic model is adopted for this study. A cylindrical cavity in an elastic-plastic material expands from a zero value ($r = 0$) to a final radius that equals the radius of the probe ($r = r_{cone}$), where r_{cone} is the radius of the conical tip of the probe. Under undrained conditions the radius of the plastic zone ($r_{plastic}$) is given by: (Randolph and Wroth, 1979):

$$r_{plastic} = (\sqrt{G/S_u}) r_{cone} \quad (3.22)$$

Where G is the shear modulus, S_u the undrained shear strength and (G/S_u) is referred to as the rigidity index (I_r) of the sediment. The maximum excess pressure generated within the fluid due to normal induced stresses using cavity expansion

and valid for a region around the probe, as shown in Fig. 3-11, is given as:

$$u_{max} = S_u \ln(G/S_u) \quad (3.23)$$

In the plastic region defined by $r_{cone} \leq r \leq \sqrt{G/S_u}r_{cone}$ (as shown in Fig. 3-11), the excess pressure generated to compensate for an increase in the average hydrostatic stress is given by:

$$\Delta u = 2S_u[\ln(r_{cone}(\sqrt{G/S_u})/r)] \quad (3.24)$$

3.8.2 Solution for Normal-Stress Induced Pore Pressure

Equation 3.20 is solved using a separation of variables method (Carslaw and Jaeger, 1986). The solution for the partial differential equation (PDE) is of the form :

$$u(r, t) = U(r)T(t) \quad (3.25)$$

substituting this equation in Equation 3.20 gives

$$\frac{U(r)T(t)}{\partial t} = C_h \left[\frac{\partial^2 U(r)}{\partial r^2} + \frac{1}{r} \frac{\partial U(r)}{\partial r} T(t) \right] \quad (3.26)$$

Equation 3.26 is separable. Introducing a separation constant (λ), the solution to Equation (3.20) can be found by solving the following equations:

$$\frac{\partial T(t)}{\partial t} + C_h \lambda^2 T(t) = 0 \quad (3.27)$$

$$\frac{\partial^2 U(r)}{\partial r^2} + \frac{1}{r} \frac{\partial U(r)}{\partial r} + \lambda^2 U(r) = 0 \quad (3.28)$$

This process breaks down the original PDE into two ordinary differential equa-

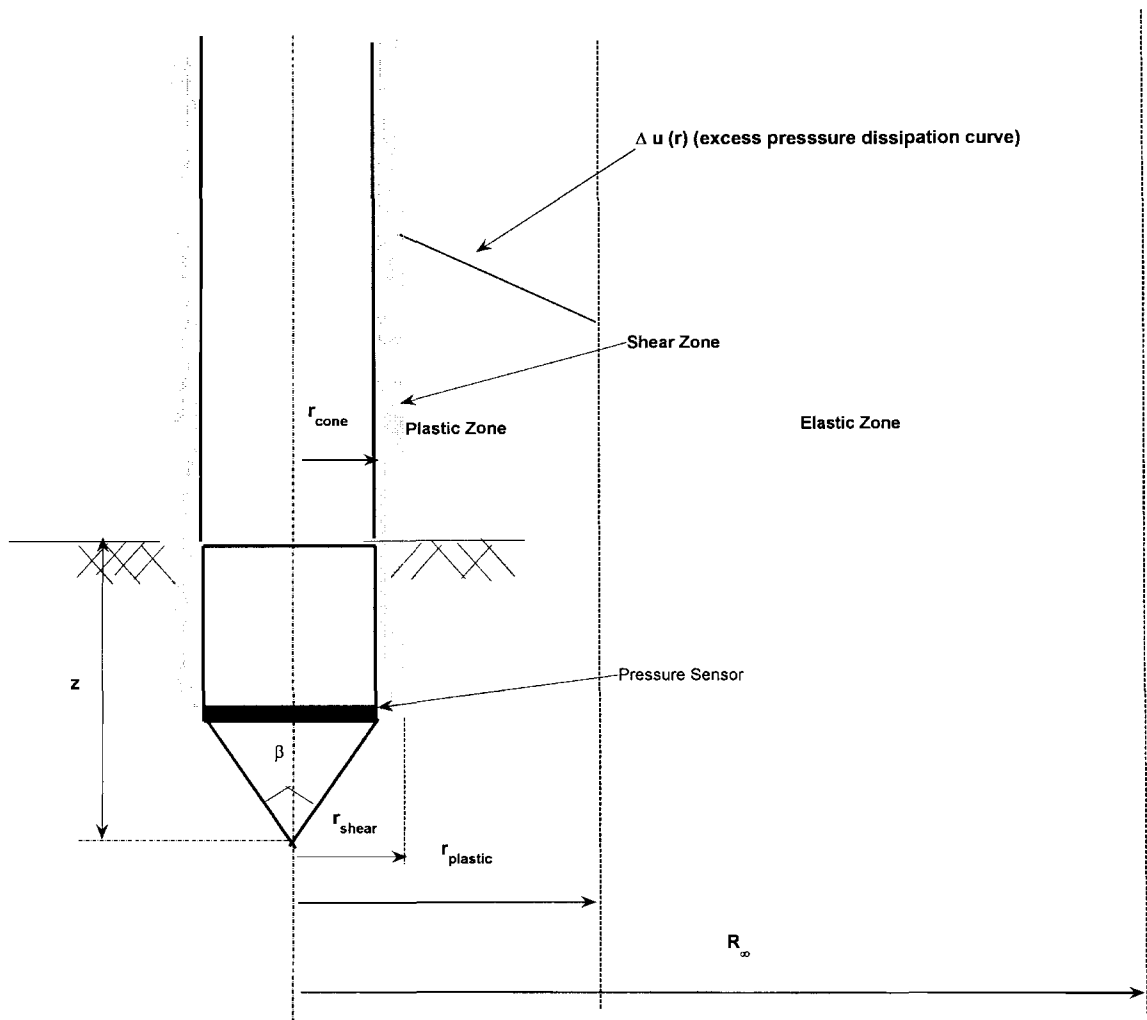


Figure 3-11: Diagram showing details of zones of deformation in sediment surrounding an embedded free fall probe.

tions that can be solved independent of the other. Equation 3.27 is a simple first order ordinary differential equation with a solution of the form:

$$T(t) = Ce^{(-C_h\lambda^2 t)} \quad (3.29)$$

Equation 3.28 is a Bessel's equation of zero order. The solution is of the form:

$$U(r) = AJ_o(\lambda r) + BY_o(\lambda r) \quad (3.30)$$

where J_o and Y_o are Bessel functions of zero order.

The boundary conditions for the original PDE are the following:

$$\partial u / \partial r = 0 \text{ at } r = r_{cone} \quad (3.31)$$

$$u = 0 \text{ at } r = r_{plastic} \quad (3.32)$$

$$(3.33)$$

Using these conditions the separation constant (λ) can be determined by solving the following equation:

$$U(r) = J_o(\lambda r_{plastic})Y_1(\lambda r_{cone}) - Y_o(\lambda r_{plastic})J_1(\lambda r_{cone}) \quad (3.34)$$

where J_1 and Y_1 are Bessel's function of the first order.

The equation however has infinite roots. Randolph and Wroth (1979) showed that the sum of the first 50 roots was sufficient enough for accuracy in such cases. Providing the initial condition imposed by the expansion of cylindrical cavity at $t = 0$:

$$u = 2S_u[\ln(r_p\sqrt{G/S_u}/r)] \quad (3.35)$$

The final solution to the normal-stress induced pore pressure is given by :

$$\sum_{n=1}^{\infty} B_n e^{-C_h \lambda^2 t} [-Y_o(\lambda_n r) J_o(\lambda_n r_{plastic}) + Y_o(\lambda_n r_{plastic}) J_o(\lambda_n r)] \quad (3.36)$$

where B_n is given by the following equation:

$$B_n = \frac{2S_u \int_{r_{cone}}^{r_{plastic}} B_{n1} B_{n2} dr}{\int_{r_{cone}}^{r_{plastic}} B_{n3} dr} \quad (3.37)$$

where B_{n1} , B_{n2} and B_{n3} are given by the following equations:

$$B_{n1} = r \left[\ln \left(\frac{r_{cone}}{r} \sqrt{\frac{G}{S_u}} \right) \right] \quad (3.38)$$

$$B_{n2} = Y_o(\lambda_n r) J_o(\lambda_n r_{plastic}) - J_o(\lambda_n r_{plastic}) Y_o(\lambda_n r) \quad (3.39)$$

$$B_{n3} = r [Y_o(\lambda_n r_{plastic}) J_o(\lambda_n r_{plastic}) - J_o(\lambda_n r_{plastic}) Y_o(\lambda_n r)]^2 \quad (3.40)$$

$$(3.41)$$

3.8.3 Solution for Shear-Stress Induced Pore Pressure

An analytical solution using a similar approach for increase in shear-stress induced pore pressure was given by Burns and Mayne (2002) using a Modified Cam Clay (MCC) soil model. Shear-stress induced pressure is assumed to influence a thin annulus of radius, r_{shear} , surrounding the probe. The annulus was assumed to be 2-10 mm thick (shown in Fig. 3-11). The variation of this pressure is assumed to be linear over the thickness. Thus, giving the equation for shear-stress induced pressure as:

$$u(r) = \frac{\sigma'_{vo} [1 - (0.5OCR)^\Lambda] r - \sigma'_{vo} [1 - (0.5OCR)^\Lambda] r_{shear}}{r_{cone} - r_{shear}} \quad (3.42)$$

where OCR is the overconsolidation ratio and Λ is the plastic volumetric strain ratio derived from soil testing. A value of $\Lambda = 0.8$ is used throughout this study (Burns and Mayne, 2002). The Overconsolidation ratio is a measure of the stress history of the sediment under consideration. It is given by the ratio of the pre-consolidation stress to the present vertical effective stress. Soils with $OCR = 1$ are considered normally consolidated, with $OCR > 1$ are overconsolidated soils and with $OCR < 1$ are underconsolidated soils. Applying an approach similar to the one previously taken and using boundary conditions (at $r = r_{shear}$, $u = 0$ and $r = r_{cone}$, $\frac{\partial u}{\partial t} = 0$), Burns and Mayne (2002) solved for shear stress induced pore pressure as :

$$u = \sum_{n=1}^{\infty} A_n e^{-C_h \beta^2 t} [-Y_o(\beta_n r) J_o(\lambda_n r_{shear}) + Y_o(\beta_n r_{shear}) J_o(\lambda_n r)] \quad (3.43)$$

A_n is given by an equation of the form:

$$A_n = \frac{\int_{r_{cone}}^{r_{shear}} A_{n1} A_{n2} dr}{\int_{r_{cone}}^{r_{shear}} A_{n3} dr} \quad (3.44)$$

A_{n1} , A_{n2} and A_{n3} are given by the following equations:

$$A_{n1} = r \frac{\sigma'_{vo} [1 - (0.5OCR)^\Lambda] r - \sigma'_{vo} [1 - (0.5OCR)^\Lambda] r_{shear}}{r_{cone} - r_{shear}} \quad (3.45)$$

$$A_{n2} = Y_o(\beta_n r_{shear}) J_o(\beta_n r) - J_o(\beta_n r_{shear}) Y_o(\beta_n r) \quad (3.46)$$

$$A_{n3} = r [Y_o(\beta_n r_{shear}) J_o(\beta_n r) - J_o(\beta_n r_{shear}) Y_o(\beta_n r)]^2 \quad (3.47)$$

$$(3.48)$$

The complete solution to the problem of pore pressure dissipation after the pen-

etration and arrest of a penetrometer is given by combining the solutions from Equations. 3.36 and 3.43.

3.8.4 Model Validation and Analysis of Results

The model is validated for dissipation test data of a piezocone at three sites documented in Burns and Mayne (2002). A summary of relevant input parameters is given in Table 3.3. The results are compared with results of a spherical cavity expansion model given by Burns and Mayne (2002) along with reported field measurements.

Figures 3-12 - 3-14 show results of CCE model test comparison with SCE model test data and field measurements of excess pore pressure. The CCE model provides a good comparison with field measurements validating the model and its application to such problems. However, the CCE model under-predicts excess pressure in comparison with the SCE model. This can be attributed to the differences in the underlying premise of each model, cylindrical and spherical cavity as the zone of dissipation respectively. This also suggests that analyzing the CCE model with a different set of assumed input values, including (G/S_u) , will produce a different set of dissipation curves.

The model is further analyzed to study the contribution of each component of pore pressure in the total modeled pressure. Figures 3-15 - 3-17 show the individual components of total pressure plotted against time. Figures 3-15 and 3-16, which represent data from slightly overconsolidated clays with a high rigidity index (G/S_u) , show that the component of shear-induced pore pressure is small in comparison with the total pressure. The shear-stress induced pore pressure is a large component of total pressure for highly overconsolidated stiff clays (Figure 3-17).

The CCE model could be applied to long term dissipation data from free fall probes. This can be accomplished by adapting an iterative procedure to fit the

Table 3.3: Summary of CCE model input parameters (from Burns and Mayne (2002)).

Site	Onsøy, Norway	Cowden, UK	Madingley, UK
z (m)	18.5	17.2	11.2
u_h	159.4	95.0	90.0
σ'_o (kPa)	1.4	283.4	122.8
OCR	1.4	3.4	26
S_u (kPa)	49	140	185
G (kPa)	6066.2	34328.0	357.0
Model Predicted $C_h(mm^2/s)$	0.04	0.25	0.008
Lab Measured $C_v(mm^2/s)$	0.44-0.79	0.05-0.19	0.03-0.08

model data to the dissipation curves and reporting the assumed values of permeability and other sediment properties. Fang et al. (1993) reported the use of such an approach to predict permeability and other properties by solving the diffusion equation using a finite difference approach and neglecting the contribution of shear-stress induced pore pressure in the model. In overconsolidated sediments, prior knowledge of OCR is required to predict permeability and other consolidation properties.

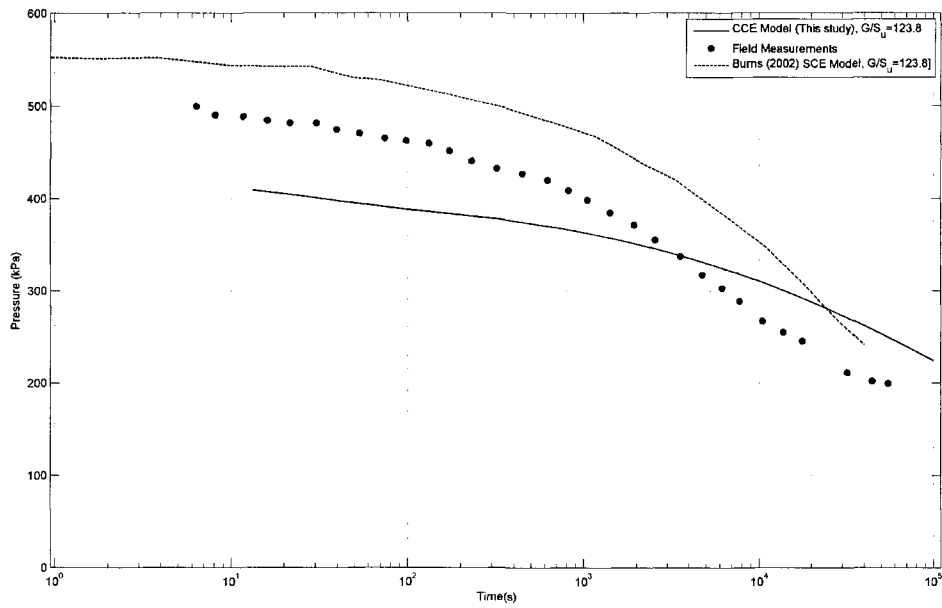


Figure 3-12: Measured and modeled pore pressure dissipation at depth of 18.5 m in a soft clay site in Onsøy, Norway. The field measurements were originally reported by Lacasse and Lunne (1982) and collected from Burns and Mayne (2002) along with the SCE model data. $OCR = 1.4$, $S_u = 49$ kPa and $C_h = 0.04$ mm^2/s .

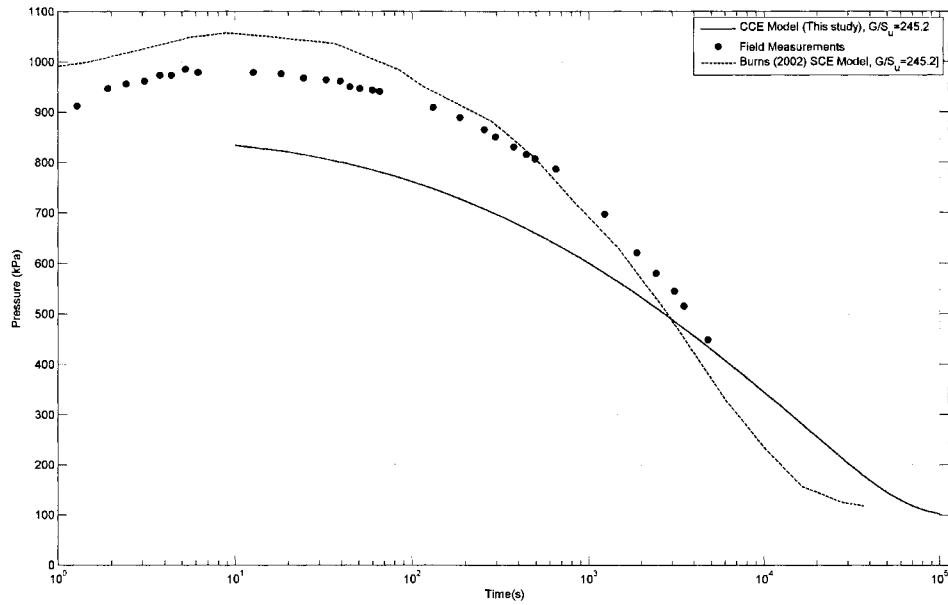


Figure 3-13: Measured and modeled pore pressure dissipation in a stiff clay at a depth of 17.2 m in a site in Cowden, UK. The field measurements were originally reported by Lunne et al. (1985) and collected from Burns and Mayne (2002) along with the SCE model data. $OCR = 3.4$, $S_u = 140$ kPa and $C_h = 0.25$ mm²/s.

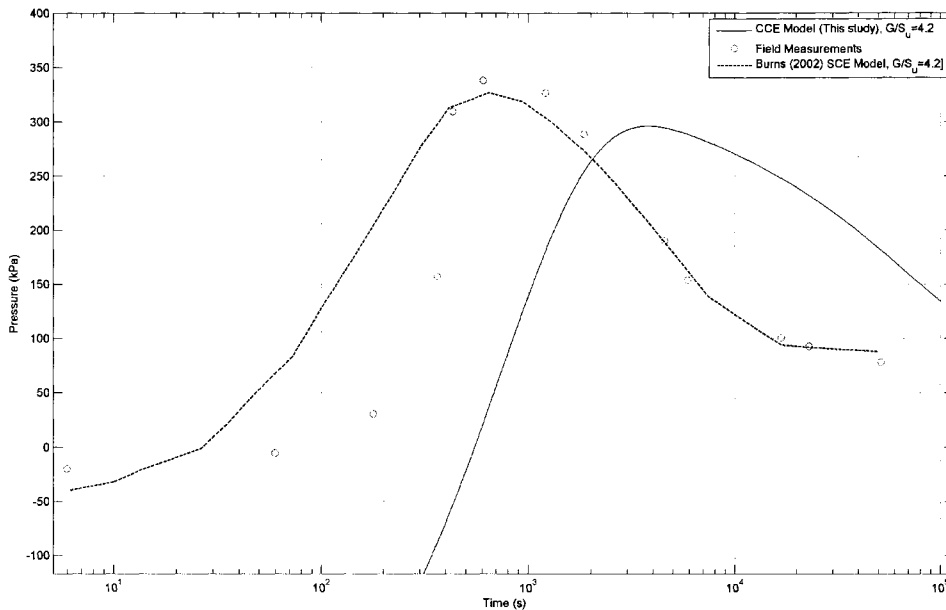


Figure 3-14: Measured and modeled pore pressure dissipation in a highly overconsolidated stiff clay at a depth of 11.2 m. The field measurements were originally reported by Lunne et al. (1986) and collected from Burns and Mayne (2002) along with the SCE model data. $OCR = 26$, $S_u = 185$ kPa and $C_h = 0.008$ mm²/s.

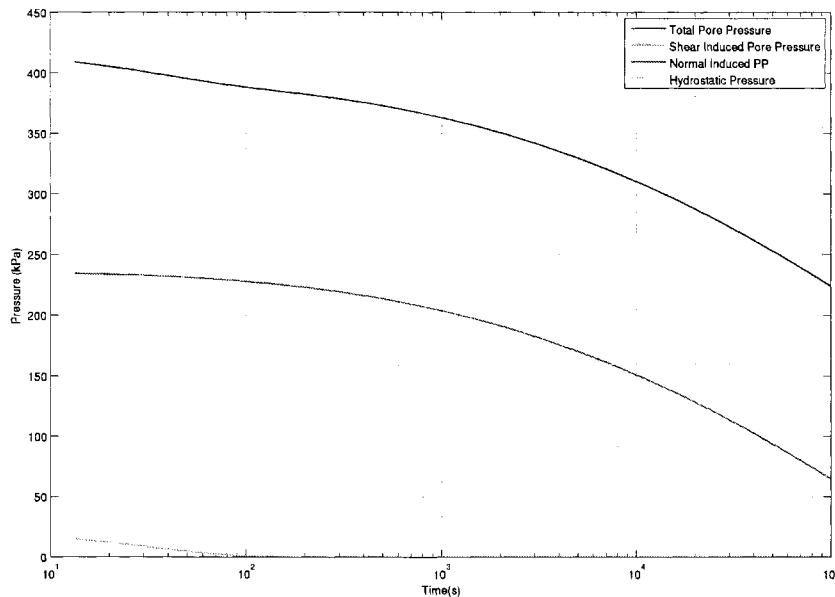


Figure 3-15: Plot showing the contribution of individual components of total pressure at a soft clay site in Onsøy, Norway. $OCR = 1.4$, $S_u = 49$ kPa and $C_h = 0.04$ mm²/s.

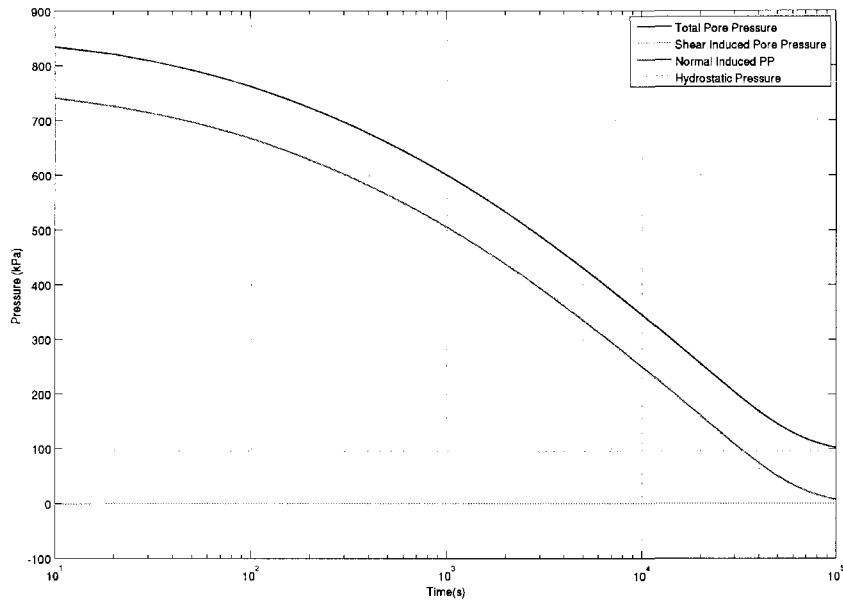


Figure 3-16: Plot showing the contribution of individual components of total pressure at a stiff clay site in Cowden, UK. $OCR = 3.4$, $S_u = 140$ kPa and $C_h = 0.25$ mm^2/s .

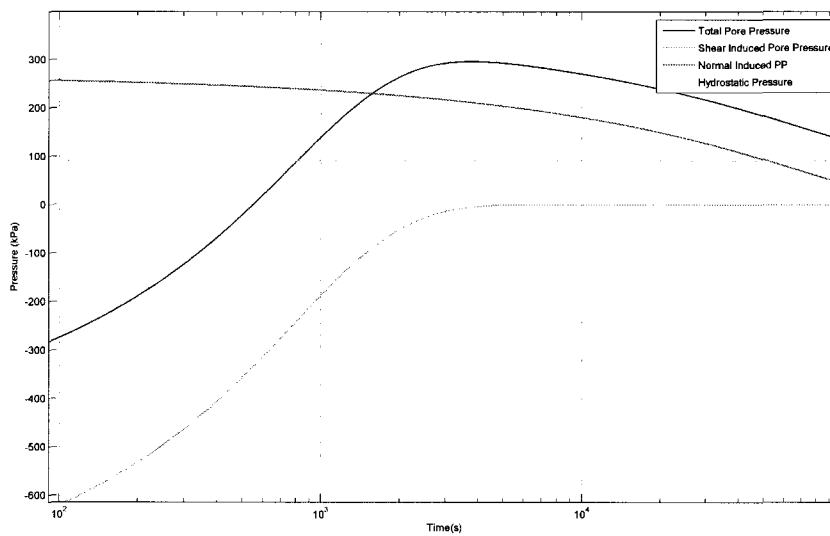


Figure 3-17: Plot showing the contribution of individual components of total pressure at a stiff clay site in Madingley, UK. $OCR = 26$, $S_u = 185$ kPa and $C_h = 0.008$ mm^2/s .

CHAPTER 4

FIELD DEPLOYMENT PROGRAM

4.1 Objectives and Approach

A field deployment program was implemented to study the correlation of sediment type to acceleration and pore pressure signals and the influence of strain rate on penetration resistance in fine-grained sediments. A separate study to validate the undrained shear strength profiles derived from the analytical model are described in this chapter.

Data was collected from four field stations totaling 24 drops in the Piscataqua River, off Portsmouth and New Castle, New Hampshire. A description of additional field testing data collected from Bering Sea, Alaska conducted as part of mapping habitat needs for Essential Fish Habitat (EFH) studies.

4.2 The Free Fall Cone Penetrometer (FFCPT)

An experimental Free Fall Cone Penetrometer (FFCPT) designed by Brooke Ocean Technologies Inc. (BOT) and on loan from the US Army Corp of Engineers to the University of New Hampshire. It is technologically a new generation free fall probe. The probe, termed UNH FFCPT is shown in Figure 4-1 with the different modules identified. The length of the probe is 1.572 m, the mass is 39.46 kg, and cone diameter is 0.088m. The sensor module houses three accelerometers calibrated for three different acceleration ranges and a nose or tip pressure sensor designed to

measure dynamic pore pressure. The ballast module consists of ballast weight. The electronic module houses the onboard microprocessor. The battery module consists of a 12 V battery pack and the bale and pressure sensor module houses the tail pressure sensor that can measure water depths up to 150 m.

In addition to the UNH FFCPT, data from another developed by the same company and provided by Alaska Fisheries Science Center (AFSC) in Seattle, Washington was also used in this study. This probe, termed AFSC FFCPT, has some slightly different design parameters. Figure 4-2 shows a photograph of a unit similar to the AFSC FFCPT (from Osler et al. (2006)). Table 4.1 summarizes some important parameters of both the probes.

Table 4.1: Configuration of UNH and AFSC probes.

Parameter	UNH Probe	AFSC Probe
Length(meters)	1.498	1.820
Weight(kg)	47.60	39.46
Cone Angle(degrees)	60	60
Cone Diameter(inches/meters)	4.5/0.1143	3.5/0.0889
Cross Sectional Area(cm ²)	102.6	62.07

4.3 Pre-deployment Assembly and Testing

Tasks prior to deployment involves assembling and testing the performance of the FFCPT. These tasks are summarized as follows:

1. **Probe Assembly:** The FFCPT is shipped and stored in individual modules that need assembly prior to each deployment. Fig. 4-3 shows the fully assembled FFCPT .
2. **Laboratory Testing:** Each of the sensors and accelerometers were calibrated prior to a major deployment. The calibration factors from the latest

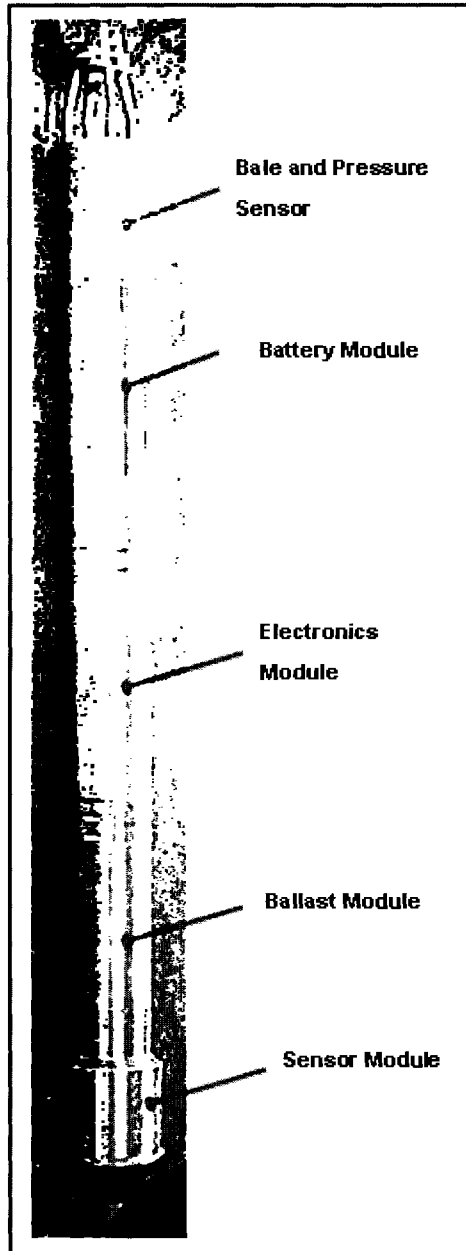


Figure 4-1: Photograph identifying the various modules in the FFCPT (Photo provided by Prof. Jeff Melton).

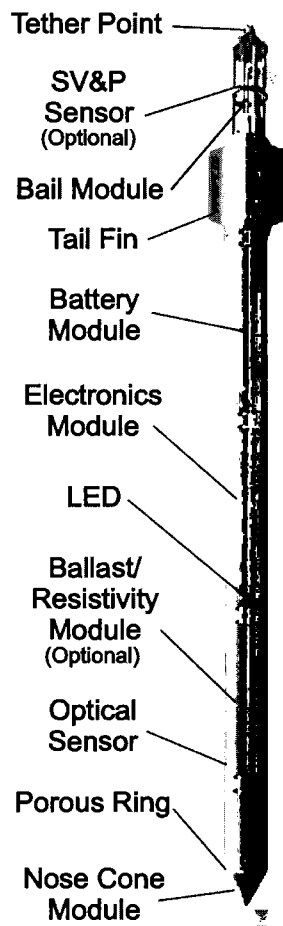


Figure 4-2: Photograph showing a unit similar to the AFSC FFCPT with various modules identified (from Osler et al. (2006)).

testing performed by BOT were used in FFCPT in laboratory testing at the Engineering Tank, at the Center for Ocean Engineering. This testing was conducted prior to every deployment so as to ascertain the performance of the pressure sensors and accelerometers in air as well as underwater. Fig. 4-4 shows testing of the performance of the FFCPT underwater. The tests include hanging the probe vertically to check the accelerometer signal and dropping the probe into a drum filled with sand. Figures 4-5 and 4-6 show the output of the accelerometers, pressure sensors and optical backscatter sensors for the tests. An air compressor was used to artificially increase the tail pressure sensor to simulate pressures higher than atmospheric pressure.

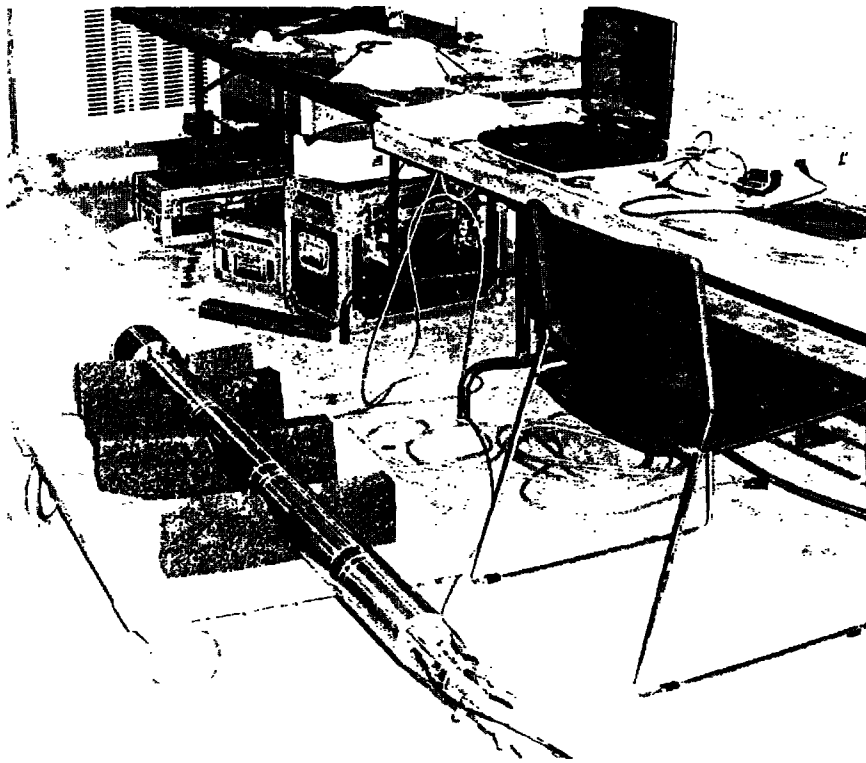


Figure 4-3: A fully assembled FFCPT probe being tested at the Center for Ocean Engineering.

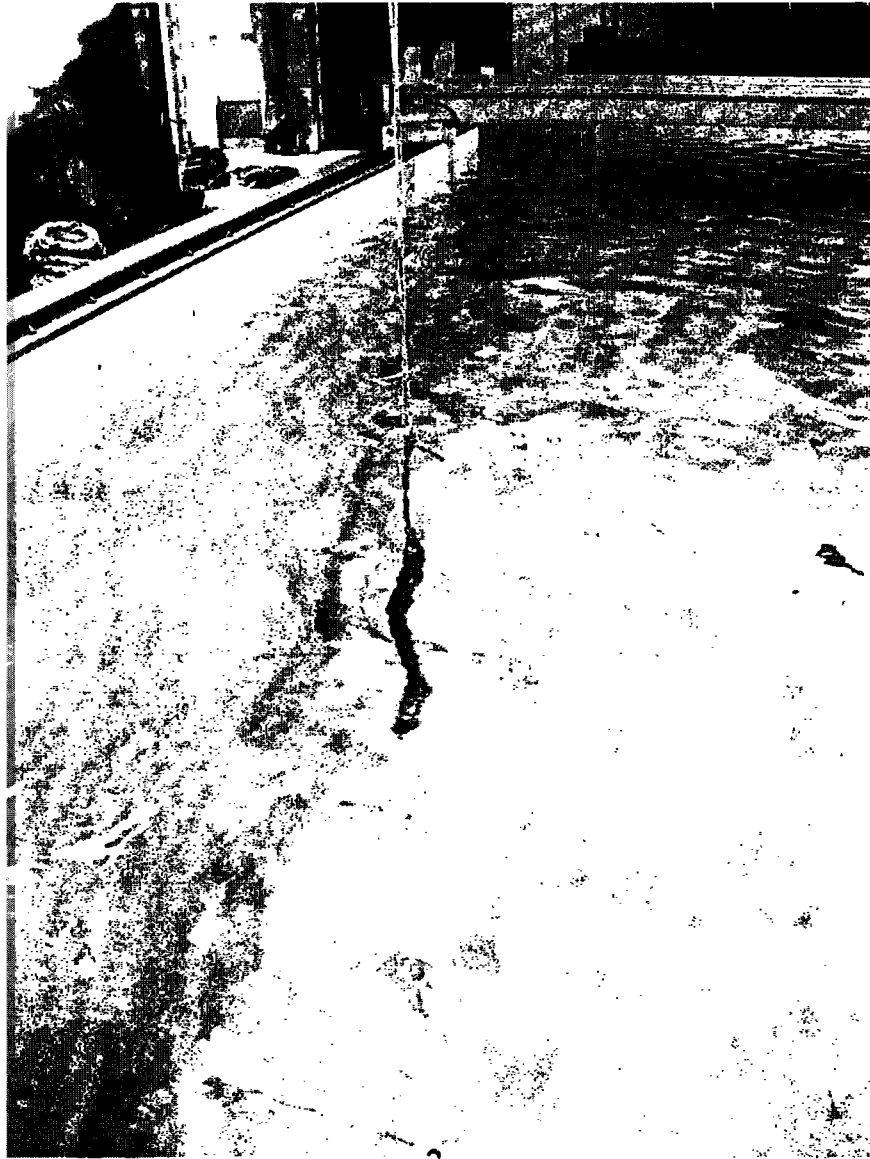


Figure 4-4: The FFCPT being tested for performance underwater.

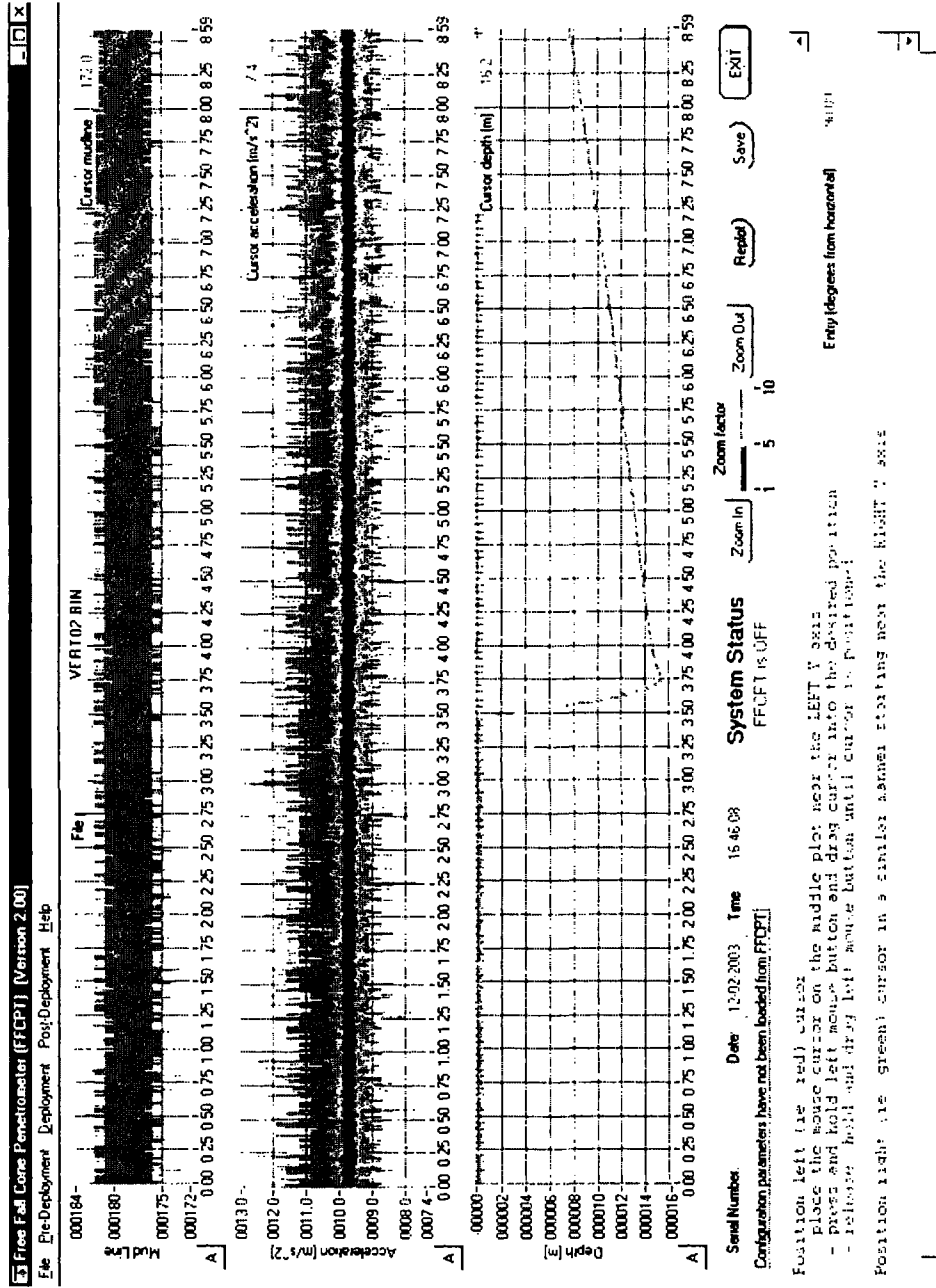


Figure 4-5: The raw data output of a vertically positioned FFCPT in air using company supplied software. Pressure supplied to tail pressure sensor using an air compressor for a trigger pressure of 10.0 m.

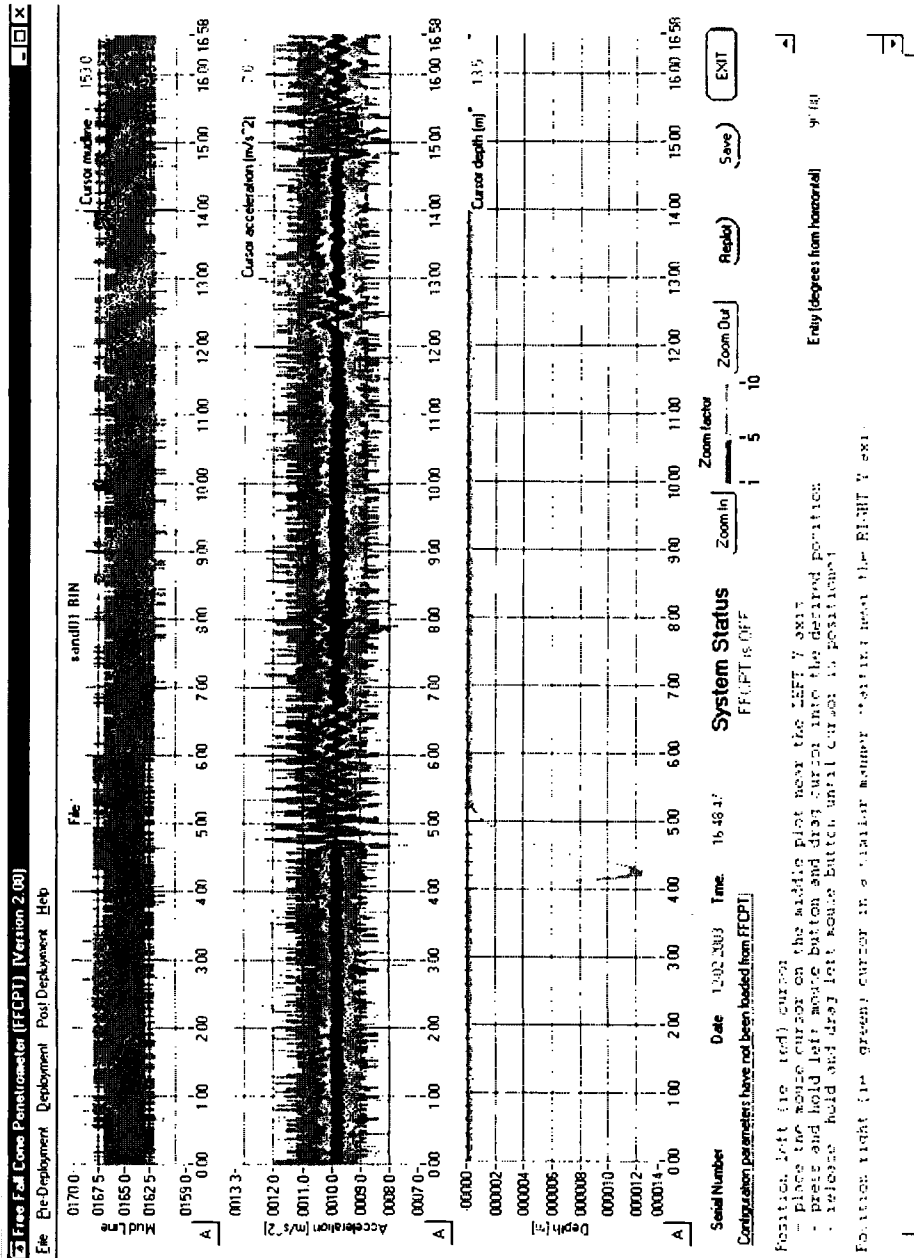


Figure 4-6: The raw data output from a FFCPT dropped into a drum of sand using company supplied software. Pressure supplied to tail pressure sensor using a air compressor for a trigger pressure of 10.0 m.

4.4 Field Deployment - Piscataqua River

The Piscataqua River is located between states of New Hampshire and Maine, where waters from several tributaries flow into Great Bay, a tidal estuarine system and eventually meet the Atlantic Ocean. Multiple drops using an experimental probe, the FFCPT, were made at 4 field stations, noted as Stations PISC, GB, FP and NP (see Figure 4-7).

A summary of the drops at the four stations is given in Table 4.2. The performance of the probe for drops from a vessel was evaluated using deployment at stations GB and PISC using the UNH Research Vessel, R/V Gulf Challenger. Fig. 4-10 shows a photograph of FFCPT being deployed from the R/V Gulf Challenger at Station GB. Stations NP and FP were located in shallower waters (see Figs. 4-8 and 4-9) close to boating piers. Each of the piers was equipped with a crane to drop and retrieve the probe. Fig. 4-11 shows a photograph of FFCPT being deployed at Station FP. The data from these two stations were primarily used to validate the sediment classification and shear strength models that are discussed in the next chapter.

Table 4.2: Summary of field deployment.

Location	Station Code	Sediment Type	Remarks
Piscataqua River	PISC	Sandy-Silt	No. of drops =7
Little Bay	GB	Sand	No. of drops =7
Piscataqua River	NP	Sand	No. of drops =5
Piscataqua River	FP	Fine Silt	No. of drops =5

4.5 Bering Sea

Deployment of a AFSC FFCPT in the Bering Sea, was done by the Alaska Fisheries Science Center (AFSC) in collaboration with the Center for Coastal and Ocean Map-



Figure 4-7: Satellite image showing the Great Bay estuary and the FFCPT deployment stations (source:Google Earth).



Figure 4-8: Satellite image showing the location of the Station NP (source: Google Earth).

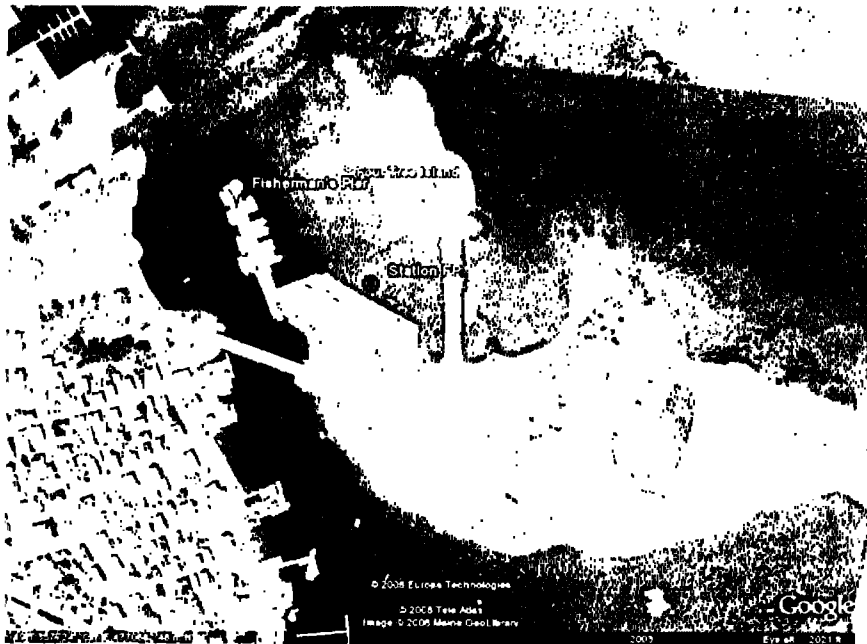


Figure 4-9: Satellite image showing the location of the Staion FP (source: Google Earth).



Figure 4-10: FFCPT deployment from R/V Gulf Challenger in the Piscataqua River (station GB) (photo provided by Prof. Ken Baldwin).



Figure 4-11: FFCPT deployment in the Piscataqua River off the Fisherman's Pier in Portsmouth, NH.

ping (CCOM), UNH. The survey was conducted as part of an experimental usage of free fall probes in the Essential Fish Habitat (EFH) study of federally managed fish species. EFH refers to "those waters and substrate necessary to fish for spawning, breeding, feeding or growth to maturity (Sustainable Fisheries Act , 1996). Determining the physical character of surficial sediments furthers the understanding of distribution and abundance of the ground fish species (McConnaughey et al., 2006).

The survey area consisted of six tracklines 140 nautical miles in length that traverse the southeast Bering Sea shelf over a depth range of 20 - 160 meters (see Fig. 4-12). The deployment of the AFSC FFCPT was done at 30 stations on the tracklines alongside of other surveys including a sediment sampling device called Seabed Observation and Sampling System (SEABOSS) (Blackwood et al., 2000). AFSC procured a Moving Vessel Profiler(MVP) along with the probe from Brooke Ocean Inc. The MVP has the capability to drop and retrieve the probe while the vessel is underway. Sediment samples using the SEABOSS sampler were collected at 26 of the 30 stations (Hill, 2006) are used to formulate the sediment classification system described in the next chapter.

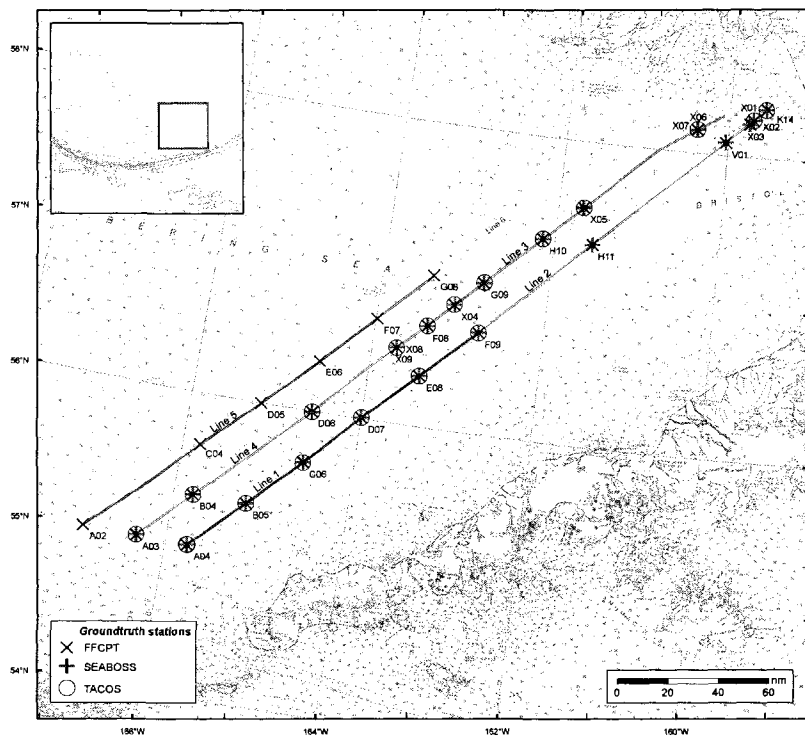


Figure 4-12: Map showing the location of survey area in the Bering Sea (Mc-Connaughey et al., 2006).

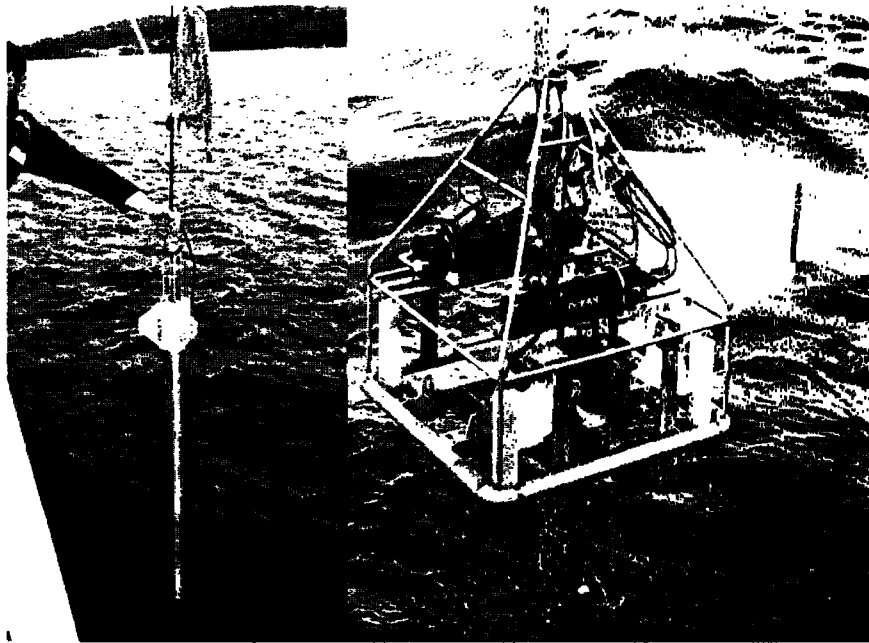


Figure 4-13: The FFCPT and SEABOSS grab sampler being deployed off the Vessel NOAA *Fairweather* in the Bering Sea (McConnaughey et al., 2006).

Table 4.3: Summary of FFCPT field deployment (from McConnaughey et al. (2006)).

Location	Station Code	Sediment Type	Remarks (if any)
Bering Sea	A04	Very coarse silt	No. of drops =6
Bering Sea	B05	Very coarse silt	No. of drops =6
Bering Sea	C06	Very fine sand	No. of drops =6
Bering Sea	D07	Very coarse silt	No. of drops =7
Bering Sea	E08	Very coarse sand	No. of drops =6
Bering Sea	F09	Very fine sand	No. of drops =7
Bering Sea	H11	Fine sand	No. of drops =6
Bering Sea	K14	Fine sand	No. of drops =6
Bering Sea	V01	Fine sand	No. of drops =6
Bering Sea	X01	Medium sand	No. of drops =6

Continued on next page

Table 4.3 – continued from previous page

Location	Station Code	Sediment Type	Remarks (if any)
Bering Sea	X02	Fine sand	No. of drops =6
Bering Sea	X03	Medium sand	No. of drops =5
Bering Sea	F08	Very fine sand	No. of drops =6
Bering Sea	G09	Fine sand	No. of drops =6
Bering Sea	H10	Fine sand	No. of drops =6
Bering Sea	X04	Very fine sand	No. of drops =6
Bering Sea	X05	Fine sand	No. of drops =6
Bering Sea	X06	Medium sand	No. of drops =3
Bering Sea	X07	Fine sand	No. of drops =2
Bering Sea	A03	Coarse Silt	No. of drops =6
Bering Sea	B04	Coarse Silt	No. of drops =6
Bering Sea	D06	Very coarse Silt	No. of drops =7
Bering Sea	F08	Very fine sand	No. of drops =6
Bering Sea	X08	Very fine sand	No. of drops =4
Bering Sea	X09	Very coarse silt	No. of drops =4
Bering Sea	F07	Very coarse silt	No. of drops =7
Bering Sea	F07	Very coarse silt	No. of drops =7
Bering Sea	A02	Unknown	No. of drops =1
Bering Sea	D05	Very coarse silt	No. of drops =6
Bering Sea	C04	Unknown	No. of drops =4
Bering Sea	E06	Unknown	No. of drops =6
Bering Sea	G08	Unknown	No. of drops =6

4.6 Shear Strength Determination Using a Field Vane Shear

A field deployment program was implemented to validate the shear strength model formulated in Chapter three. A field vane shear borer (FVS), on loan from the Massachusetts Institute of Technology (MIT) was used for this purpose. The FVS was deployed at the station FP, where a thick layer of marine silt was detected during the deployment of the FFCPT.

Field vane shear tests are commonly used to determine the *in situ* shear strength of soft fine-grained sediment. The ASTM Standard D2573 (ASTM, 2000) defines a vane shear test as "an in-place shear test in which a rod with thin radial vanes at the end is forced into soil and the resistance to rotation is determined". The torque measured from the rotation can then be used to infer the undrained shear strength in saturated fine-grained soils.

4.7 The Field Vane Shear Borer Equipment

The H-10 Field Vane Shear(FVS) Borer manufactured by Geonor Inc., Norway consists of three parts. The lower part, a vane and a protection shoe with a casing designed to be driven into soil. The upper part consisting of instrumentation to measure torque, and the middle part, extension rods and pipes that can be extended to 30 meters in length to connect the lower and upper parts. The vane, made of four blades, is rotated at a constant rate of strain by the crank handle and the maximum torque is measured which is then correlated with the undrained shear strength of the sediment. Figure 4-14 shows a photograph of various components of the FVS equipment.

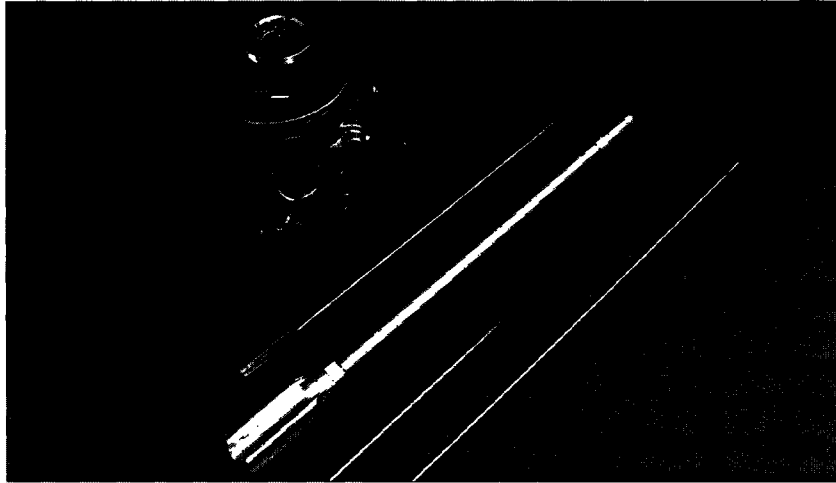


Figure 4-14: Figure showing various components of Field Vane Shearer (FVS) Borer (source: Geonor Inc.)

4.8 Interpretation of the Data

The equation for peak shear strength is given by the following (ASTM, 2000):

$$S_{u\ peak} = \frac{6T_{\max}}{7\pi D^3} \quad (4.1)$$

where $S_{u\ peak}$ is the undrained shear strength, T_{\max} is the recorded maximum torque and D the diameter of the vane (in meters). The values of S_u and T_{\max} are input in consistent units. The vane is then rotated for 10 complete revolutions and the remolded value of shear strength is calculated. Sensitivity provides information about the stress history of the sediments, it can be calculated using the following equation:

$$S_t = \frac{S_{u\ peak}}{S_{u\ remolded}} \quad (4.2)$$

where S_t is the sensitivity of the soft sediment and $S_{u\ remolded}$ is the remolded strength.

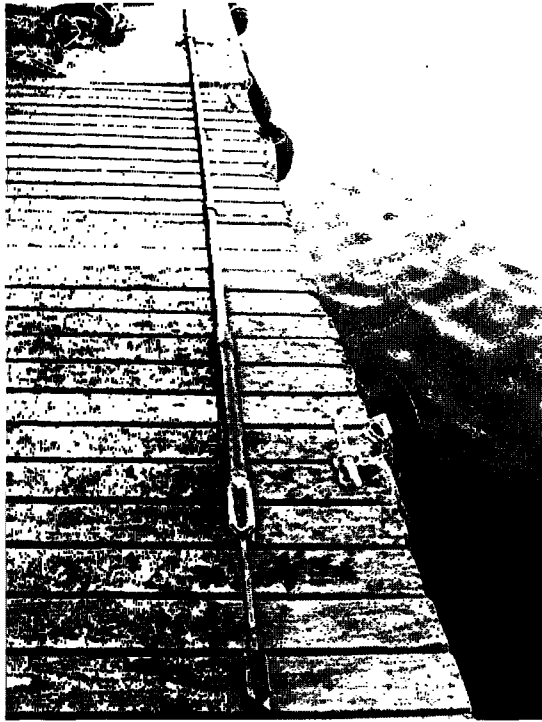


Figure 4-15: Photograph showing a fully assembled FVS Borer at the deployment location.

4.9 FVS Deployment

The FVS Borer was deployed at the Station FP (refer Fig. 4-9) in soft silty sediment. The pier provided the "firm ground" for the deployment.

Fig. 4-15 shows a fully assembled FVS after one test. Two more tests were performed at the location. The data to calculate $S_{u\text{peak}}$ was collected. The measurements at the depths tested did not allow the determination of $S_{u\text{remolded}}$ and by extension S_t . This was due to inadequate borehole depth created originally during the insertion of the casing, which collapsed soon after the completion of peak strength measurements.

CHAPTER 5

DATA ANALYSIS AND RESULTS

5.1 Introduction

Experimental data obtained from the field deployment of two cone tipped free fall penetrometers tested in sediment types ranging from silt to medium sand was analyzed using the analytical framework developed in Chapter 3. A sediment classification system based the firmness factor and embedment depth is proposed. Undrained shear strength profiles from drops in fine-grained sediments are determined using the formulated analytical model. The strain-rate dependent model is validated using data from a field vane shear measurements.

5.2 Data Processing

5.2.1 Initial Data Processing

Data obtained from each drop of the probe is automatically recorded and stored in a memory unit residing in the probe. This data was retrieved periodically so as to keep sufficient memory free. One of the first tasks in processing a free fall penetrometer's acceleration data is to solve the equation of motion to determine the velocity and position of the probe during its free fall motion through the water, impact and subsequent arrest in the seafloor. Initial data processing mainly dealt with the task of producing data relevant for further analysis. The analytical model

formulated in chapter two was implemented using MATLAB[®], a numerical computing environment and programming language (MathWorks Inc., 2008). Figure 5-1 shows a flowchart of program PREP developed for initial data processing. The main tasks of this programs include the following:

1. Conversion of the measured data from raw voltages, stored in binary format files to actual physical measurements of acceleration and pressure in a text format for easy manipulation.
2. The application of the forces acting on the free fall probe and subsequent solution of the equation of motion to determine the velocity and position of the probe.
3. The determination of the point of impact manually by observing spikes in the accelerometer, tip pressure and optical backscatter signals.
4. The determination of the point of arrest of the probe and the parameters useful for the further analysis such as peak acceleration (a_{max}), impact velocity (v_i), total duration of penetration (t_t), rise time (t_r) and embedment depth (z). The point of arrest is determined using the zero-crossings of velocity-time signal. This is done to exclude the portion of the signal representing the rebound of the probe after initial impact.

Figure 5-2 shows a plot of sample raw data from the OBS (represented as mud-line), accelerometers and pressure sensors. The plots shown are for the complete event of penetration i.e., free fall, impact and arrest. Figure 5-3 shows a plots of acceleration, velocity and position of probe obtained from initial data processing.

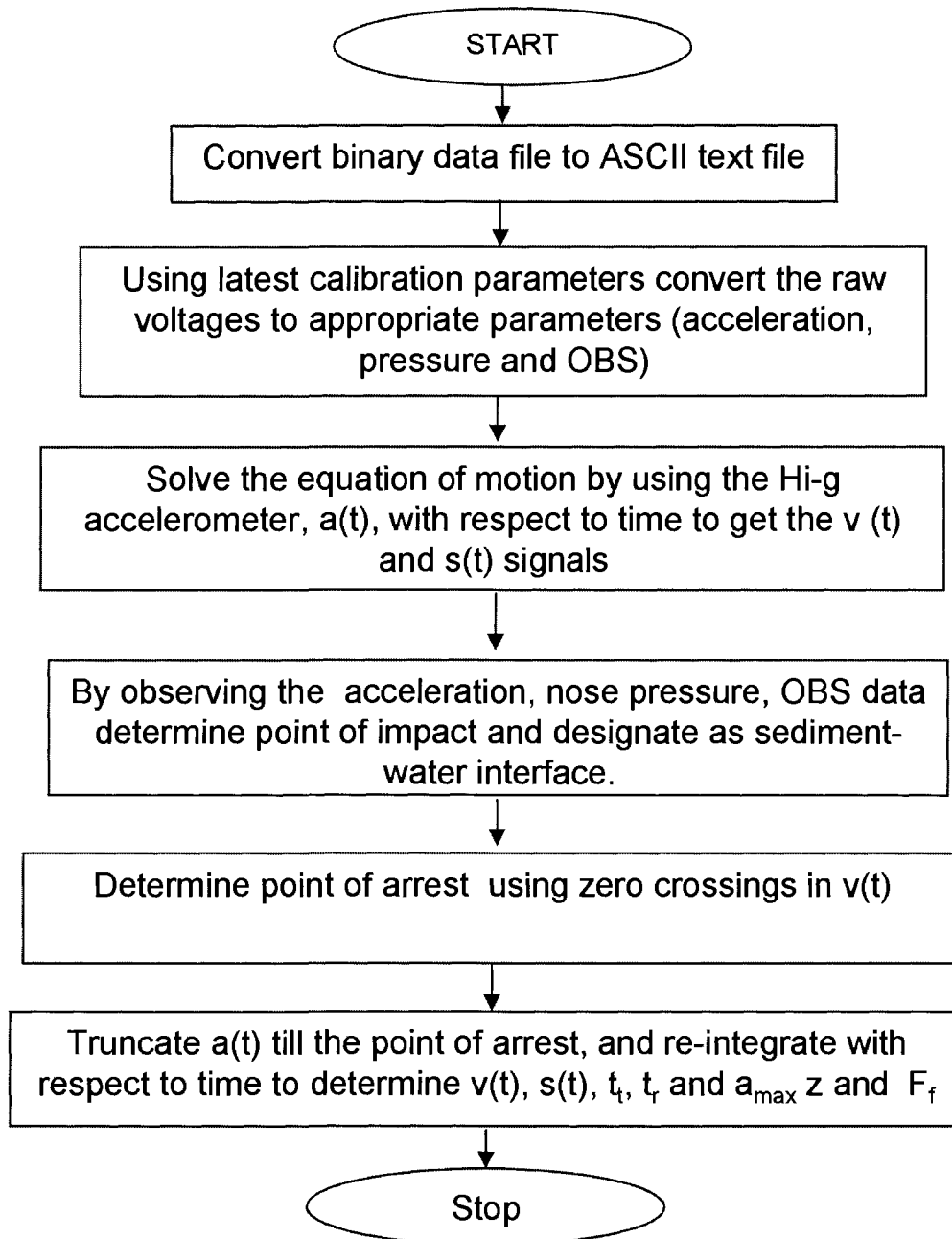


Figure 5-1: Flowchart describing the program PREP.

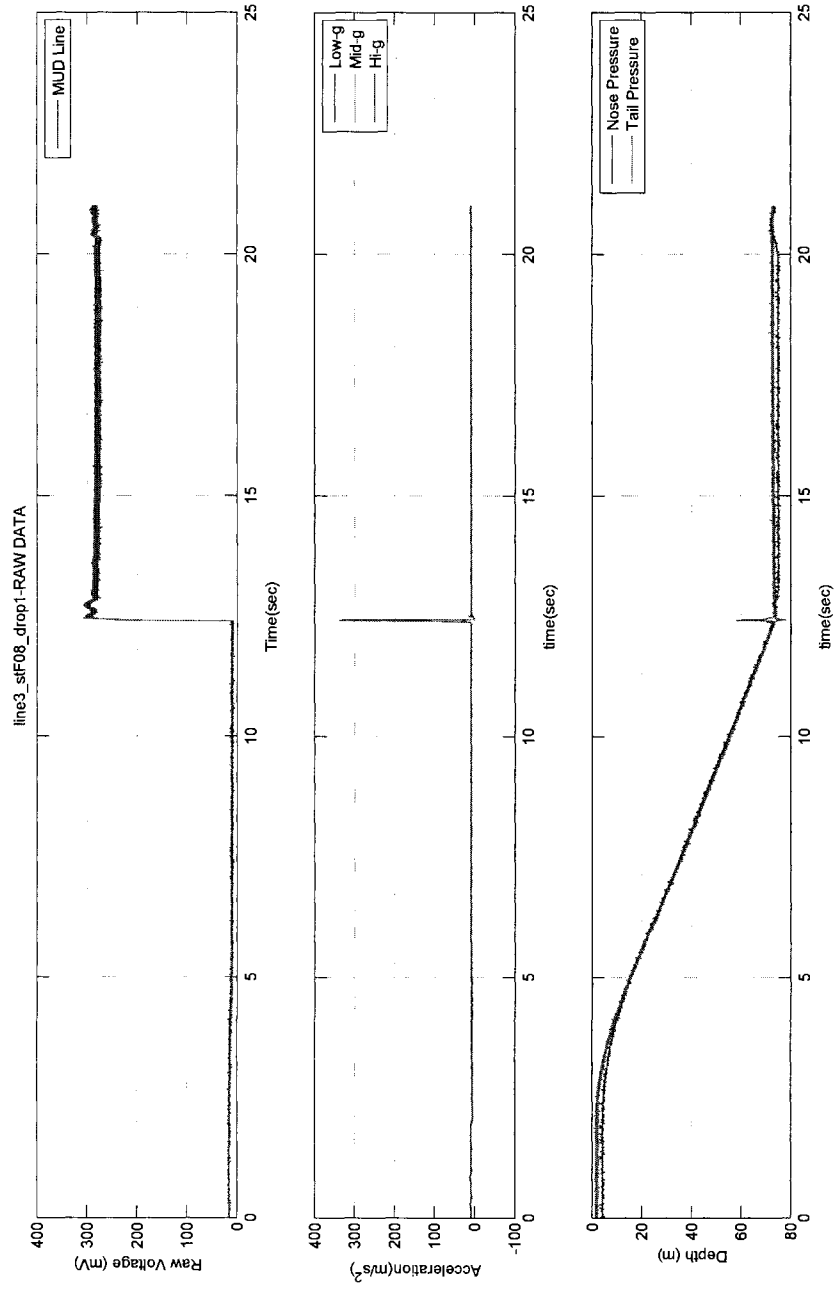


Figure 5-2: Plot of raw data from the OBS sensor (above), accelerometers (middle) and tail and tip pressure sensors (below).

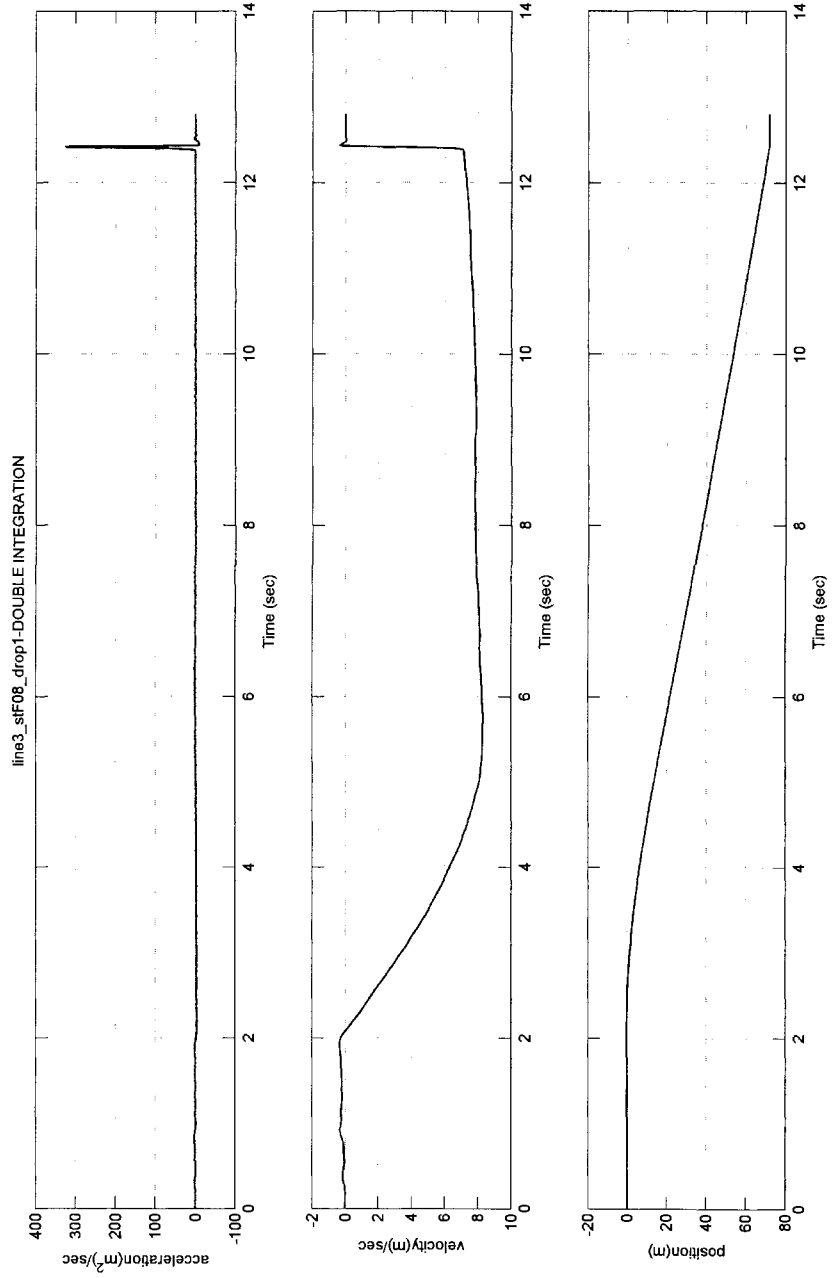


Figure 5-3: Plot showing output from program PREP, the acceleration (top), velocity (middle) and position (bottom) of the probe.

5.2.2 Analysis Tool

Parameters obtained by initial data processing are used for further analysis. This is accomplished by the development of FFCPT-TOOL an analysis tool in easy to use modular form. Figure 5-4 shows the organization of FFCPT-TOOL with various modules.

Data obtained from initial data processing is used to identify the sediment type based on the sediment classification model described in the next section. Further processing for sediment identified as predominantly as fine-grained is conducted to determine undrained shear strength (S_u) profiles. The CCE model formulated to solve the radial diffusion equation is used for trial values of coefficient of consolidation (C_h), permeability (k) and rigidity index (I_r). This is used to determine the contribution of normal stress induced and shear stress induced pore pressure. Relevant data is stored for further use such as for development of bottom type and other maps that can be integrated with test data from other geotechnical, geophysical or geological surveys of the seafloor.

5.3 Results

5.3.1 Sediment Classification Model

The firmness factor (F_f), introduced in Chapter 3, when plotted against the normalized embedment depth (z/D) showed a high degree of correlation to the target media in which the impact test was conducted. This approach was extended to distinguish unconsolidate sediment in the shallow depths of the seafloor encountered by a free fall probe. F_f also showed a variation with probe mass, shape and impact velocity. These factors can be constrained to minimize or eliminate influencing the development of a sediment classification system by using a probe with constant

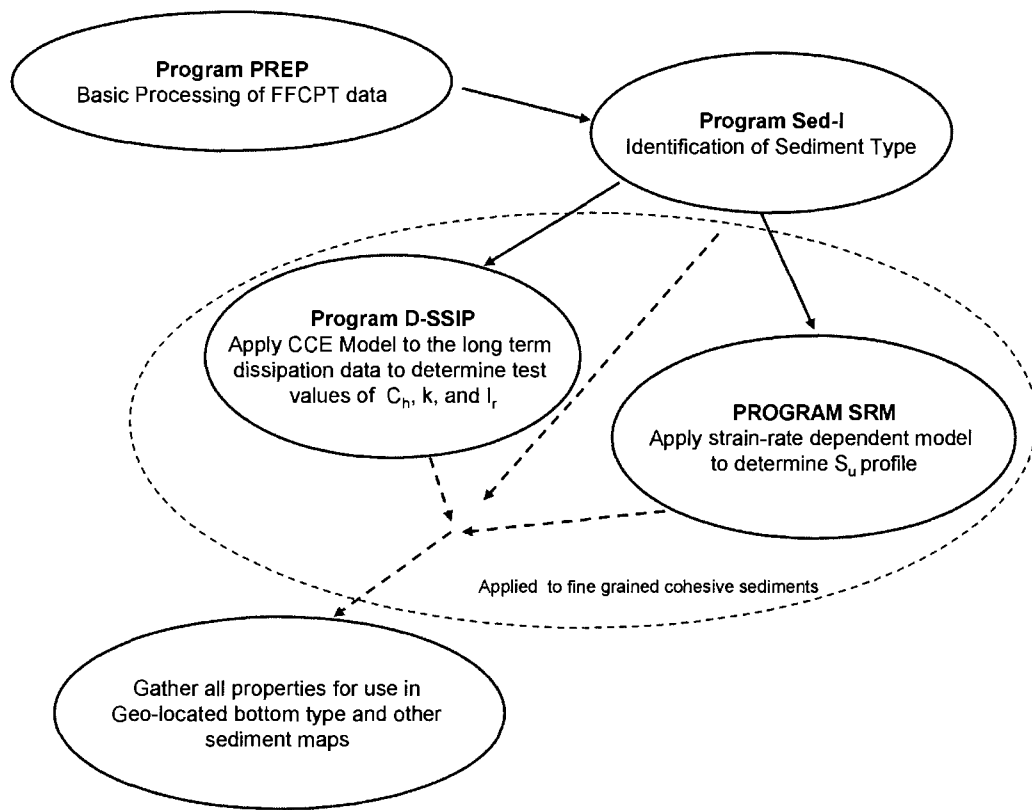


Figure 5-4: An organization chart of the processing procedure developed to implement the formulated analytical model.

geometry and mass and restricting the impact velocity to a narrow range.

Sediment grain size data collected by the SEABOSS sampling system during the Bering Sea deployment were used as part of this study. The grain size data were analyzed and reported by Hill (2006). Sediment type at each station was determined by evaluating the mean grain size parameter (M_z) and using the classification terminology given in Table 3.1 (in Chapter Three). Relevant data from these deployments is summarized in Appendix A. The grain size distribution curves derived from grain size analysis results are shown for each of the 26 stations in Figure 5-7.

The firmness scale described in Chapter 3 was extended to include data from this study. Figure 5-5 shows the plot of $a_{max}/(gv_i)$ against t_t . This plot from multiple impact tests confirms the general relationship between the parameters for different impact tests in target media ranging from concrete to soft silts in the seafloor. This study also justifies the extension of firmness factor's application to the present study.

The deployment of the FFCPT in the Bering Sea was conducted in water depths ranging from 20m to 110m. The impact velocities (v_i) ranged from 5.9 to 9.16 m/s. This wide range was observed due in part to the presence of excessive cable drag attributed to a malfunctioning winch used to drop and retrieve the probe. This effect can be noticed in a plot of impact velocity plotted against water depth. The plot is given in Figure 5-6. The probe, which has a terminal velocity of approximately 9 m/s, fails to attain the value in deeper waters. This suggests that there was cable drag associated with the deployment. This results also confirms observations made by personnel on board the vessel during deployment.

The variation in impact velocity does not affect proposing a sediment classification system specific to a type of probe. The sediment types in the Bering Sea deployment ranged from *Medium Sand* to *Coarse Silt* ($M_z = 1.29 - 5.38$). A sed-

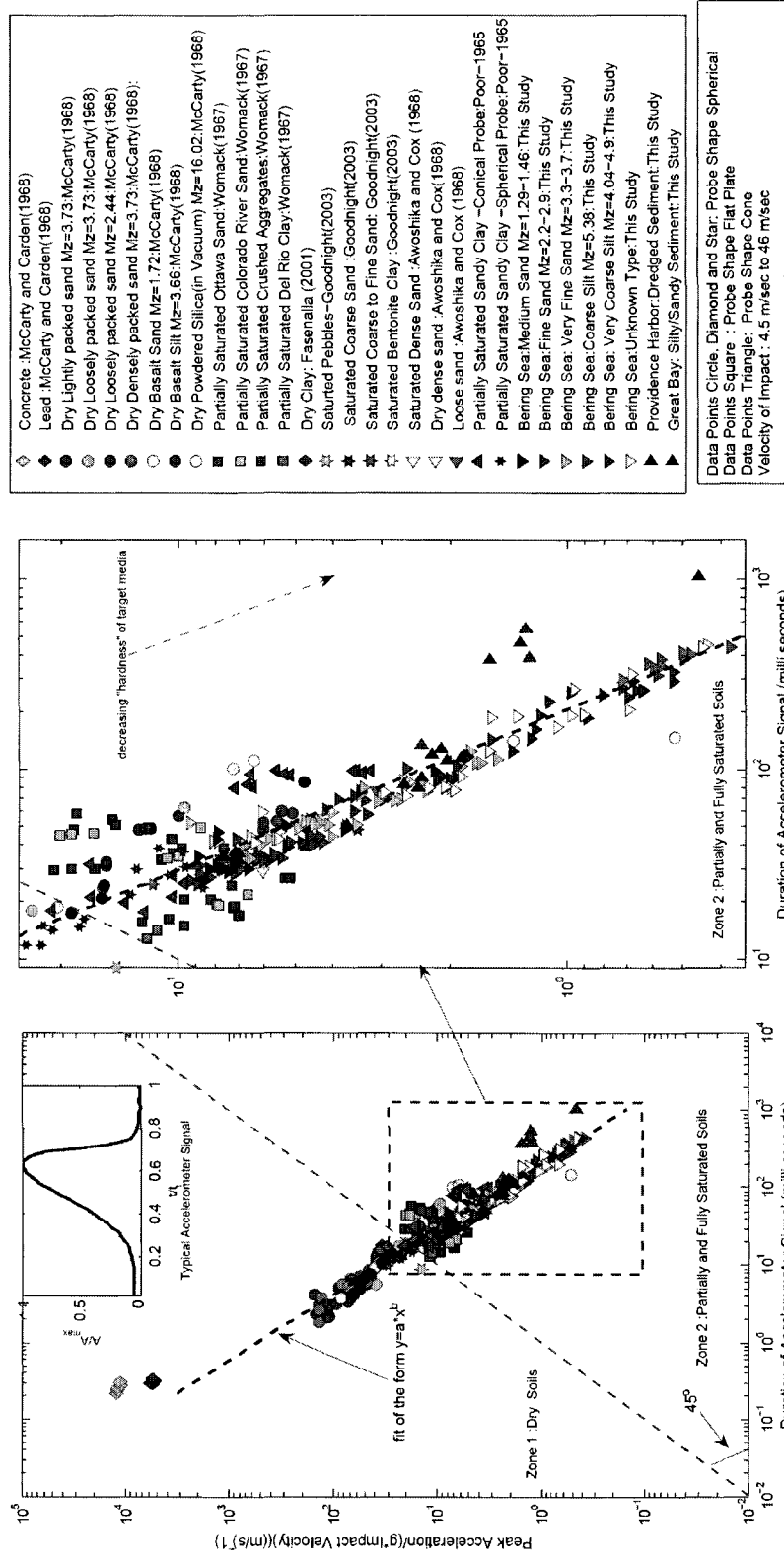


Figure 5-5: A logarithmic plot of peak acceleration (a_{max}) normalized with acceleration due to gravity g and impact velocity (v_i) plotted against total duration of the acceleration-time signal (t_t). The legend gives details of the various sources of the data.

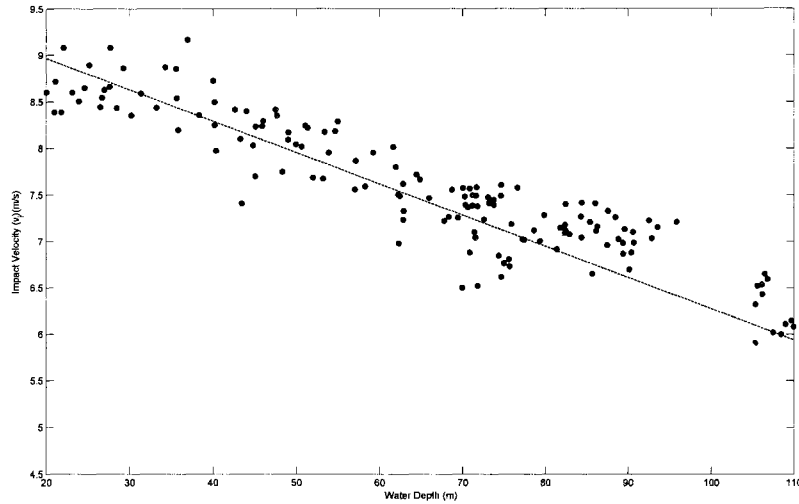


Figure 5-6: Plot of impact velocity against water depth for Bering Sea deployment. The plot shows the presence of cable drag resulting in lower impact velocities for increased water depth.

iment classification system is shown in Figure 5-8. This system is based on the data obtained from the AFSC FFCPT and is not strictly applicable to data from other probes. This is mainly due to the lack of a quantitative relationship between F_f and variables such as mass and probe shape. The system will be applied to data from UNH FFCPT since it is only slightly different in mass and size to the AFSC FFCPT. Dual categories of sediment types have been added to make it broad enough to take into account the influence of variables not included in the model.

5.3.2 Validation of Sediment Classification Model

The classification model is validated using data obtained from the UNH FFCPT deployment at station NP in the Piscataqua River. The bottom type determined from the classification model is compared with the sediment type identified by prior geotechnical studies.

A graphical method is used to determine the sediment type at station NP. Figure 5-9 shows the sediment classification model previously described with data from the

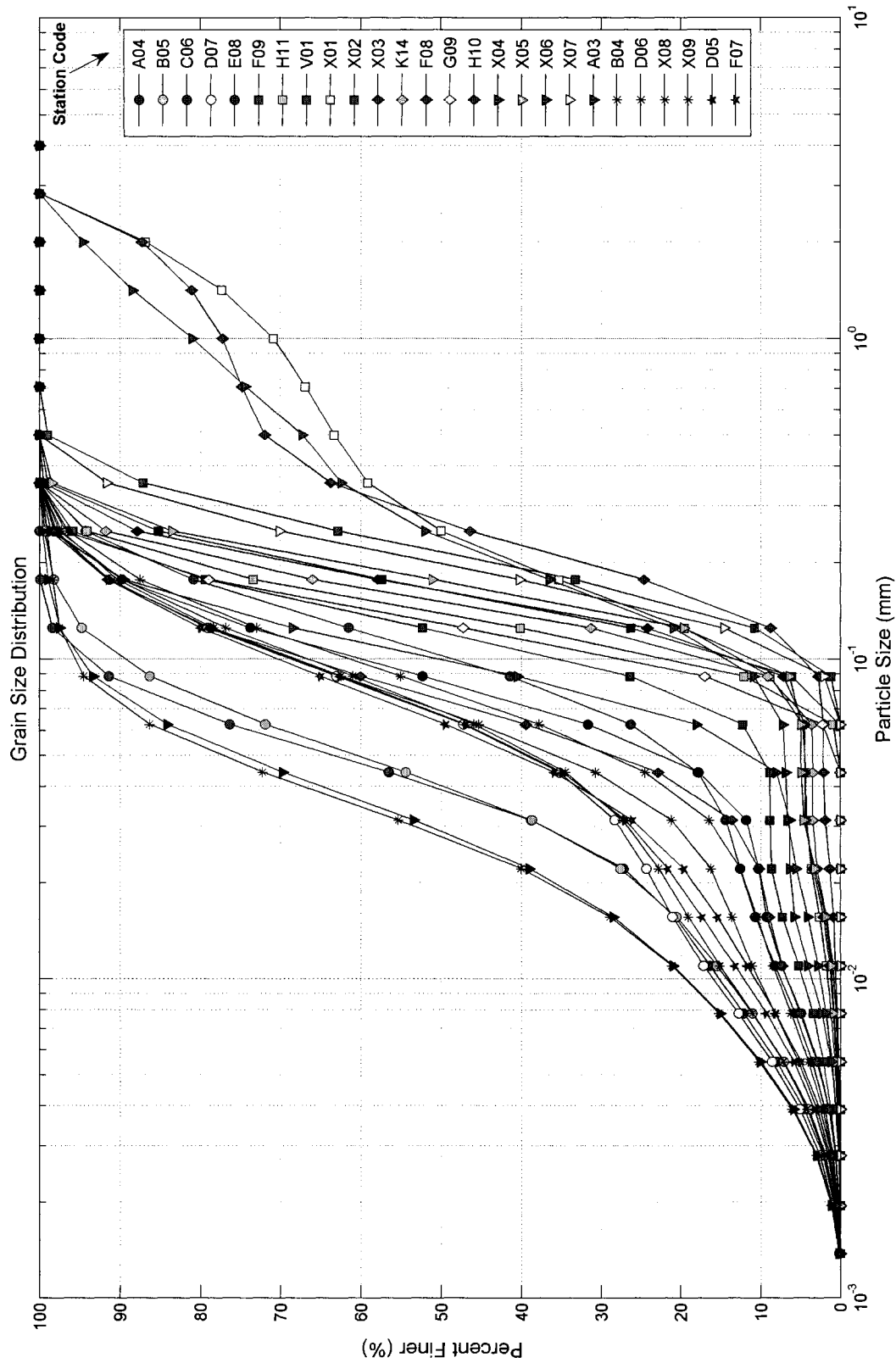


Figure 5-7: Plot showing the grain size distribution curves from samples collected at 26 stations in the Bering Sea. The y-axis shows the cumulative fraction of sediment that passed a particular size of sieve (x-axis).

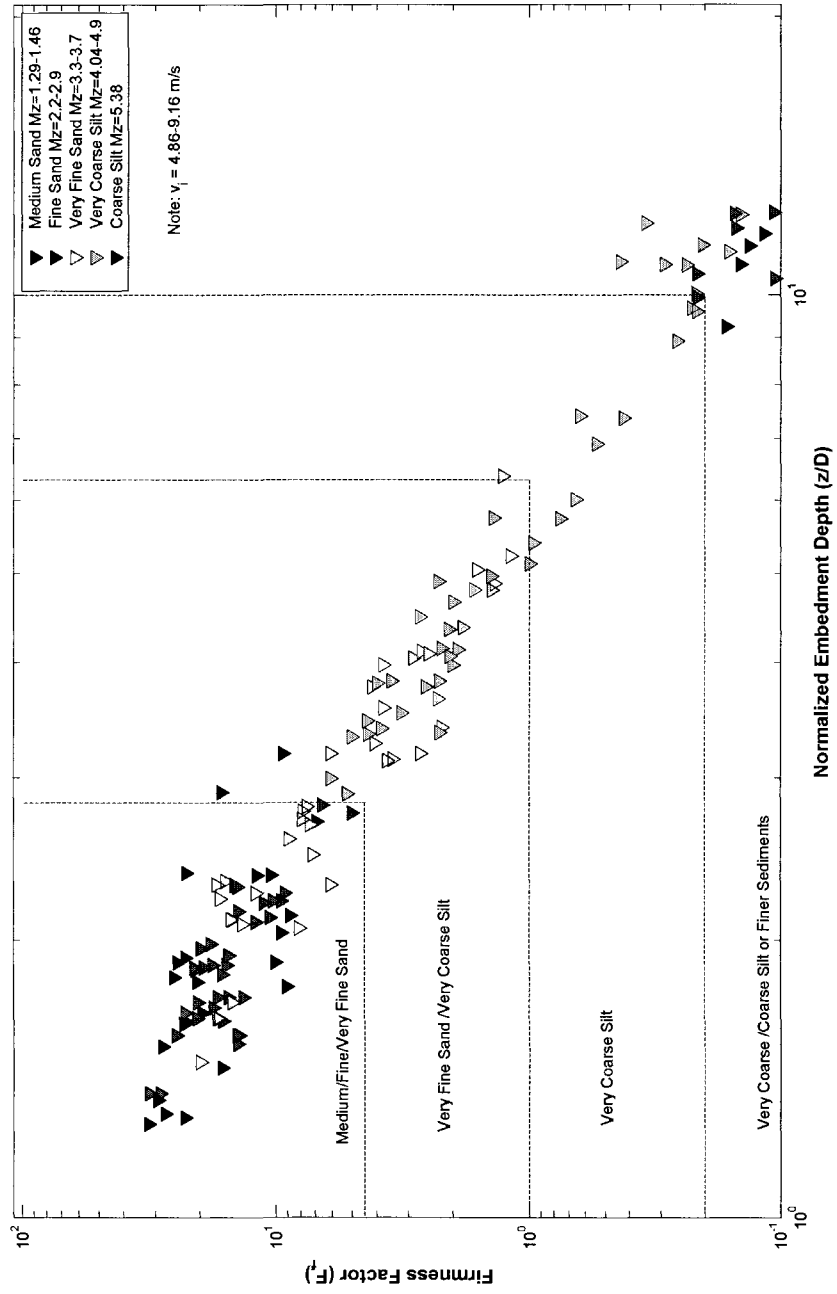


Figure 5-8: Plot showing the proposed sediment classification model based on data from Bering Sea deployment.

FFCPT drops at station NP overlaid. Four of the five drops at the station suggest that the sediment of type is "medium to very fine sand". Prior geotechnical studies conducted by UNH for the construction of the pier adjacent to the station provided grain size data to classify the sediments. Figure 5-10 shows grain size distribution curves obtained from data provided (Buzby and Karbe, 2005). The fifth data point shows a very high "firmness" and this can be attributed to the probe encountering seashells at the location. Boring logs conducted for pier construction at the site provided more information on the composition of the sediment. The log at the nearest location to the station NP identified fine to coarse sand in the sample and described the sample as the following: "Medium dense, black to fine coarse sand with little silt and trace gravel" (Moulton and Stuttdard, 2002). This suggest that the probe could have encountered either a local deposit of gravel , construction debris, or seashells to explain the anomalous fifth data point.

5.3.3 Bering Sea Sediment Map

A free fall penetrometer can be used for quick and inexpensive identification of surficial sediment. The Bering Sea FFCPT deployment data was analyzed to create a bottom type map using the proposed sediment classification system. Figure 5-11 shows the mean value of $F_f/(z/D)$ plotted as a contour map with an overlay of station locations in the Bering Sea. It must be emphasized that the map for a vast area was created with data points from a limited number of stations on the survey lines. The accuracy of the map can be increased by increasing the number of stations where the drops are performed. Probes such as XBP, which can be deployed while the vessel is underway, are especially suitable for the adaptation of such a sediment classification system. Such applications can lead to the further integration of free fall penetrometers into geophysical, geotechnical or geological studies of the deep sea.

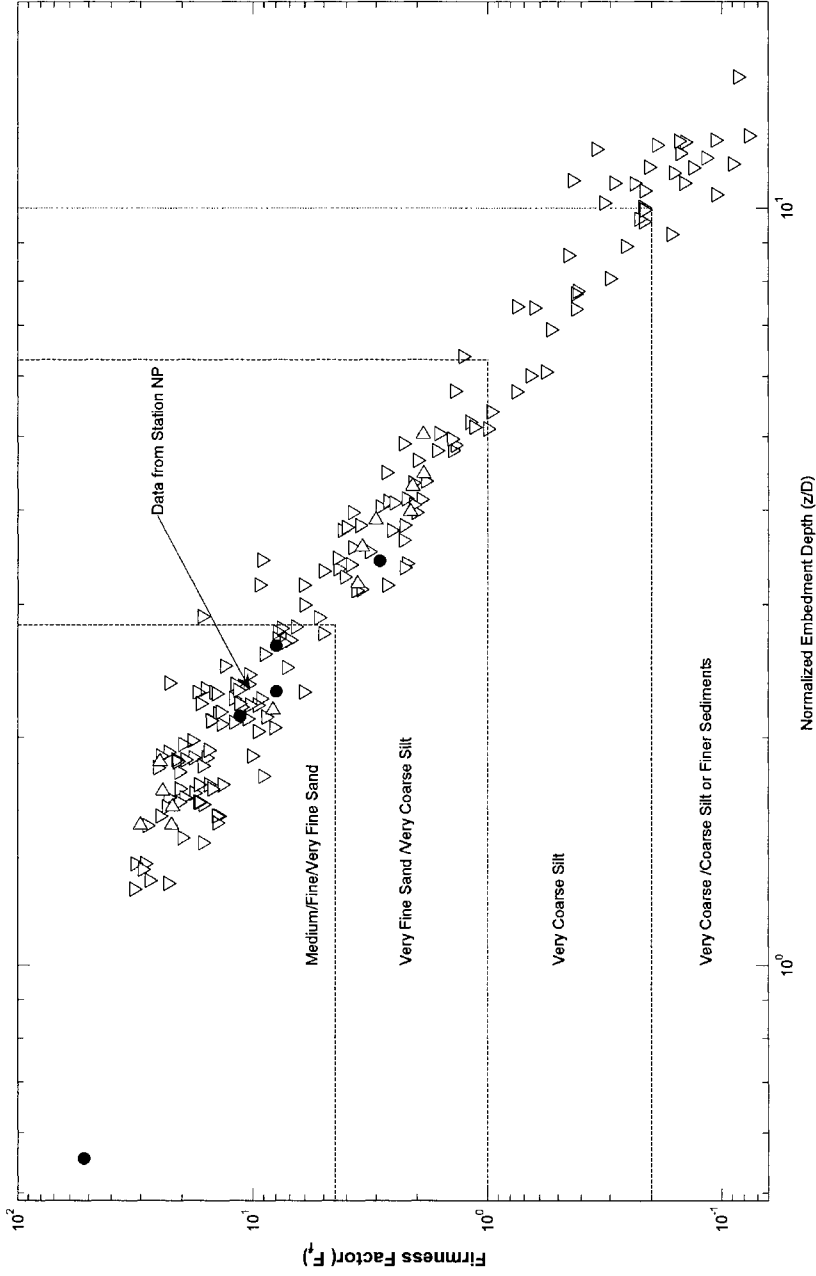


Figure 5-9: Bottom type prediction at Station NP. The data from the FFCPT drop at the station is denoted by circular markers.

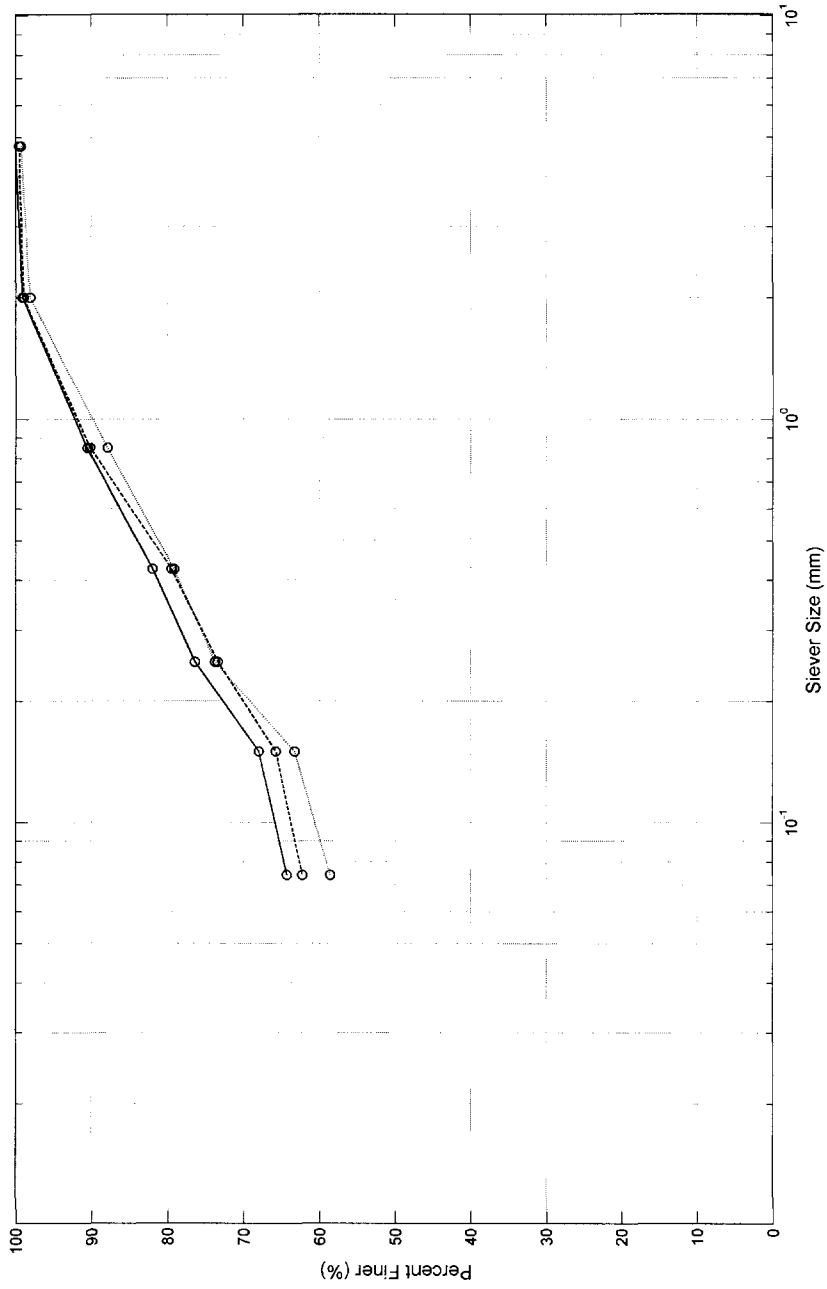


Figure 5-10: Grain size distribution curves of sediments at station NP (based on data from Buzby and Karbe (2005)). The mean $M_z = 3.50$, giving a classification as "very fine sand".

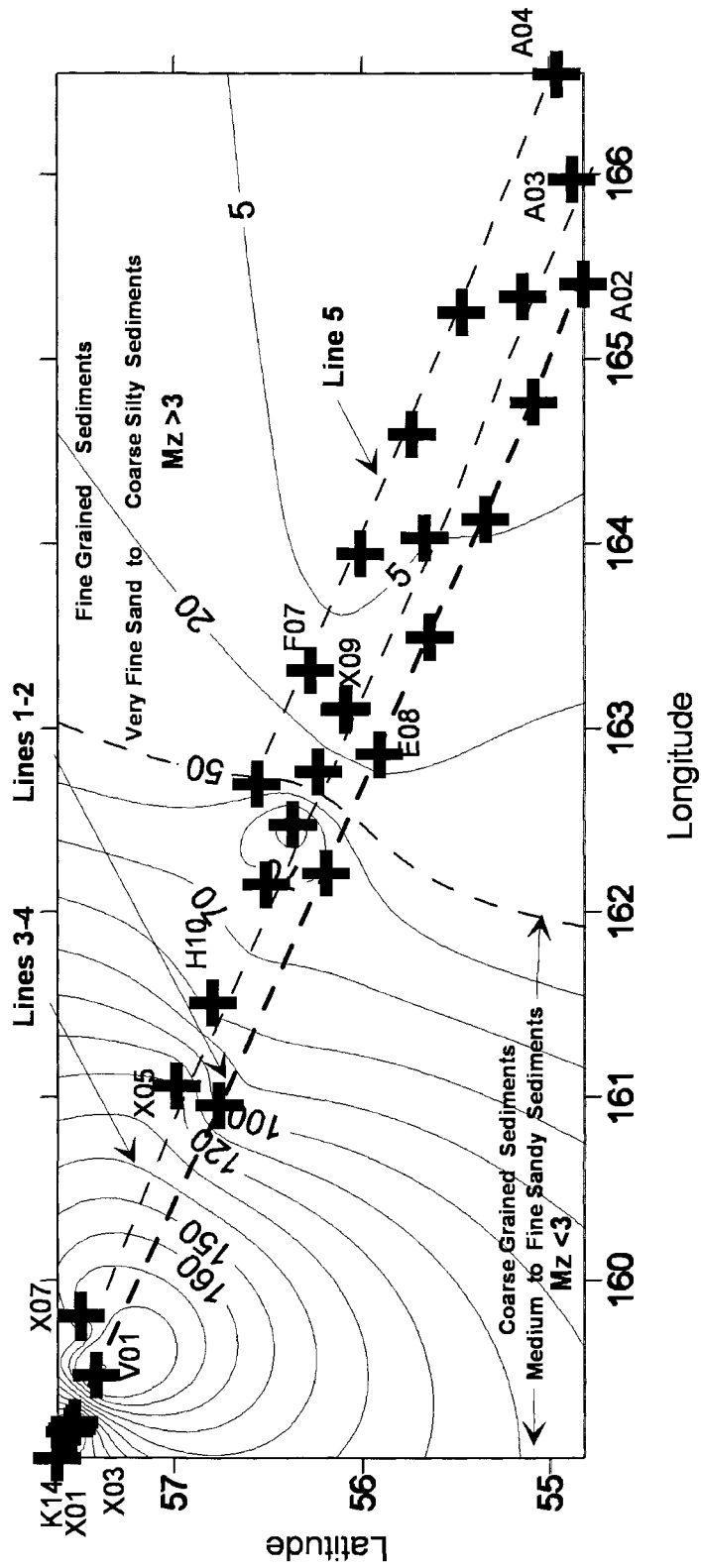


Figure 5-11: Mean $[F_f / (z/D)]$ plotted as a contour map with an overlay of station locations in the Bering Sea.

5.3.4 Undrained Shear Strength

Undrained shear strength is an important property of soft sediments useful in many studies including mine burial and undersea pipeline construction. Chapter 3 described a strain-rate dependent model to determine the undrained shear strength of soft fine-grained sediment from free fall penetrometer data. This model is applied to FFCPT deployment data from stations where the sediment was identified as soft silt and finer sediments. The validation of the model is accomplished using data from station NP by comparing shear strength profiles with vane shear data.

The penetration resistance (Q_d) of a probe at a depth (z) is related to the undrained shear strength of sediment (S_u) by the following equation:

$$Q_d = N_c S_u A + \sigma_{vo} A \quad (5.1)$$

where N_c is the empirical cone factor and σ_{vo} is the overburden pressure at the depth under consideration and A is the cross sectional area of the probe.

The variable penetration rate of the probe induces high strain rates which influence the determination of undrained shear strength. The model described previously introduced rate dependent bearing capacity factors that are used to calculate the shear strength of soft sediment penetrated by a free fall penetrometer.

$$N_{cv} = N_{co} [1 + \lambda_o \log_{10}(\frac{v}{D\dot{\epsilon}_o})] \quad (5.2)$$

where $\dot{\lambda}_0 = \ln(\lambda_0)/10$. N_{co} is the quasi-static cone factor that can be determined based on a formulation provided by Houlsby and Martin (2003). The formulated model was implemented in the model. Figure 5-12 shows the variation of velocity dependent cone factors with the normalized embedment depth for the UNH FFCPT.

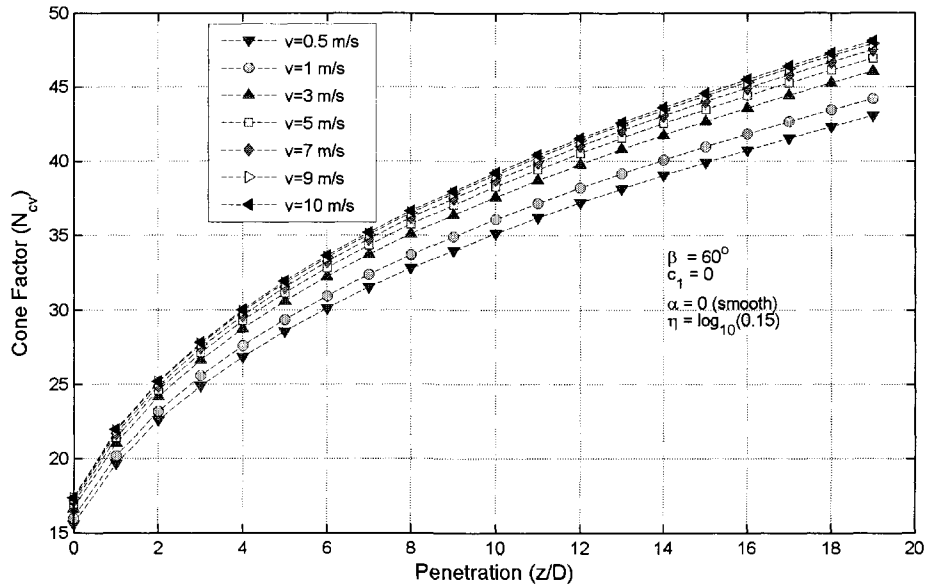


Figure 5-12: Variation of model cone factors with normalized embedment depth for AFSC FFCPT.

The model was used to analyze data of FFCPT drops from station FP. The sediment at the station was visually identified as marine silt with traces of seashells using a grab sample. The sediment classification system also confirmed the sediment to be *soft coarse silt or finer* (Figure 5-13). The strain rate dependent model was applied using program SRM. Figure 5-14 shows the shear strength profiles from five drops of the FFCPT. Values of $c_1 = 1.0$ and $\lambda = 0.15$ were used in the analysis. In the plot, data from some of the drops shows apparent high shear strength values at the mudline. This can be attributed to the presence of seashells in the sediment.

The shear strength profiles from the station FP are compared with vane shear data at the same station. Figure 5-15 shows a plot comparing the data from the two field studies. Figure 5-16 shows shear strength comparison neglecting the effect of strain rate. The shear strengths from a free fall penetrometer are over-predicted without taking strain rate effects into account. The study validates the analytical

model to determine the *in situ* undrained shear strength of soft silty and clayey sediments. A sample strength profile of data from station A04 in the Bering Sea is given in Figure 5-17.

5.3.5 Study of Pore Pressure

The FFCPT is equipped with two pressure sensors. One is located near the tip and the other at the end of the probe. The probe is capable of measuring pore pressure during the free fall and embedment stages in coarse-grained as well as fine-grained sediments.

In Chapter 3 a cylindrical cavity expansion (CCE) model was formulated to determine properties such as the coefficient of consolidation (C_h), permeability (k) and shear modulus (G) for soft fine-grained sediments such as clays and silts from long term pore pressure dissipation data. The model could not be applied to data from the FFCPT due to the lack of storage and design capabilities needed to measure long term dissipation. Nevertheless, the CCE model has been integrated into analysis model for future use.

Impact loading of saturated sandy sediments result in pore pressure changes. These changes vary depending on the penetration rate, type of sediment as well as the boundary conditions that control the drainage. There have been some experimental studies of post-impact pore pressure in saturated sediments directly measured from impact probes (for example Stoll et al. (2007) and Hansen and Gislason (2007)). The impulsive nature of the loading tends to dilate the sediment and the pore pressures drop from the geostatic level. The drop in the pore pressure tends to increase the resistance as measured by the probe. As this effect is dependent on the penetration rate it has been termed as "strain rate effect on saturated sands". Due to the high permeability, the drainage conditions in sands and other coarse-grained sediments range anywhere from undrained to fully drained depending on

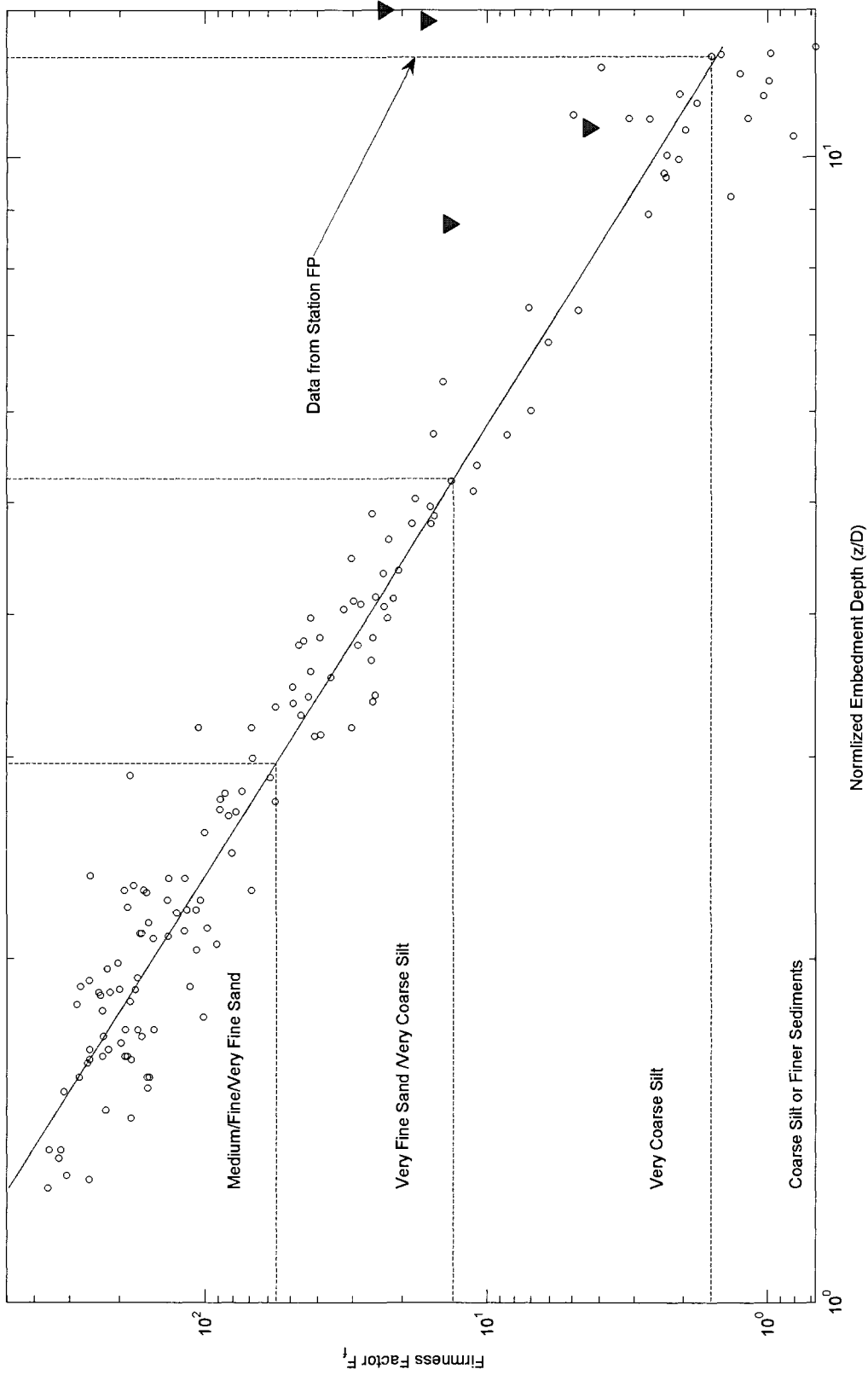


Figure 5-13: Sediment type at Station FP determined using the sediment classification model.

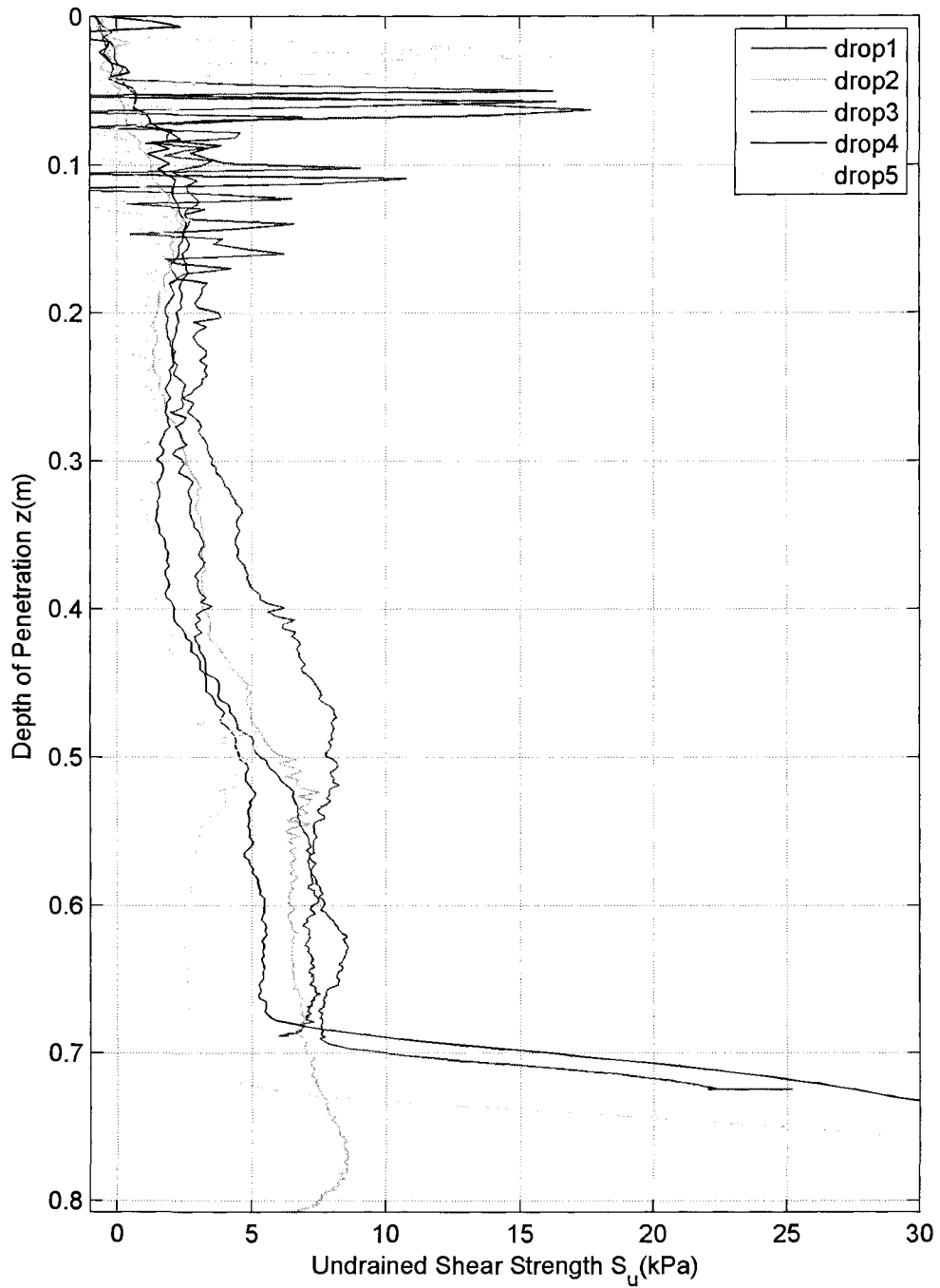


Figure 5-14: Variation of undrained shear strength with depth, as station FP with input values of $c_1 = 1.0$ and $\lambda = 0.25$

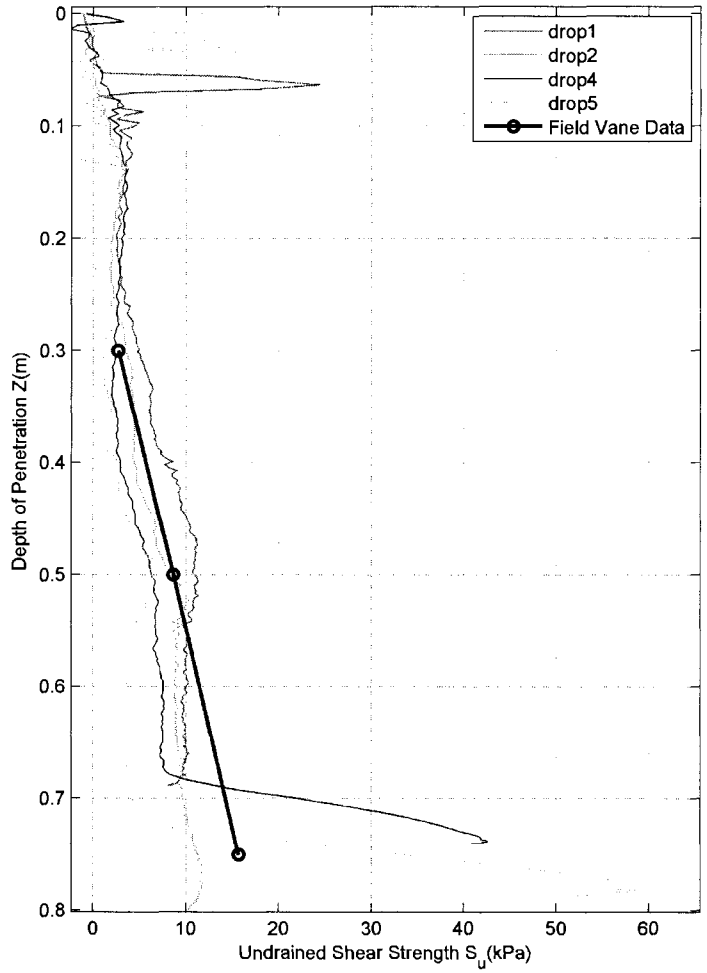


Figure 5-15: Comparison of FFCPT shear strength profiles with data from field vane shear studies at station FP. Values of $c_1 = 1.0$ and $\lambda = 0.15$ were used to determine FFCPT data.

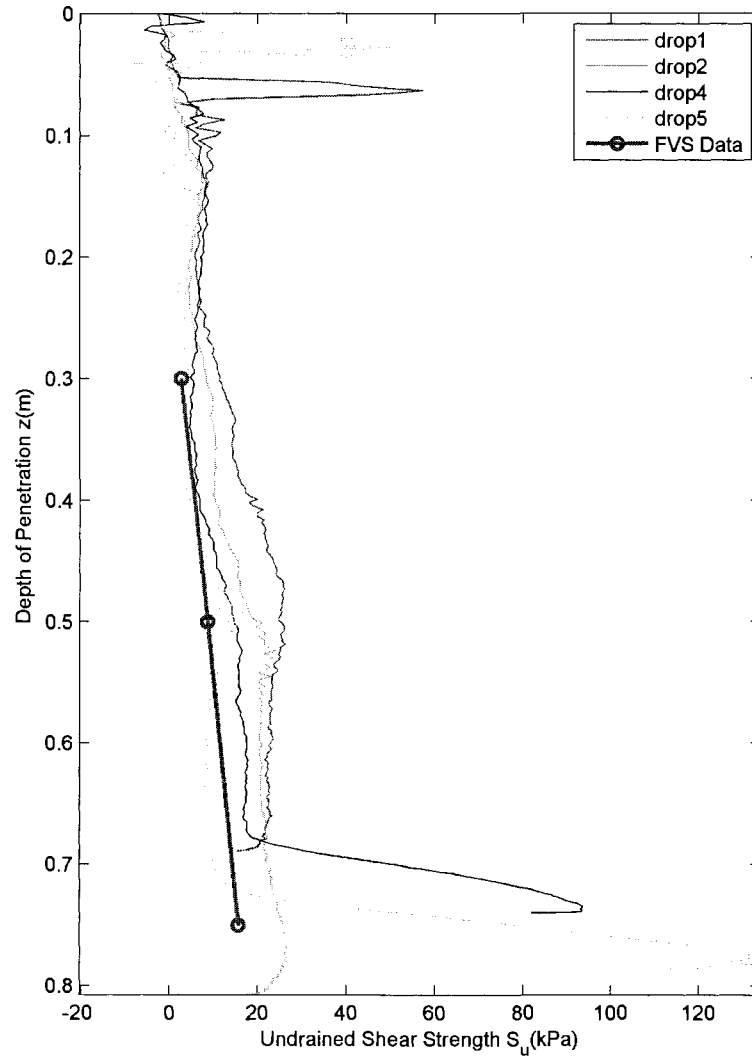


Figure 5-16: Comparison of FFCPT shear strength profiles with no influence of strain rate data. Values of $c_1 = 1.0$ and $\lambda = 0.0$ were used to determine FFCPT data.

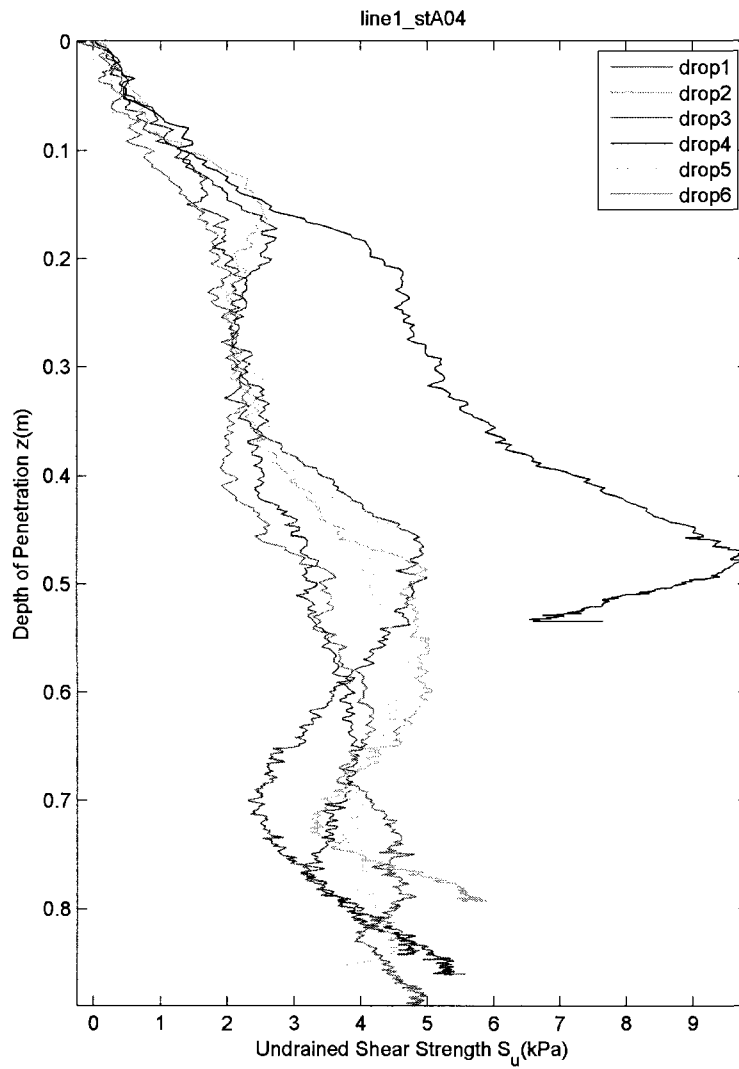


Figure 5-17: Sample shear strength profiles from Station A04 in the Bering Sea. Values of $c_1 = 1.0$ and $\lambda = 0.25$ were used for this analysis.

the penetration velocity and boundary conditions.

The quantitative study of pore pressures in sandy sediments is beyond the scope of this dissertation. But a qualitative study was conducted to observe dilatancy effects in the range of sediment types tested. Figure 5-18 shows the variation of maximum positive and negative pore pressures during the penetration event to the mean grain size for Bering Sea sediments. It is observed that there is a greater difference between the positive and negative pore pressure in sediment types ranging from fine sand to very coarse silt. These are the sediment types most conducive to exhibit dilatancy effects due to dynamic penetration by the FFCPT in the velocity range observed in testing. Furthermore, the variation of firmness factor and embedment depth to mean grain size is studied alongside of maximum positive and negative pore pressures. Figure 5-19 shows these plots which suggest that a distinguishing feature between *medium* and *very fine sand* is the lower observed dilatancy in *medium sand* at the observed penetration rates. It can be concluded from this study that a qualitative analysis of dynamic pore pressure can be integrated into a sediment classification system to distinguish sediments exhibiting dilatancy behavior from those that do not.

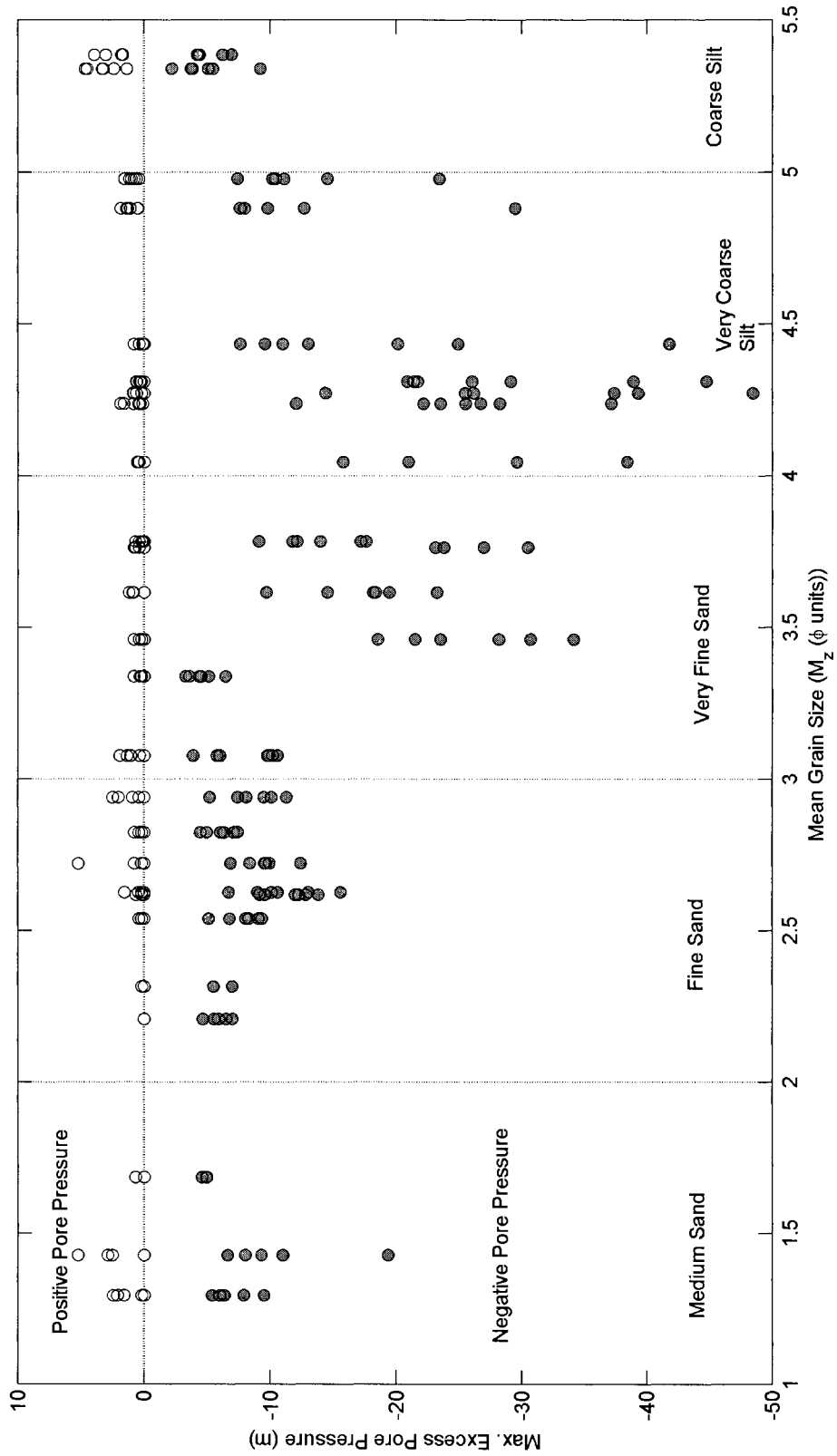


Figure 5-18: Variation of positive and negative pore pressure with mean grain size for Bering Sea sediments.

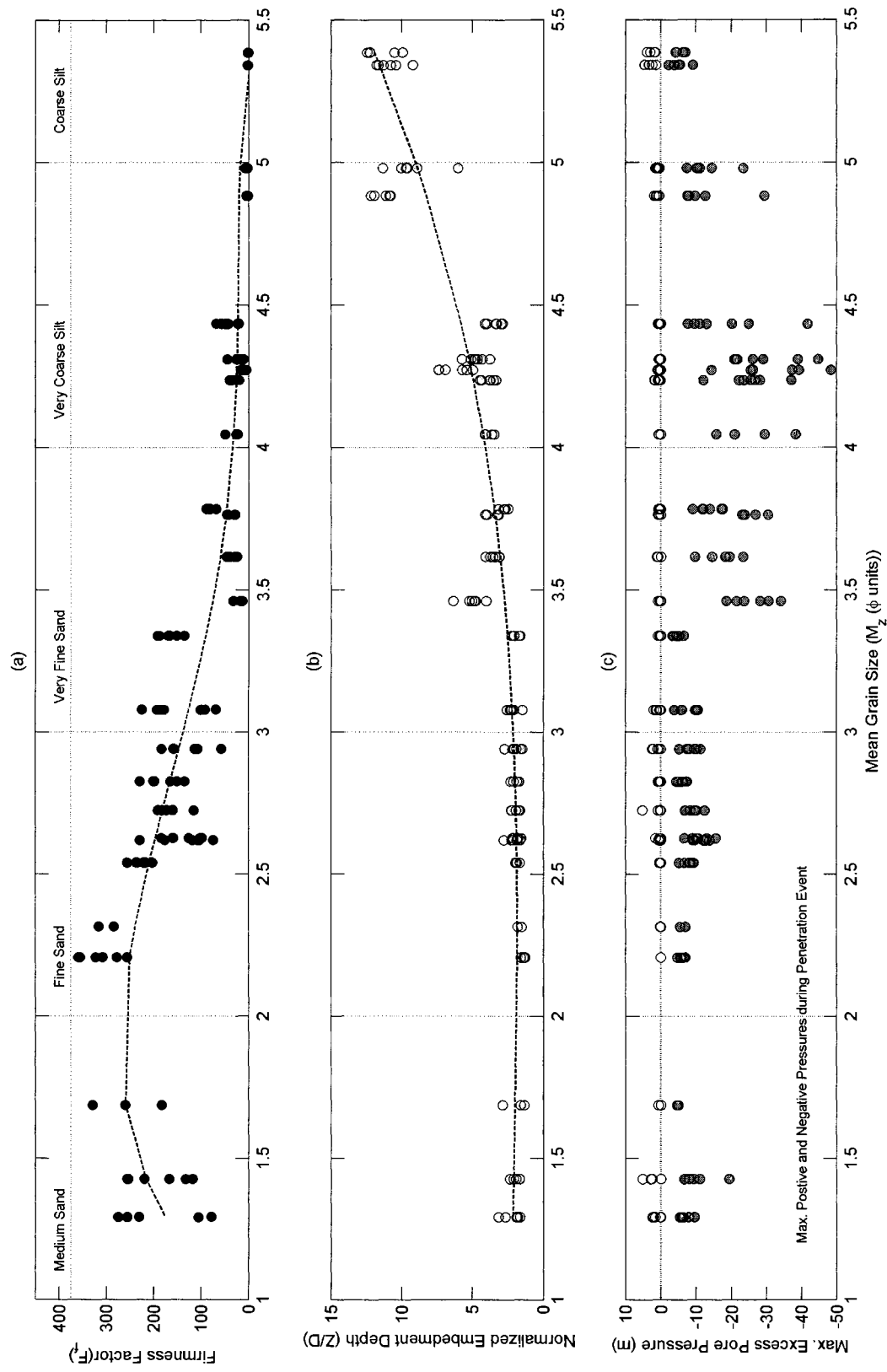


Figure 5-19: Variation of firmness factor (F_f), normalized embedment depth (z/D) and excess positive and negative pore pressure to mean grain size (M_z).

CHAPTER 6

CONCLUSIONS AND RECOMMENDATIONS

6.1 Conclusions

The work in this dissertation can be divided into two separate studies. Firstly, the formulation of a new analytical model for a free fall penetrometer and secondly, the application of this model to data from field deployment studies.

The research to understand the background of free fall penetrometers and the formulation of a new analytical model provide the following conclusions:

1. The acceleration signals of free fall penetrometer tests have valuable information about the nature of the shallow seafloor. Important variables for such studies include peak acceleration (a_{max}), impact velocity(v_i), total time of impact(t_t), mass(M) and normalized penetration depth (z/D).
2. The dynamic nature of penetration results in increased shear strength due to high strain rates. The drainage conditions during penetration may vary from fully drained and partially drained to undrained depending on the sediment type. Consequently, the direct application of empirical correlations for strength and soil classification determined from quasi-static CPT models are not proven or validated for use with data from free fall penetration.
3. A free fall penetrometer equipped with accelerometers and pressure sensors can be used to conduct dissipation tests in fine-grained sediments to determine properties such as coefficient of consolidation (C_h) and permeability (k).

Undrained shear strength data from the strain rate dependent strength model can be used to provide an estimate of the rigidity index (I_r) of soft sediments.

4. A cylindrical cavity expansion (CCE) with soil modeled as an elastic-plastic material is used to solve the diffusion equation for test values of coefficient of consolidation (C_h), permeability (k) and rigidity index (I_r). Normal-stress induced pore pressure forms only a small and negligible component of total pore pressure in normally consolidated and slightly overconsolidated soils. In stiff highly overconsolidated clays normal-stress induced pressure is a large component of total pore pressure.

The field deployment of a free fall penetrometer and subsequent data analysis using the proposed analytical model provide the following conclusions:

1. The acceleration-time signals from drops with a free fall penetrometer at the same station are repeatable within a range that is suitable for identifying sediments and determining strength profiles.
2. A sediment classification model can be established for a free fall probe with a constant tip geometry and mass for a narrow range of impact velocities.
3. Normalized embedment depths in coarse-grained non-plastic sediments are in the shallow to intermediate ranges ($0 < z/D < 20$). While, in soft fine-grained sediments it is greater than 20 ($z/D \geq 20$). Normalized penetration depth for *medium sand* is less than one ($z/D < 1$), suggesting that there is a physical zero-bound that limits the probes used in the study from distinguishing coarser sediments such as gravel from other coarse-grained sediment. Similarly, sediments finer than coarse silt would be indistinguishable from other soft fine-grained sediment. This conclusion though applicable to the probes used point towards the limitation of free fall probes in general.

4. The inertial drag forces (F_D) are small enough to be neglected while solving the equation of motion for the free fall probes. This confirms a similar conclusion made by True (1976).
5. The strain-rate dependent analytical model to determine undrained shear strengths of soft fine-grained sediments shows good comparison with the field vane shear strength profiles. Neglecting strain rate in analyzing free fall penetrometer shear strengths results in significant over-prediction of shear strength values as compared with field vane shear strength profiles.

6.2 Recommendations for Further Research

The following are the recommendations for further research :

1. The freely falling penetrometer is assumed to impact and penetrate the sediment vertically. This is a critical assumption in the formulation of the CCE dissipation model. Additional sensors and instrumentation are recommended to determine the full nature of impact. This would assist in the further development of the CCE model and any corrections that would need to be applied.
2. The shapes of acceleration-time signals show variations due to the tip geometry of the probe. A study to quantify the effect of variable mass, diameter and impact velocity for specific tip geometries in saturated sediments would provide a more accurate sediment classification model that could lead to the design variable mass and variable diameter probes, thereby expanding the coverage of sediment types that can be identified. Such studies can also find application in mine burial studies as scaled models in the laboratory and field can be used to predict penetration depths of full prototypes particularly in homogenous sediment.

3. The post-arrest rebound of the probe is particularly noticeable in coarse-grained sediments. A dynamic foundation-sediment interaction model can be used to determine the large strain shear modulus of using this sediment type.
4. The analytical model to determine shear strength of soft sediment based on an empirical strain rate dependent material model is proven only with limited experimental data. More advanced material and analytical techniques could be used for such studies.
5. The research documented in this dissertation has made a contribution towards the expanded use of free fall penetrometers with other seafloor survey methods. An application research program that uses this approach is recommended for integration with other geophysical, geotechnical or geological studies of the seafloor.

APPENDIX

FIELD DEPLOYMENT DATA

This appendix presents data from the field deployment of UNH and AFSC FFCPTs. Table A1 provides test data collected with the AFSC FFCPT deployment in the Bering Sea (McConnaughey et al., 2006). Table A2 provides test data collected with the UNH FFCPT in the coastal waters off New Hampshire.

Table A1 - Summary of AFSC FFCPT field deployment in the Bering Sea

Station	Drop	Seabed	M _z	v _i (m/s)	a _{max} (g/s)	t _t (ms)	z(m)
A04	1	VCSilt	4.98	5.91	39.14	0.29	1.01
A04	2	VCSilt	4.98	6.02	40.97	0.24	0.79
A04	3	VCSilt	4.98	6.00	38.93	0.26	0.86
A04	4	VCSilt	4.98	6.11	72.38	0.16	0.53
A04	5	VCSilt	4.98	6.15	38.24	0.26	0.85
A04	6	VCSilt	4.98	6.08	38.00	0.26	0.89
B05	1	VCSilt	4.88	6.32	49.83	0.25	0.96
B05	2	VCSilt	4.88	6.43	33.45	0.33	1.09
B05	3	VCSilt	4.88	6.52	45.97	0.27	0.96
B05	4	VCSilt	4.88	6.54	33.90	0.29	0.99
B05	5	VCSilt	4.88	6.65	63.96	0.25	1.06
B05	6	VCSilt	4.88	6.59	72.14	0.23	0.97
C06	1	VFSand	3.46	6.65	111.76	0.11	0.43
C06	2	VFSand	3.46	6.88	112.66	0.11	0.43
C06	3	VFSand	3.46	7.03	104.46	0.11	0.46
C06	4	VFSand	3.46	7.21	132.91	0.10	0.45
C06	5	VFSand	3.46	7.23	126.08	0.12	0.57
C06	6	VFSand	3.46	7.16	183.90	0.08	0.36
D07	1	VCSilt	4.43	6.70	256.26	0.07	0.29
D07	2	VCSilt	4.43	6.87	280.39	0.06	0.27
D07	3	VCSilt	4.43	6.96	226.91	0.07	0.30
D07	4	VCSilt	4.43	6.99	133.38	0.09	0.37
D07	5	VCSilt	4.43	7.10	246.94	0.06	0.26
D07	6	VCSilt	4.43	7.13	208.46	0.07	0.30
D07	7	VCSilt	4.43	7.26	143.62	0.09	0.35

M:Medium,C:Coarse,VC:Very Coarse,D:Densem,VF:Very Fine; Continued next page...

Table A1 – continued from previous page

Station	Drop	Seabed	M_z	v_i (m/s)	a_{max} (g's)	t_t (ms)	z (m)
E08	1	VFSand	3.61	7.05	186.17	0.07	0.28
E08	2	VFSand	3.61	7.09	193.90	0.07	0.28
E08	3	VFSand	3.61	7.15	178.42	0.09	0.36
E08	4	VFSand	3.61	7.27	243.97	0.07	0.33
E08	5	VFSand	3.61	7.40	218.70	0.07	0.32
E08	6	VFSand	3.61	7.41	145.21	0.08	0.30
F09	1	VFSand	3.08	7.27	577.85	0.04	0.20
F09	2	VFSand	3.08	7.48	256.49	0.05	0.20
F09	3	VFSand	3.08	7.26	561.47	0.04	0.20
F09	4	VFSand	3.08	7.39	292.00	0.04	0.18
F09	5	VFSand	3.08	7.49	361.87	0.05	0.23
F09	6	VFSand	3.08	7.58	533.47	0.03	0.13
F09	7	VFSand	3.08	7.41	675.71	0.05	0.21
H11	1	FSand	2.82	7.67	532.78	0.04	0.20
H11	2	FSand	2.82	7.69	530.74	0.04	0.17
H11	3	FSand	2.82	7.75	499.09	0.03	0.15
H11	4	FSand	2.82	8.19	523.23	0.04	0.15
H11	5	FSand	2.82	8.18	423.77	0.04	0.19
H11	6	FSand	2.82	8.02	578.08	0.03	0.15
V01	1	FSand	2.21	8.17	670.26	0.03	0.14
V01	2	FSand	2.21	7.70	628.82	0.03	0.12
V01	3	FSand	2.21	8.09	692.55	0.03	0.12
V01	4	FSand	2.21	7.98	563.29	0.03	0.11
V01	5	FSand	2.21	8.40	762.88	0.03	0.12
V01	6	FSand	2.21	8.41	740.81	0.03	0.11
X01	1	MSand	1.43	8.44	546.22	0.03	0.15

M:Medium,C:Coarse,VC:Very Coarse;D:Densem,VF:Very Fine; Continued next page...

Table A1 – continued from previous page

Station	Drop	Seabed	M_z	v_i (m/s)	a_{max} (g/s)	t_t (ms)	z (m)
X01	2	MSand	1.43	8.63	673.89	0.03	0.17
X01	3	MSand	1.43	8.86	454.05	0.04	0.21
X01	4	MSand	1.43	8.51	658.88	0.05	0.19
X01	5	MSand	1.43	8.90	777.68	0.04	0.21
X01	6	MSand	1.43	9.08	430.15	0.04	0.21
X02	1	FSand	2.62	8.44	573.75	0.03	0.15
X02	2	FSand	2.62	8.87	383.71	0.04	0.20
X02	3	FSand	2.62	8.54	310.43	0.05	0.25
X02	4	FSand	2.62	8.59	401.01	0.04	0.19
X02	5	FSand	2.62	8.86	505.71	0.03	0.17
X02	6	FSand	2.62	9.17	383.26	0.04	0.20
X03	1	Msand	1.29	8.44	437.19	0.05	0.28
X03	2	Msand	1.29	8.60	698.92	0.03	0.17
X03	3	Msand	1.29	8.66	632.23	0.03	0.14
X03	4	Msand	1.29	8.36	587.40	0.03	0.16
X03	5	Msand	1.29	8.54	313.39	0.05	0.24
K14	1	FSand	2.72	8.65	535.74	0.03	0.15
K14	2	FSand	2.72	8.39	496.37	0.03	0.14
K14	3	FSand	2.72	8.60	528.46	0.04	0.20
K14	4	FSand	2.72	8.39	499.09	0.04	0.15
K14	5	FSand	2.72	9.08	412.63	0.04	0.20
K14	6	FSand	2.72	8.72	519.58	0.04	0.17
F08	1	VFSand	3.78	7.10	327.95	0.05	0.24
F08	2	VFSand	3.78	7.50	302.91	0.05	0.22
F08	3	VFSand	3.78	7.24	326.14	0.05	0.25
F08	4	VFSand	3.78	7.38	292.67	0.06	0.28

M:Medium,C:Coarse,VC:Very Coarse,D:Densem,VF:Very Fine; Continued next page...

Table A1 – continued from previous page

Station	Drop	Seabed	M_z	v_i (m/s)	a_{max} (g's)	t_t (ms)	z (m)
F08	5	VFSand	3.78	7.49	317.04	0.05	0.24
F08	6	VFSand	3.78	7.61	336.60	0.05	0.25
G09	1	FSand	2.94	7.59	244.43	0.06	0.24
G09	2	FSand	2.94	7.87	437.43	0.04	0.14
G09	3	FSand	2.94	7.56	482.26	0.04	0.19
G09	4	FSand	2.94	7.96	360.50	0.04	0.18
G09	5	FSand	2.94	8.02	356.63	0.04	0.17
G09	6	FSand	2.94	7.96	472.25	0.03	0.13
H10	1	FSand	2.63	7.41	407.61	0.04	0.14
H10	2	FSand	2.63	8.29	441.53	0.03	0.14
H10	3	FSand	2.63	8.04	361.64	0.04	0.16
H10	4	FSand	2.63	8.42	426.50	0.04	0.20
H10	5	FSand	2.63	8.22	505.92	0.03	0.16
H10	6	FSand	2.63	8.24	351.85	0.04	0.19
X04	1	VFSand	3.34	7.51	450.40	0.04	0.19
X04	2	VFSand	3.34	6.98	458.60	0.04	0.15
X04	3	VFSand	3.34	7.33	489.54	0.04	0.19
X04	4	VFSand	3.34	7.48	485.67	0.04	0.15
X04	5	VFSand	3.34	7.62	488.40	0.03	0.15
X04	6	VFSand	3.34	7.49	428.56	0.04	0.20
X05	1	FSand	2.54	8.03	610.85	0.03	0.17
X05	2	FSand	2.54	8.10	623.37	0.03	0.17
X05	3	FSand	2.54	8.35	586.72	0.03	0.17
X05	4	FSand	2.54	8.29	626.55	0.03	0.15
X05	5	FSand	2.54	8.23	576.47	0.04	0.18
X05	6	FSand	2.54	8.24	611.08	0.03	0.17

M: Medium, C: Coarse, VC: Very Coarse, D: Densem, VF: Very Fine; Continued next page...

Table A1 – continued from previous page

Station	Drop	Seabed	M_z	v_i (m/s)	a_{max} (g's)	t_t (ms)	z (m)
X06	1	Msand	1.69	8.20	688.92	0.03	0.12
X06	2	Msand	1.69	8.25	632.92	0.03	0.14
X06	3	Msand	1.69	8.50	662.74	0.04	0.26
X07	1	FSand	2.31	8.73	757.41	0.03	0.14
X07	2	FSand	2.31	8.36	723.74	0.03	0.16
D06	1	VCSilt	4.31	6.99	150.45	0.10	0.41
D06	2	VCSilt	4.31	6.81	128.82	0.10	0.43
D06	3	VCSilt	4.31	7.02	95.82	0.12	0.46
D06	4	VCSilt	4.31	7.08	237.15	0.08	0.34
D06	5	VCSilt	4.31	7.11	127.00	0.12	0.51
D06	6	VCSilt	4.31	7.18	151.58	0.09	0.39
D06	7	VCSilt	4.31	6.52	166.36	0.10	0.44
A03	1	CSilt	5.34	4.86	22.76	0.40	0.93
A03	2	CSilt	5.34	5.17	29.59	0.32	0.82
A03	3	CSilt	5.34	4.92	27.55	0.38	1.00
A03	4	CSilt	5.34	5.31	25.94	0.38	1.03
A03	5	CSilt	5.34	5.21	31.41	0.36	1.05
A03	6	CSilt	5.34	5.11	28.68	0.35	0.96
B04	1	CSilt	5.38	5.57	27.31	0.42	1.09
B04	2	CSilt	5.38	5.34	19.80	0.44	1.11
B04	3	CSilt	5.38	5.82	40.97	0.30	0.88
B04	4	CSilt	5.38	5.51	38.69	0.30	0.94
B04	5	CSilt	5.38	5.78	33.90	0.35	1.09
B04	6	CSilt	5.38	5.78	33.90	0.35	1.09
X08	1	VFSand	3.76	6.73	152.25	0.08	0.28
X08	2	VFSand	3.76	6.85	225.32	0.08	0.35

M:Medium, C:Coarse, VC:Very Coarse; D:Densem, VF:Very Fine; Continued next page...

Table A1 – continued from previous page

Station	Drop	Seabed	M_z	v_i (m/s)	a_{max} (g's)	t_t (ms)	z (m)
X08	3	VFSand	3.76	7.19	168.87	0.09	0.36
X08	4	VFSand	3.76	7.39	223.04	0.07	0.29
X09	1	VCSilt	4.04	7.12	147.70	0.09	0.36
X09	2	VCSilt	4.04	7.12	152.04	0.09	0.37
X09	3	VCSilt	4.04	7.04	244.88	0.07	0.31
X09	4	VCSilt	4.04	7.28	147.48	0.08	0.32
D05	1	VCSilt	4.27	6.50	79.21	0.15	0.51
D05	2	VCSilt	4.27	6.88	60.08	0.19	0.65
D05	3	VCSilt	4.27	6.62	101.73	0.14	0.48
D05	4	VCSilt	4.27	6.77	120.86	0.11	0.44
D05	5	VCSilt	4.27	7.00	80.56	0.19	0.61
D05	6	VCSilt	4.27	7.03	93.31	0.19	0.66
F07	1	VCSilt	4.24	7.37	135.87	0.09	0.39
F07	2	VCSilt	4.24	7.22	139.07	0.08	0.30
F07	3	VCSilt	4.24	7.45	166.59	0.08	0.33
F07	4	VCSilt	4.24	7.58	192.53	0.07	0.31
F07	5	VCSilt	4.24	7.39	214.39	0.07	0.34
F07	6	VCSilt	4.24	7.57	197.08	0.09	0.40
F07	7	VCSilt	4.24	7.58	153.84	0.08	0.34
A02	1	unknown	-	5.37	82.84	0.19	0.66
C04	1	unknown	-	5.85	38.93	0.32	1.08
C04	2	unknown	-	6.00	25.49	0.45	1.32
C04	3	unknown	-	5.86	55.07	0.27	0.90
C04	4	unknown	-	5.58	24.35	0.44	1.02
E06	1	unknown	-	7.03	62.35	0.19	0.69
E06	2	unknown	-	7.16	68.73	0.19	0.77

M:Medium,C:Coarse,VC:Very Coarse;D:Densem,VF:Very Fine; Continued next page...

Table A1 – continued from previous page

Station	Drop	Seabed	M_z	v_i (m/s)	a_{max} (g's)	t_t (ms)	z (m)
E06	3	unknown	-	6.92	47.11	0.20	0.72
E06	4	unknown	-	7.33	65.31	0.20	0.69
E06	5	unknown	-	7.42	116.07	0.12	0.46
E06	6	unknown	-	7.21	75.11	0.17	0.54
G08	1	unknown	-	7.24	389.87	0.05	0.22
G08	2	unknown	-	7.72	492.74	0.04	0.22
G08	3	unknown	-	7.56	414.67	0.04	0.20
G08	4	unknown	-	7.67	416.49	0.04	0.20
G08	5	unknown	-	7.47	444.94	0.06	0.30
G08	6	unknown	-	7.80	484.08	0.04	0.19

Table A2 - Summary of UNH FFCPT field deployment

Station	Drop	Seabed	M_z	v_i (m/s)	a_{max} (g's)	t_t (ms)	z (m)
GB	1	unknown	-	10.34	373.84	0.05	0.25
GB	2	unknown	-	10.27	705.97	0.04	0.17
GB	3	unknown	-	10.39	726.29	0.04	0.18
GB	4	unknown	-	9.37	728.75	0.03	0.17
GB	5	unknown	-	9.35	700.02	0.04	0.21
GB	6	unknown	-	9.51	653.76	0.03	0.19
PS	1	unknown	-	10.23	238.25	0.09	0.44
PS	2	unknown	-	10.40	247.00	0.08	0.41
PS	3	unknown	-	10.43	268.38	0.08	0.36
PS	4	unknown	-	10.33	206.72	0.11	0.49
PS	5	unknown	-	10.36	214.76	0.13	0.57
PS	6	unknown	-	10.36	227.38	0.12	0.45
PS	7	unknown	-	10.40	191.65	0.11	0.51
FP	2	unknown	-	7.05	69.02	0.20	0.81
FP	3	unknown	-	7.13	161.51	0.16	0.72
FP	4	unknown	-	6.86	226.34	0.15	0.74
FP	5	unknown	-	7.04	322.67	0.15	0.79
NP	1	VFSand	3.50	8.17	201.46	0.10	0.39
NP	2	VFSand	3.50	8.66	464.92	0.08	0.30
NP	3	VFSand	3.50	8.04	316.37	0.06	0.26
NP	4	VFSand	3.50	7.85	430.93	0.06	0.24
NP	5	VFSand	3.50	7.71	1042.31	0.03	0.06

Notation-VF: Very Fine

LIST OF REFERENCES

- T. Akal and R. D. Stoll. An expendable penetrometer for rapid assessment of seafloor parameters. In *Proceedings OCEANS'95 Conference :Volume 3*, 1995.
- W. A. Allen, E. B. Mayfield, and H. L. Morrison. Dynamics of a projectile penetrating sand. *Journal of Applied Physics*, 28(3):370–376, 1957.
- ASTM. D-2573-01 Standard test method for field vane shear test in cohesive soil. ASTM Book of Standards, 2000.
- C. P. Aubeny and H. Shi. Interpretation of impact penetration measurements in soft clays. *Journal of Geotechnical and Geoenvironmental Engineering*, 132(6):770–777, 2006.
- C. P. Aubeny and H. Shi. Effect of rate-dependent soil strength on cylinders penetrating into soft clay. *IEEE Journal of Oceanic Engineering*, 32(1):49–56, 2007.
- P. Aubeny, C. and A. Dunlap, W. Penetration of cylindrical objects in soft mud. In *Proceedings Oceans 2003*, volume 4, 2003.
- P. Aubeny, C., H. Shi, and D. Murff, J. Collapse loads for a cylinder embedded in trench in cohesive soil. *ASCE International Journal of Geomechanics*, 5(4):320–325, 2005.
- K. Awoshika and W. R. Cox. An application of similitude to model design of a soil-projectile system. Technical report, National Aeronautics and Space Administration (NASA) contractor report CR-1210, University of Texas at Austin, 1968.
- R. M. Beard. A penetrometer for deep ocean exploration. In *Oceans'81*, volume 13. IEEE, 1981.
- R. M. Beard. *Strength Testing of Marine Sediments: Laboratory and In-Situ Measurements*, chapter Expendable doppler penetrometer for deep ocean sediment measurements, pages 101–124. ASTM STP 883, 1985.
- R. H. Bennett, M. H. Hulbert, C. Curry, H. P. Johnson, M. Hutnak, and K. J. Curry. In-situ permeabilities of selected coastal marine sediments. *IEEE Journal of Oceanic Engineering*, 27(3):571–580, 2002.
- D. Blackwood, K. Parolski, and P. Valentine. Seabed observation and sampling system (fact sheet fs-142-00.). Technical report, U.S. Geological Survey, 2000.

- S. J. Blott and K. Pye. GRADISTAT: A grain size distribution and statistics package for the analysis of unconsolidated sediments. *Earth Surface Processes and Landforms*, 26:1237–1248, 2001.
- J. E. Bowles. *Foundation Analysis and Design, Fifth Edition*. McGraw-Hill, 1996.
- S. E. Burns and P. W. Mayne. Analytical cavity expansion-critical state model for piezocone dissipation in fine-grained soils. *Soils and foundations*, 42(2):131–137, 2002.
- B. Buzby and P. Karbe. Grain size analysis results from sediment samples at UNH Pier in Newcastle, Nh. Technical report, Envirosystems Inc., Portsmouth, NH, 2005.
- H. Carslaw and J. Jaeger. *Conduction of heat in solids*. Oxford University Press, 1986.
- T. R. Chari, W. G. Smith, and S. N. Chaudhari. Development of the free-fall penetrometer. In *Oceans'81*, pages 678–682. IEEE, 1981.
- E. E. Davis, G. C. Horel, and R. D. MacDonald. Pore pressures and permeabilities measured in marine sediments with a tethered probe. *Journal of Geophysical Research*, 96,(B4):5975–5984, 1991.
- U. Dayal. Analysis of free-fall penetrometer data. In *Oceans'81*, volume 13, pages 683–687, 1981.
- U. Dayal and W. Allen, J. Instrumented impact cone penetrometer. *Canadian Geotechnical Journal*, 10(3):397–409, 1973.
- U. Dayal and W. Allen, J. Effect of penetration rate on the strength of remolded clay and sand samples. *Canadian Geotechnical Journal*, 12(3):336–348, 1975.
- B. Denness, A. Berry, J. Darwell, and T. Nakamura. Dynamic seabed penetration. In *Oceans'81*, pages 662–667. IEEE, 1981.
- W. Doniger-O'Flaherty. *The Rig Veda: An Anthology*. Penguin Books, 1981.
- H. T. Durgunoglu and J. K. Mitchell. Static penetration resistance of soils, NASA Grant NGR 05-003-406 : Lunar soil properties and soil mechanics,. Technical report, Space Sciences Laboratory, University of California Berkeley and National Aeronautics and Space Administration (NASA), 1973.
- W. W. Fang, M. G. Langseth, and P. J. Schultheiss. Analysis and application of in situ pore pressure measurements in marine sediments. *Journal of Geophysical Research*, 98(B5):7921–7938, 1993.

- E. L. Fasanella, Y. Jones, N. F. Knight, and S. Kellas. Low velocity earth-penetration test and analysis. Technical report, Technical Report: NASA-AIAA-2001-1388, 2001.
- P. Flemings, H. Long, B. Dugan, J. Germaine, C. John, J. Behrmann, D. Sawyer, and IODP Expedition 308 Scientists. Pore pressure penetrometers document high overpressure near the seafloor where multiple submarine landslides have occurred on the continental slope, offshore Louisiana, Gulf of Mexico. *Earth and Planetary Science Letters*, 269(3-4):309 – 325, 2008.
- R. Folk. A Review of Grain-Size Parameters. *Sedimentology*, 6(2):73–93, 1966.
- R. Folk and W. Ward. Brazos River Bar: A study in the significance of grain size parameters. *Journal of Sedimentary Petrology*, 27:3–27, 1957.
- D. J. Goodnight. Impact of a large sphere into a bed of cohesionless particles. Master's thesis, Department of Marine Earth and Atmospheric Sciences, North Carolina State University, 2003.
- G. Guerin and D. Goldeberg. Heave compensation and formation strength evaluation from downhole acceleration measurements while coring. *Geo-Marine Letters*, 22:133–141, 2002.
- N. E. O. Hansen and K. Giselson. Soil reactions in saturated sand caused by impulsive loads. *Journal of Waterway, Port, Coastal, And Ocean Engineering*, 133(1):39–49, 2007.
- O. Hembise, P. Guevel, P. R. Bardey, J. L. Viaud, J. Y. Boisson, and F. Vacherand. Identification of marine soils by ballistic penetrometry. *Journal of Offshore Mechanics and Arctic Engineering*, 112(4):277–284, 1990.
- S. Hill. Grain size analysis of sediment samples from Bering Sea Research Cruise : Report submitted to AFSC, NOAA Seattle WA. Technical report, GeoSea Consulting Ltd., Brentwood Bay, BC, Canada, 2006.
- G. Houlsby and C. Teh. Analysis of the piezocone in clay. In *Proc. of the 1st International Symp. on Penetration Testing, ISOPT-1*, number 2, pages 777–783, 1988.
- G. T. Houlsby and C. M. Martin. Undrained bearing capacity factors for conical footings on clay. *Geotechnique*, 53(5):513–520, 2003.
- G. T. Houlsby and C. P. Wroth. Direct solution of plasticity problems in soils by the method of characteristics. In *Proc. 4th International Conference on Numerical Methods in Geomechanics, Edmonton*, volume 3, pages 1059–1071, 1982.

- K. M. Kelly and G. J. Heald. *Impact of Littoral Environmental Variability on Acoustic Predictions and Sonar Performance*, chapter Mapping Seabed Variability Using Combined Echosounder and XBPS for SONAR Performance Prediction, pages 99–106. 2002. hardcopy.
- S. J. Knight and C. A. Blackmon. Studies of aerial cone penetrometer:laboratory study of mechanical principles and mechanical principles. Technical report, US Army Corps of Engineers, Vicksburg, Mississippi. Technical Report No. 3-462 , 1 and 2, 1957.
- S. Lacasse and T. Lunne. Penetration tests in two norwegian clays, proceedings. In *Proceedings, Second European Symposium on Penetration Testing*, volume 2, 1982.
- D. S. Lee and D. Elsworth. Indentation of a free-falling sharp penetrometer into a poroelastic seabed. *Journal of Engineering Mechanics*, 130(2):170–179, February 2004.
- T. Lunne, J. Powell, T. Eidsmoen, and R. Quarterman. Comparison of piezocones in overconsolidated clays. Technical report, Norwegian Geotechnical Institute, Contract Report No. 84223-1, 1985.
- T. Lunne, P. K. Robertson, and J. J. M. Powell. *Cone Penetration Testing in Geotechnical Practice*. Spon Press, 1997.
- T. Lunne, T. and Eidsmoen, J. Powell, and R. Quarterman. Piezocone testing in overconsolidated clays. In *Proceedings, 39th Canadian Geotechnical Conference*, 1986.
- MathWorks Inc. Matlab 2008b, User Documentation, 2008.
- J. L. McCarty and H. D. Carden. Impact characteristics of various materials obtained by an acceleration-time-history technique applicable to evaluating remote targets. Technical report, NASA Langley Research Center, 1962.
- J. L. McCarty and H. D. Carden. Response characteristics of impacting penetrometers appropriate to lunar and planetary missions. Technical report, National Aeronautics and Space Administration, 1968.
- R. McConnaughey, C. Yeung, M. Amend, J. Lomnicky, and K. Smith. Cruise report for 2006 FISHPAC project. Technical report, Alaska Fisheries Science Center, Seattle, WA, 2006.
- R. L. McNeill. Enhancement of geophysical soil profiles using instrumented sediment penetrators. In *Proceedings Offshore Technology Conference, OTC 3526*, volume 3, pages 1469–1480, 1979.
- R. L. McNeill. Approximate method for estimating the strengths of cohesive materials from penetrator decelerations. In *Oceans'81*, volume 13. IEEE, 1981.

- R. L. McNeill and I. Noorany. Offshore in-situ testing techniques. Technical report, Sandia Laboratories, 1983.
- J. S. Melton. FFCPT deployment in Providence Harbor CAD Cells on february 20, 2004. Technical report, Report to ENSR, Deapartment of Civil Engineering, University of New Hampshire, 2005.
- J. Meunier, Sangouard, and B. Lhuillier. A new seabed penetrometer. In *Offshore Technology Conference*, 2000.
- J. K. Mitchell. *Fundamentals of Soil Behavior*. John Wiley and Sons, 1975.
- A. B. N. K. Moore, G.F.and Taira, S., T. Shipley, C. Alex, S. Gulick, D. Hills, T. Ike, S. Ito, S. Leslie, A. McCutcheon, K. Mochizuki, S. Morita, Y. Nakamura, J.-O. Park, B. Taylor, G. Toyama, H. Yagi, , and Z. Zhao. Shipboard scientific party, 2001. leg 190 summary. In *Proceedings of the Ocean Drilling Program, Initial Reports Volume 190*, 2001.
- J. Moulton and N. Stuttdard. Boring logs for UNH Pier Replacement. Technical report, GZA Environmental Inc. , Providence , RI, 2002.
- J. Osler, A. Furlong, H. Christian, and M. Lamplugh. The integration of the Free Fall Cone Penetrometer (FFCPT) with the Moving Vessel Profiler (MVP) for the rapid assessment of seabed characteristics. In *Proceedings Undersea Defense Technology Pacific, San Diego*, 2006.
- A. R. Poor, W. R. Cox, and L. C. Reese. Behavior of sandy clay under vertical impact of geometric shapes. Technical report, National Aeronautics and Space Administration (NASA), 1965.
- M. Randolph. Characterisation of soft sediments for offshore applications. In V. da Fonseca and P. Mayne, editors, *Proceedings ISC-2 on Geotechnical and Geophysical Site Characterization*. Millpress, Rotterdam, 2004.
- M. F. Randolph and C. P. Wroth. An analytical solution for the consolidation around a driven pile. *International Journal for Numerical and Analytical Methods in Geomechanics*, 3(3):217–229, 1979.
- P. Robertson. Soil classification using the cone penetration test. *Canadian Geotechnical Journal*, 27(1):151–158, 1990.
- P. Schultheiss. *Geotechnical Engineering of Ocean Waste Disposal, ASTM STP 1087*, chapter In situ pore pressure measurements for a detailed assessment of marine sediments: state of the art, pages 190–205. ASTM, Philadelphia,, 1990.
- P. J. Schultheiss, S. D. McPhail, A. R. Packwood, and B. Hart. An instrument to measure differential pore pressures in deep ocean sediments: Pop-up-pore pressure instrument. Technical report, Institute of Oceanographic Sciences, Wormley, UK, Report No 202, 1985.

- R. F. Scott. In-place ocean soil strength by accelerometer. *Journal of the Soil Mechanics and Foundations Division*, 96(1):199–211, 1970.
- T. C. Sheahan, C. C. Ladd, and J. T. Germaine. Rate-dependent undrained shear behavior of saturated clay. *Journal of Geotechnical Engineering*, 122(2):99–108, 1996.
- H. Shi. *Numerical simulations and predictive models of undrained penetration in soft soils*. PhD thesis, Office of Graduate Studies (Civil Engineering), Texas A&M University, August 2005.
- I. S. Spooner, P. Williams, and K. Martin. Construction and use of an inexpensive, lightweight free-fall penetrometer: applications to paleolimnological research. *Journal of Paleolimnology*, 32(3):305–310, 2004.
- S. Stegmann, H. Villinger, and A. Kopf. Design of a modular, marine free-fall cone penetrometer. *Sea Technology*, 47(2):27–33, 2005.
- S. Stegmann, T. Morz, and A. Kopf. Initial results of a new free fall cone penetrometer(ff-cpt) for geotechnical in situ characterisation of soft marine sediments. *Norwegian Journal of Geology*, 86:199–208, 2006.
- S. Stegmann, M. Strasser, F. Anselmetti, and A. Kopf. Geotechnical in-situ characterization of subaquatic slopes: The role of pore pressure transients versus frictional strength in landslide initiation. *Geophysical Research Letters*, 34, 2007.
- D. Stoll, R., Y.-F. Sun, and I. Bitte. Seafloor properties from penetrometer tests. *IEEE Journal of Ocean Engineering*, 32(1):57–63, 2007.
- R. Stoll and A. Tumay. Probe for evaluating seafloor geoaoustic and geotechnical properties, us patent 5681982. Technical report, 1997.
- R. D. Stoll. Measuring sea bed properties using static and dynamic penetrometers. In *Civil Engineering in the Ocean VI*, pages 386–395. American Society of Civil Engineers, 2006.
- R. D. Stoll and T. Akal. XBP -tool for rapid assessment of seabed sediment properties. *Sea Technology*, 40(2):47–51, 1999.
- M. Strasser, S. Stegmann, F. Bussmann, F. S. Anselmett, B. Rick, and A. Kopf. Quantifying subaqueous slope stability during seismic shaking: Lake lucerne as model for ocean margins. *Marine Geology*, 240:77–97, 2007.
- Sustainable Fisheries Act . Public law 104-297 Enacted by the 104th Congress of the United States, 1996.
- A. H. Tarabay and M. Sanai. Penetration of a rigid body projectile into underwater sediments. In *Proceedings of the 65th Shock and Vibration Symposium*, pages 137–154, 1994.

- C. Teh and G. Houlsby. Analysis of the cone penetration test by the strain path method. In I. Swoboda, editor, *Proc. of the 6th International Conference on Numerical and Analytical Methods in Geo-mechanics*, pages 397–402, Rotterdam, 1988. Balkema.
- J. B. Thomsson and J. K. Mitchell. Determination of insitu soil properties utilizing an impact penetrometer. Technical report, National Aeronautics and Space Administration (NASA) :Lunar Surface Engineering Properties Experiment Definition Volume I of IV, 1971.
- D. G. True. *Undrained Vertical Penetration Into Ocean Bottom Soils*. PhD thesis, University of California at Berkeley, 1976.
- G. W. Turnage. Influence of viscous-type and inertial forces on the penetration resistance of saturated fine grained soils. *Journal of Terramechanics*, 10(2):63–76, 1973.
- R. Urgeles, M. Canals, and J. Roberts. Fluid flow from pore pressure measurements off La Palma, Canary Islands. *Journal of Volcanology and Geothermal Research*, 101:253–271, 2000.
- D. P. Womack and W. R. Cox. Measurement of dynamic characteristics of soils with penetrometers. Technical report, University of Texas at Austin, 1967. Report submitted to NASA.
- C. W. Young. An empirical equation for predicting penetration depth into soft sediments. In *Oceans' 81*, pages 674–681, 1981.
- H.-S. Yu. *Cavity Expansion Methods in Geomechanics*. Springer, 2000.
- H.-S. Yu. Proceedings isc-2 on geotechnical and geophysical site characterization. pages 3–38. Millpress, Rotterdam, 2004.